Dipl.-Ing. Sebastian Nau, BSc

Organic Resistive Memory Devices: Unveiling the Nature of Resistive Switching and Evolving Applications

DOCTORAL THESIS

For obtaining the academic degree of

Doktor der technischen Wissenschaften

Doctoral Programme of Technical Sciences
Technical Physics

Graz University of Technology

Supervisor:

Ao. Univ.-Prof. Dipl.-Ing. Dr.techn. Emil J. W. List-Kratochvil

Institute of Solid State Physics

In cooperation with

NanoTecCenter Weiz Forschungsgesellschaft mbH

Graz, September 2014

EIDESSTATTLICHE ERKLÄRUNG

AFFIDAVIT

Ich erkläre an Eides statt, dass ich die vorliegende Arbeit selbstständig verfasst, andere als die angegebenen Quellen/Hilfsmittel nicht benutzt, und die den benutzten Quellen wörtlich und inhaltlich entnommenen Stellen als solche kenntlich gemacht habe. Das in TUGRAZonline hochgeladene Textdokument ist mit der vorliegenden Dissertation identisch.

I declare that I have authored this thesis independently, that I have not used other than the declared sources/resources, and that I have explicitly indicated all material which has been quoted either literally or by content from the sources used. The text document uploaded to TUGRAZonline is identical to the present doctoral dissertation.

Datum / Date

Unterschrift / Signature

für meine Eltern…

Acknowledgments – Danksagung

After three years of endeavor I am finally in the position to thank several important people who were directly and indirectly involved in the creation of this work.

I would like to thank my supervisor, Emil J. W. List-Kratochvil for making this work possible and for guiding me through the rough world of science.

Highest honors go to Stefan for constantly being skeptical about my work and results, for creating opportunities, simply making things possible but most important for being a friend. When I finished my master thesis I remember that I was acknowledging Stefan for 'showing me my limits in sports': I guess these times have changed, Stefan!

I cannot express how many hours my fellow PhD-students Kerstin, Johannes and Florian (less many hours, but still a lot) and me spend together in the lab, constantly battling shoulder-to-shoulder for science and against other fears. Every day we spend together in work, on our way back home and after work was a great pleasure and honor to me. Thank you, Cheers!

I would also like to thank my master student, Christoph Engelbert for his eagerness and willingness to learn. Also for providing cake every morning thus helping me not to lose weight. Good luck in Korea!

Several people who worked with me together on different tasks should be also acknowledged. Karl, the printer operator, Conny and Angelika, our chemistry ladies and Markus, master of the 3D-printer and everything else. There are many other people in our organization that made my time as a PhD-student so much easier and enjoyable. Thank you all!

Further I want to thank all my friends who still stand by me, even though I had rarely time for social activities.

For funding, the European Commission is acknowledged (Project HYMEC: FP7-NMP-2010-SMALL-4 program, project number 263073).

Meiner Familie möchte ich hiermit für die vielen Jahre des Rückhalts danken! Ohne euch wäre ich nicht so weit gekommen! Danke!

Abstract

Electrically tunable resistors based on two terminal structures are currently one of the most versatile innovations in the semiconductor industry with many possible applications such as logic circuitry, memory devices or neuromorphic systems. In particular, inorganic resistive switching devices implemented as memories are on the edge to commercialization. Restive switching was observed in organic devices as well. However, despite vital academic interest a consistent explanation about their working mechanisms is still missing.

Within this thesis, a set of experimental findings which explain unipolar resistive switching are presented: For the first time it is unambiguously possible to rule out most models which are held to be responsible for switching in organic devices. It is shown that the memory behavior is due to the formation and rupture of a localized conductive pathway ('filament') rather than any charging effects. Furthermore, it is also shown that resistive switching is a universal and largely material independent property in metal/organic/metal thin-film structures. With this knowledge, a route towards the first all inkjet-printed organic resistive switch is described. Conventional fabrication routes of the functional components are successively replaced step-by-step through inkjet-printing. For each configuration a distinct impact on the device characteristics is found and analyzed. Using a high-performance organic diode, these inkjet-printed devices are successfully integrated into a passive matrix crossbar array.

Optical addressing of organic resistive switches in a 1 Diode – 1 Resistor setup is presented. With an appealingly simple approach, it is possible to manipulate the resistive state of the memory device by a photonic stimulus. Based on this feature, photo-switchable non-volatile resistive multi-bit 2-terminal devices as pixels in flexible image detectors are demonstrated. These structures are scaled up to 32 by 32 cells (1024 bit), integrated into an organic and flexible passive-matrix image detector array.

As a second application, the possibility of controlling organic light emitting diodes with resistive switches is demonstrated resulting in luminance and color tuning of highly efficient blue and white light emitting polymer LEDs at constant operation voltage.

Kurzfassung

Elektrisch veränderbare Widerstände werden als eine der wichtigsten Innovationen der Halbleiterforschung der letzten Jahre angesehen. Basierend auf den besonderen Bauteileigenschaften konnten Logikschaltungen oder sogenannte neuromorphe Systeme bereits erfolgreich demonstriert werden. Insbesondere bieten diese resistiven Schaltelemente großes Potential in der Anwendung als Speicherbausteine und eine Kommerzialisierung kann in absehbarer Zeit erwartet werden. Resistives Schalten wurde auch in verschiedenen organischen Materialien beobachtet, jedoch konnte der Arbeitsmechanismus bis dato nicht eindeutig erklärt werden.

In diesem Zusammenhang wird in dieser Arbeit eine Reihe von Experimenten präsentiert, die die Vorgänge beim resistives Schalten erklären. Durch eine sorgfältige Wahl der Experimente ist es nun zum ersten Mal eindeutig möglich, die meisten der bislang vorgeschlagenen Arbeitsmechanismen auszuschließen. Es wird gezeigt, dass resistives Schalten als die Formierung und den Bruch eines sehr kleinen, lokalisiert leitfähigen Pfades durch das Bauteil ("Filament") interpretiert werden kann. Daraus lässt sich ableiten, dass resistives Schalten eine universelle und damit weitgehend materialunabhängige Eigenschaft von Metall/organischer Halbleiter/Metall oder Metall/Isolator/Metall Dünnschichtstrukturen ist. Im Zuge dieser Arbeit werden neben der Bauteilcharakterisierung auch alternative Herstellungstechniken von resistiven Schaltelementen wie etwa mittels Tintenstrahldruck-Verfahren gezeigt. Die Realisierung erfolgt dabei durch sukzessive Substitution von konventionellen Produktionsschritten durch tintenstrahl-basierende Präparationsprozesse. Deren Einfluss auf die Bauteileigenschaften wird im Detail untersucht. Im Weiteren wird die Integration dieser tintenstrahlgedruckten Bauteile in eine voll funktionsfähige passiv-matrix Struktur präsentiert.

Neben der Anwendung als Speicherbausteine, wird die optische Adressierbarkeit von resistiven Schaltern vorgestellt. Mittels eines einfachen Ansatzes ist es möglich, den Widerstandszustand der Speicherbausteine durch einen photonischen Stimulus zu manipulieren. Basierend auf dieser Eigenschaft werden photo-schaltbare nichtflüchtige Widerstände als Pixel in einem bis zu 32 mal 32 Pixel großen (1024 Bit) flexiblen passiv-matrix Lichtdetektor demonstriert.

Darüber hinaus wird die Ansteuerung organischer Leuchtdioden mittels resistiver Schalter gezeigt. Dieses neuartige Konzept ermöglicht eine Abstimmung von Luminanz und Emissionsspektrum von hocheffizienten blau bzw. weiß emittierend Polymer-LEDs bei konstanter Betriebsspannung.

Table of Contents

List of Acronyms

This section summarizes repeatedly used acronyms of this work.

1D-1R	1 diode - 1 resistor
Alq3	Aluminium-tris(8-hydroxychinolin)
AuNP	Gold nanoparticles
CCD	Charge-coupled devices
CMOS	Complementary metal-oxide-semiconductor
HOMO	Highest occupied molecular orbital
HRS	High resistance state
IMRS	Intermediate resistance state
ITO	Indium tin oxide
IV(-curve)	Current-voltage curve
LRS	Low resistance state
LUMO	Lowest unoccupied molecular orbital
NDR	Negative differential resistance
OD	Organic Diode
OLED	Organic light emitting diode
OPD	Organic photodiode
ORS	Organic resistive switch
PCBM	Phenyl-C61-butyric acid methyl ester
PLED	Polymer light emitting diode
PMMA	Poly(methyl methacrylate)
PS	Poly(styrene)
rr-P3HT	regio-regular poly(3-hexylthiophen-2,5-diyl)
V_T	threshold voltage
WOLED	White organic light emitting diode

Outline

Today a variety of established types of memory exist, used in dependence of the needs of the application. Although we usually just call them ‘memory’ or ‘data storage’, the physical working mechanism significantly differs from one type to another. A small fraction of this work addresses this issue as the most prominent and widespread technologies are discussed in the introduction (***Chapter 1***). In addition an overview over memory technologies currently under development and on the edge to commercialization is given including the concept of resistive switches and memristors. The latter were recently taken up by several companies as it promises great advantages over current memory technologies in terms of integration density, speed, power consumption, etc.

Chapter 2 deals with the implementation of organic materials in resistive switching devices. Unlike their inorganic counterparts, the working mechanism for organic devices isn’t well understood. Therefore the basic features as well as the most commonly proposed working mechanisms are presented and discussed. Further a promising strategy to integrate these switches into arrays is shown.

Chapter 3 unveils the working mechanism of organic resistive switches (ORS). On the basis of three prototypical model devices and a set of experiments (I/V-characterization, photovoltaic measurements and impedance spectroscopy), the actual origin of the memory functionally is unambiguously explained by using fundamental physical and electro-technical considerations. Furthermore it is inferred that resistive switching is a universal property of metal/organic/metal devices.

Chapter 4 explores the possibility of inkjet-printing of these devices. For the first time, an all inkjet-printed ORS is presented. The impact of every single fabrication step is investigated. Moreover, the printed devices are implemented in conjunction with high-performance organic diodes as selector elements, demonstrating a partly inkjet-printed fully functional memory array.

Chapter 5 presents the optical addressing of ORS. It is shown that the memory can be written and erased by a photonic stimulus. Thus the device is not only an optically write and erasable memory, but also an image detector, similar to the well-known charge-coupled devices (CCD). Along these lines, the prototype of a unique organic image detection array technology is presented and discussed. Additionally, this new principle is expanded in terms of x-ray detection.

Chapter 6 shows how organic light emitting diodes (OLED) can be combined with ORS. The change of luminance at constant operation voltage of the OLED is presented. This principle is expanded to allow the tuning of the electroluminescence emission spectrum in white light emitting OLEDs (WOLED). Along these lines, the fabrication of a novel, highly efficient and color-stable PLED is shown.

Chapter 7 concludes this work.

1 Introduction to Memory and Storage Technologies

The following chapter provides a background in terms of memory and storage technology. A general classification is given and memory related figures of merit are presented. The current market leaders, emerging technologies and their physical storage mechanism are described. The last part of this chapter addresses the inorganic counterpart to the topic of this work, resistive random access memory.

The discovery of how to store information in form of numbers and letters is generally considered as one of the most important steps of social evolution in human history as it allowed passing information from generation to generation. The simplest forms appeared at least forty thousand years ago in the form of unary numeral systems (tally marks). Real alphabets developed, however, much later around 4000 BC in Mesopotamia. The invention of a moveable metal type printing press by Johannes Gutenberg (1450) is considered as another big leap since it enabled a relatively cheap, large scale duplication of information. Nowadays, information is stored digitally encoded in a binary language consisting of zeros and ones, i.e. binary logical states. The origin of the rapid development in this field dates back to the 1940s, starting from the first computer prototypes with an implemented memory – Zuse3 (1942, Germany) and ENIAC (1946, USA) - via the launch of first personal computers (1970s) to the present state where digital memory is found in nearly every electronic device. Recent calculations showed that approximately 300 exabytes (10^{18} byte) of information is stored worldwide.[1]

Memory capacity develops according to Moores law[2], meaning that roughly every 18 month a doubling of the number of transistors per chip at approximately equal costs was found. Although this observation has been doubtlessly valid for the past decades, a strong convergence to a upper integration density is predicted. It is expected that within the next 10 to 20 years it will not be possible to further downsize the traditional complementary metal-oxide-semiconductor (CMOS) architecture due to physical restrictions at such small dimensions. In order to overcome this fact, two parallel strategies are usually presented. First, *more Moore*, dealing with the continuous miniaturization of classical CMOS building blocks as well as post-CMOS materials and devices. Second, the *more-than-Moore* approach which targets system integration and functional diversification rather than scaling issues: The inclusion of non-digital functionalities like sensors and actuators, bio-chips, photonic applications, etc. interfaces the integrated circuit to the outside world.

This work actually addresses both approaches by investigating organic resistive switching memory technology and its advantages (*more Moore*) and demonstrating how resistive memory can be integrated with photonic devices (*more-than-Moore*).

In principle every system with two electronically distinguishable states can be used as digital memory. However there are several other prerequisites what a memory device, especially an emerging one, should fulfill to outpace established technologies. The most important ones are listed in the following:

- Non-volatility: State should be preserved at least for several years even if the supply voltage is turned off.
- Fast read, write and erase times in the range of the CPU clock (~ GHz): This prevents a bottleneck effect in the communication between the individual components in an electronic application.
- Cyclability: 10^{12} - 10^{15} write-read-erase-read cycles should be possible
- CMOS compatibility
- Operation temperature not higher than 85°C
- ON/OFF ratio: Clear difference between ‘0’ (OFF) and ‘1’ (ON) state which enables for simple peripheral electronics and a reliable read-out
- High integration density (down to $4F^2$, where F denotes the smallest lithographically obtainable feature size)
- Low power consumption
- Compatibility with existing semiconductor fabrication plants
- Non-destructive read-out
- 3D-integration on multiple layers, multiple bits per cell
- Random Access: Each bit cell should be accessible directly and sequential read out is necessary.

As discussed in the following chapters, today’s dominant memory technologies do not meet all of these criteria simultaneously and the decision which memory or storage technology is used strongly depends on its actual application. Figure 1.1 depicts the memory-storage hierarchy. Usually storage and memory are considered separately, whereas the first term includes non-volatile, high capacity technologies and the latter term is used for fast, lower capacity and volatile technologies.

Along these lines, the main task is the development of a technology which unifies memory and storage technology to a ‘storage class memory’ with the advantages of both. This would allow for example to design computers where the operating systems and other data does not need to be read out from the hard disc drive to the main memory when its switched on.

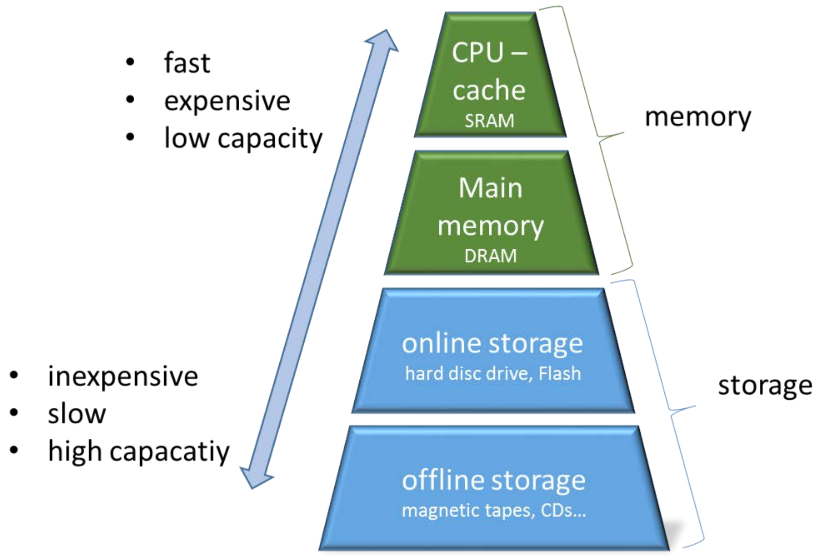

Figure 1.1. Memory-storage hierarchy. Costs and speed are increasing from bottom to the top whereas information capacity is decreasing.

1.1 Established technologies and their physical storage principle

Nowadays, three technologies dominate the market - each of them highly specialized in its field of application.

Dynamic Random Access Memory (DRAM)

DRAM is omnipresent in modern computers (including smartphones, tablets, etc.). Each bit of information is stored on a capacitor which can either be charged (logical 1) or discharged (logical 0). The information can be read out by essentially shortening the capacitor and measuring the current. If a certain discharge current is detected, a logical '1' was stored, if no current is measured, the initial state was a logical '0'. Such a procedure is called destructive read-out, since the read-out procedure can change the state of the capacitor. To keep the information in the DRAM cell a refresh cycle after each read-out operation is needed. Also without a read-out operation a charged capacitor quickly discharges (several ms) due to inevitable leakage current through the dielectric. Thus this device is a *volatile* memory and a periodic refresh is needed in order to maintain the present state. DRAM cells are typically aligned in a crossbar matrix. With each capacitor, a selector device (a transistor) has to be implemented. This decreased integration density of the DRAM technology.

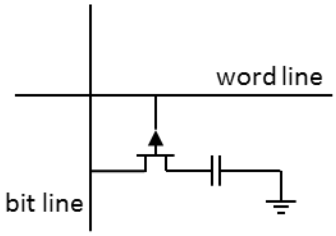

Figure 1.2. Sketch of a single DRAM cell consisting of a transistor as selector element and a capacitor. Such elements are wired in a crossbar of so called word and bit lines

Flash memory

A single flash memory cell basically consists of a metal-oxide-semiconductor (MOS) transistor with an additional floating gate embedded in the gate oxide (Figure 1.3). A bias applied to the control gate results in charge carriers tunneling from the control gate onto the floating gate or from the floating gate to the control gate, respectively. Since the floating gate is electrically insulated by the gate oxide, its charged or uncharged character is stable over time. These two states modify the conductivity of the channel similar to the standard operation of a field-effect transistor. Flash memory has severe drawbacks like a possible gate oxide breakdown induced by the high electric fields necessary for tunneling charges on and off the floating gate, leading to a reduction of its lifetime to several 10^5 cycles. Further, the write and erase times are in the range of several µs. Nowadays, new stratgeies of implementing Flash memory are explored including multi-bit storage[3] as well as 3D-stacking[4], making it to a serious competitor to emerging memory technologies.

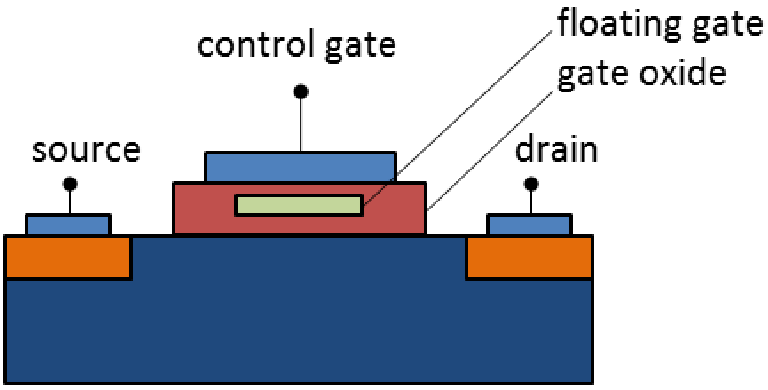

Figure 1.3. Sketch of a single bit cell of a Flash memory. Charge carriers are tunneling off and on the floating gate by controlled by the so called control gate. This renders the channel of the field-effect transistor either conductive or non-conductive which is used to store logical information.

Hard disc drive

The hard disc drive (HDD) was developed in 1956 by IBM. The storage mechanism is based on the magnetization of single units on a rotating disc coated with a ferromagnetic material. The magnetization of these domains can be influence by a read/write head which - at least in the early implementations - can be considered as a little electromagnet. When the ferromagnetic cell of interest passes the stationary read/write head, a current proportional to its magnetization is induced, detected and interpreted as logic 0 or 1. For writing a single bit the process is reversed – a small current in the head causes a change in magnetization of the ferromagnetic material. In later implementations, the effect of magnetoresistance and most up to date, giant magnetoresistance[5] are used to read single magnetic domains. Due to the superparamagnetic limit, where already thermal fluctuations lead to an influence of the orientation of magnetization, further increase in storage density is limited.

Besides the market leaders one may find several other memory technologies in modern electronic devices, highly specialized to their actual application: Static random access memory (SRAM) is applied as a fast data cache close to the processor, magnetic tapes for long term data storage or mechanical implementations like the compact disc.

1.2 Emerging concepts

There is wide consensus, that one major challenge for the future clearly is the unification of the advantages of these memory devices. Several technologies are considered to be capable of achieving this goal. The most prominent are discussed in the following.

Ferroelectric RAM (FeRAM)

The setup of a ferroelectric memory cell is similar to that of DRAM with the difference that instead of a dielectric a ferroelectric material is used. In contrast to most other materials, ferroelectrics exhibit a hysteresis in the electric field – polarization curve (Figure 1.4), meaning that a certain polarization remains when the applied electric field is removed. This feature is utilized to write logic states. A state can be read-out by applying a voltage pulse which forces the device to a defined polarization state. Nothing happens if the initial polarization of the ferroelectric is equal to the new polarization. If the initial polarization was different, a certain displacement current can be detected from the periphery. It is evident that this is a destructive read-out mechanism and the initial state has to be re-written after each read operation.

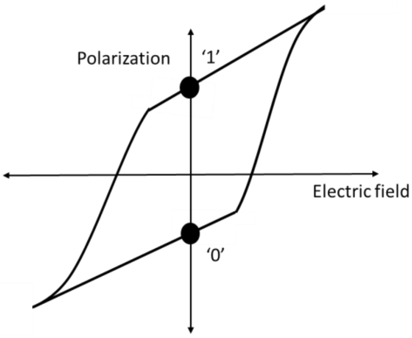

Figure 1.4. Sketch of the ferroelectric hysteresis: At zero field the two possible orientations of polarization are used as logic states.

This technology was originally thought to be the most promising candidate to replace DRAM and Flash, since it has the advantages of both technologies (speed and simple structure from DRAM and non-volatility from Flash). Although FeRAM is already on the market, there are a multitude of failure mechanisms during operation including depolarization (loss of the ability to be polarized) and imprint (loss of ability to change the polarization) which still limit the widespread applicability.[6] However, in several niche markets, especially in the field of low-cost applications, FeRAM is still a popular choice.

Magnetoresistive RAM (MRAM)

A magnetoresistive memory cell basically consists of two ferromagnetic layers separated from each other by an insulating tunnel layer. This setup is commonly known as ‘spin-valve’: One of the ferreomagnetic layers has a pinned magnetization orientation, whereas the second one can be changed. The effective resistance of the three layer stack is dependent on the relative magnetization of the two layers, an effect called giant magnetoreistance[5]. If a bias is applied between bit line and read line and the magnetizations of the layers are aligned in parallel, a low resistance is found. Anti-parallel alignment leads to a high resistance, correspondingly. Writing and erasing of the magnetization of the free magnetic layer is facilitated by passing a current through the write line which then induces a magnetic field in the cell.

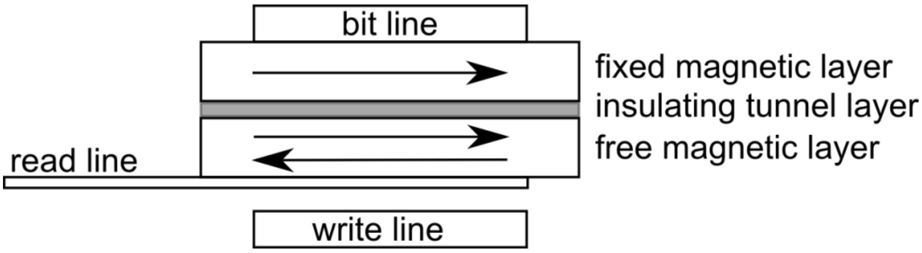

Figure 1.5. Schematic of a single MRAM cell. The effect of giant magnetoresistance is used to store logic information. If the magnetization of both ferromagnetic layers is aligned in parallel, a low resistance is found when a voltage is applied between read a bit line. If they are aligned anti-parallel, a high resistance can be measured. The write line is used to change the magnetization of one of the layers.

MRAM shows very impressive performance parameters in terms of speed and power consumption; however several issues limit a widespread commercialization. The induced magnetic field necessary for writing can also induce a magnetization change in neighboring cells, clearly limiting downscaling and thus increasing of the packing density. Further there are severe cost related issues.[6]

Phase-change RAM (PCRAM)

Phase-change materials are a class of materials which can be switched from an amorphous phase to a crystalline phase mediated by Joule heating.[7] Both phases are strongly different in their electrical conductivity which can be employed for data storage. These materials, mostly chalcogenide glass like GeTe[8], are sandwiched between two electrodes, where certain specific pulses heat the material and lead to a phase change, accompanied by a resistance change. The written state can be read-out at low voltage levels, unable to induce a phase change. PCRAM was first introduced to the market on a large scale in mobile phones[9], however the strong concurrence of stackable Flash memory recently led to a withdrawal of PCRAM from the market.[10]

Note that also the optical properties (more specific: the reflectivity) are different for both phases. This principle is employed DVDs and Blu-Ray discs for writing and reading data.

1.3 Resistive Memory

Amongst the here presented candidates, resistive random access memory is doubtless the most promising candidate to act as storage class memory.

There are several physical mechanisms which can lead to a change in resistance of the observed system like molecular memories[11,12] or the previously presented PCRAM and MRAM. This section however, introduces a memory device which is commonly referred to as resistive switch, resistive memory or resistive random access memory. It turns out that this type of memory matches well with the theoretically predicted fourth fundamental passive building block in electronics (the other ones being resistor, capacitor and inductor) – the memristor – formulated by Leon Chua in 1971.[13,14] It took several decades until S. Williams et al. at the HP labs linked the theoretically predicted device characteristics with resistive switches.[15] Since then, a rapid development started, and commercialization is claimed to be possible within less than 5 years. Very promising demonstrators have recently been presented importantly fabricated in an 28 nm CMOS-compatible process.[16]

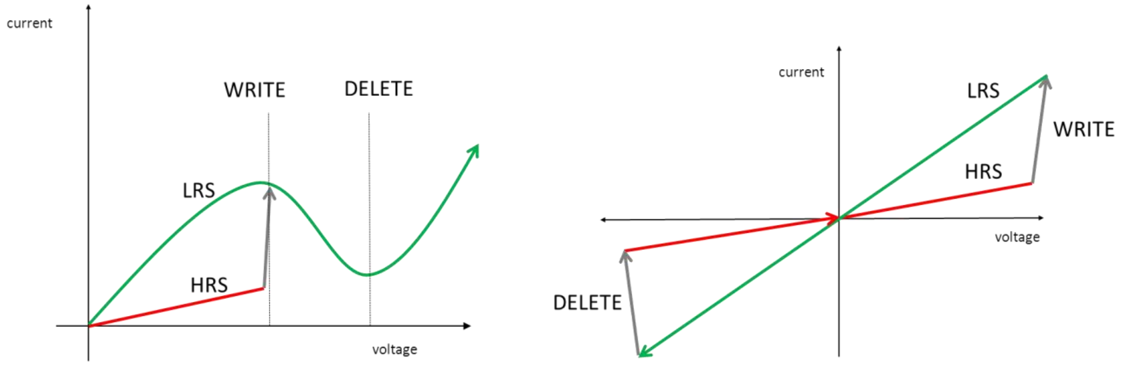

Figure 1.6. Unipolar (left) and bipolar (right) modes of resistive switching.

Basically two different modes of operation are usually assigned to resistive switching. First, unipolar switching, meaning that the memory can be written and erased with equal voltage polarity. Second, bipolar switching, meaning writing and erasing with opposite voltage polarity (Figure 1.6) These operation modes are assigned to different working mechanisms which are summarized in the following:[17]

Electrochemical metallization processes

An electrochemical metallization cell basically consists of a thin-film solid-state electrolyte sandwiched between an electrochemically active electrode (such as Ag or Cu) and an electrochemically inactive counter electrode (Pt, Au, W). If a sufficiently high bias is applied to the cell, anodic dissolution of the active electrode M occurs ($M \rightarrow M^{z+} + ze^-$), accompanied by a migration of the metal cations through the solid state electrolyte. These metal cations are reduced at the inactive electrode and finally crystalize there ($M^{z+} + ze^- \rightarrow M$). This leads to the growth of a filament through the device which is able to transmit a large current after establishing a connection between the electrodes (low resistance state - LRS). By applying a bias in opposite polarity, dissolution of the filament forming metal and a corresponding counter diffusion back to the active electrode occurs. As soon as the filament is disconnected, a high resistance state (HRS) is found. As this description suggests this mechanism is bipolar. Further, the mechanism can be considered as universal in any solid-state electrolyte with a reasonable ion-conductivity.

Valence change mechanism

The valence change mechanism is most likely to occur in binary transition metal oxides. In contrast to the former described mechanism, valence change is associated with the diffusion of anions (and more specifically oxygen anions). To prevent and exclude the previously described electrochemical metallization, both electrodes should be electrochemically inactive. Under the electric field, the oxide species gets reduced at the anode interface, leaving oxygen vacancies behind. The vacancies then migrate through the oxide to the cathode interface where they form a filament (consisting of oxygen vacancies) at spots of high electric field (most likely due to inhomogeneity of the electrode and the oxide). Since reduced metal oxides can have a considerable higher electrical conductivity, an LRS would be the result if the filament is eventually connected to the anode. Reversing the applied electric field leads to a corresponding reversal of this redox process and thus the mechanism is also bipolar. Famous examples for valence change memories are based on TiO_2[15,18] or $SrTiO_2$[19].

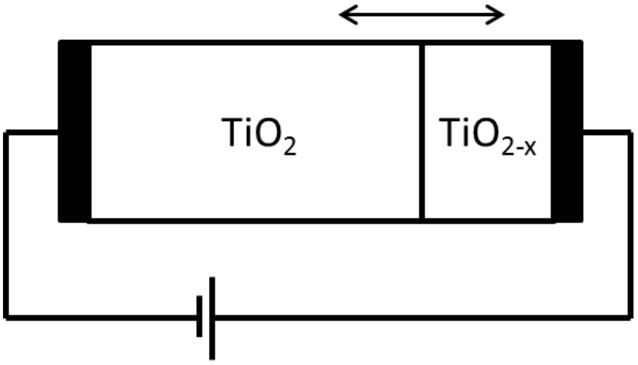

Figure 1.7. Illustration of a TiO_2 – based resistive memory. Upon an applied bias, the relative thickness of the conductive species can be increased or decreased, resulting in a distinct resistance change.

In order to obtain a higher operational stability of such devices, another approach apart from pure filament growth was suggested. By deliberately introducing a thin layer (2 nm - 5 nm) of the oxide with higher conductivity at the interface between insulating oxide and electrode, it is possible to actually manipulate the thickness ratio of conductive to non-conductive material upon an applied voltage due to the migration of oxygen vacancies (Figure 1.7). This approach has recently attracted considerable interest, as impressive performance parameters (switching speed ~ 10 ns, endurance > 10^{11} cycles, cell size ~30 nm) had been demonstrated in Pt/Ta_2O_{5-x}/TaO_{2-x}/Pt devices.[20]

Thermochemical processes

The basic idea behind thermochemical processes is the controlled partial dielectric breakdown of an insulator sandwiched between two metal electrodes. The breakdown itself can be explained by different mechanisms including electrode metal transported into the insulator, carbon contaminations stemming from the device fabrication or decomposition of the insulator material.[21] In all cases, a conductive filament is thought to be the result. The use of a current compliance during the switching event ensures that this filament is not too ‘strong’ and the breakdown is reversible. The filament can be erased by thermal dissolution induced by Joule heating due to power dissipation along the filament. Thermochemical switching has been observed in a wide variety of systems, e.g. Pt/NiO/Pt devices[22].

2 Introduction to Organic Memory Devices

Resistive switching can occur in various forms and characteristics. This chapter focuses on one of the most common types, namely unipolar resistive switching. On the basis of the data obtained from measurements on ITO/Alq3/Ag devices, the features of unipolar resistive switching are discussed. A possible strategy to implement unipolar resistive switches into array structures is presented.

The rapid development in the field of organic electronics started with the discovery of electrical conductivity in doped poly(acetylene) in 1977[23]. Since then, organic semiconductors have been successfully applied in devices like OLEDs[24] and PLEDs[25], organic photovoltaic devices (OPV)[26], photodiodes (OPD)[27], field-effect transistors[28], electrochemical cells[29], rectifiers[30], etc. Although the limitations of organic semiconductors are omnipresent,[31–33] advantages like the possible mechanical flexibility, their tailorabilty with respect to electro-optical properties, cheap fabrication, light weight and low energy consumption justify industrial and academic research. Furthermore, the properties of organic materials allow for environmentally friendly 'green' fabrication routes. Various innovative printing techniques are capable of contributing to this ambitious goal with benefits like reduced material waste due to additive maskless patterning and low-temperature processing.[34]

Resistive switching effects in organic devices have already been observed around the 1970s in various organic dielectric films such as poly(styrene).[35,36] Between 1980 to 2000 the work on this effect can be considered as more sporadic, but resistive switching in organic devices was re-discovered by the group around Yang Yang.[37] Since then, a multitude of devices and novel materials have been presented. The vast manifold of published devices is distinguished by nearly every structural parameter: different electrode materials, organic semiconductors/insulators or modified organics by additional inorganic nanoparticles turned out not to influence the switching characteristics.[13] Up to now, no convincing structure-to-property relationship has been established.

2.1 Features of Unipolar Organic Resistive Switching Devices

Two switching behaviors, unipolar (writing and erasing with identical polarization of the electric field) and bipolar (writing and erasing with opposite polarization of the applied electric field) have been presented for inorganic resistive switches. The same is true for their organic counterpart, where bipolar[10] and unipolar switching cells are reported. In this work, only unipolar devices are discussed. The typical current-voltage- (IV-) characteristics and other important features are described in the following.

Current – Voltage Characteristics

Figure 2.1 shows a typical IV-characteristic of an ORS. At low bias values, two resistance states can be clearly distinguished: A high resistance state (HRS) (around 1 GΩ at 1 V) and a low resistance state (LRS) (down to 1 kΩ at 1 V) represent the outer resistance levels of such a device. During the first sweep, an ORS is in its HRS. At a characteristic voltage V_{th}, a steep increase in current (threshold) switches the device from its HRS to its LRS. For $V > V_{th}$ the IV curve shows a region of negative differential resistance (NDR) associated with decreasing current as the voltage is increased. The resistance is set back to its initial HRS by applying a bias at the end of the NDR region.

Both resistance states are non-volatile, i.e. their states are preserved even if the supply voltage is removed. From this curve, the necessary bias levels required to switch or read the device can be identified. To read-out the device, any voltage well below V_{th} (e.g. 1 V) is suitable. To switch the device from HRS to LRS a voltage slightly above V_{th} is used and in order to set the device back from LRS to HRS, a voltage at the end of the NDR has to be used. For a typical memory operation, it is certainly not necessary to record a full IV-sweep in order to switch the device; applying a single short read, write or reset voltage pulse is sufficient to switch or read the device. This is demonstrated in a cycling test shown in Figure 2.2 (right) where the device was continuously switched between HRS and LRS by applying the corresponding read write and erase levels.

Further, mirror symmetry of the device with respect to bottom and top electrode material (or its workfunction) results in equally symmetric IV-curves (Figure 2.2, left)

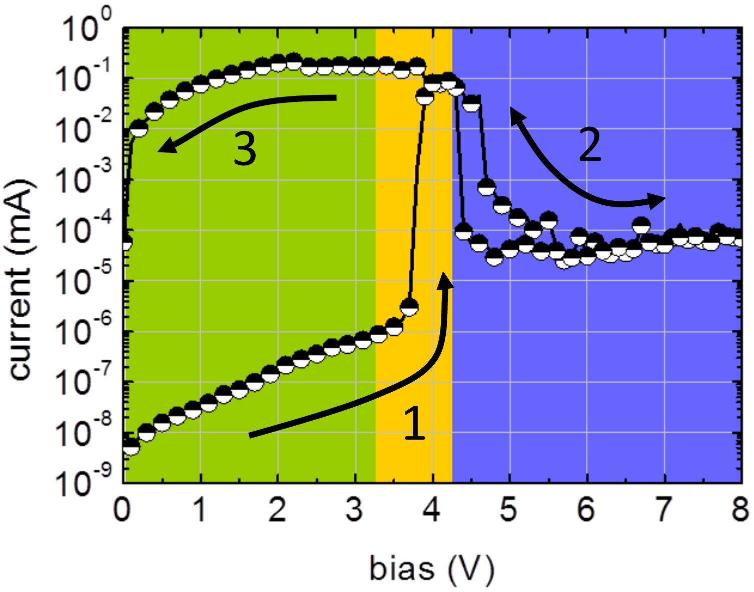

Figure 2.1. Typical IV-characteristics of an organic resistive switch: Two distinctive resistance states are present at low voltages (green), representing the read-out margin. A current threshold can be found around 4 V, representing the switching from the devices from its HRS to its LRS (yellow). For higher bias levels, a pronounced region of NDR is observed. Applying a bias at the end of this NDR region sets the device back to its initial HRS (blue). All devices were initially in their HRS. The curves were recorded as a double-sweep starting from 0 V to 8 V and again back to 0 V. The arrows indicate the sweep sequence.

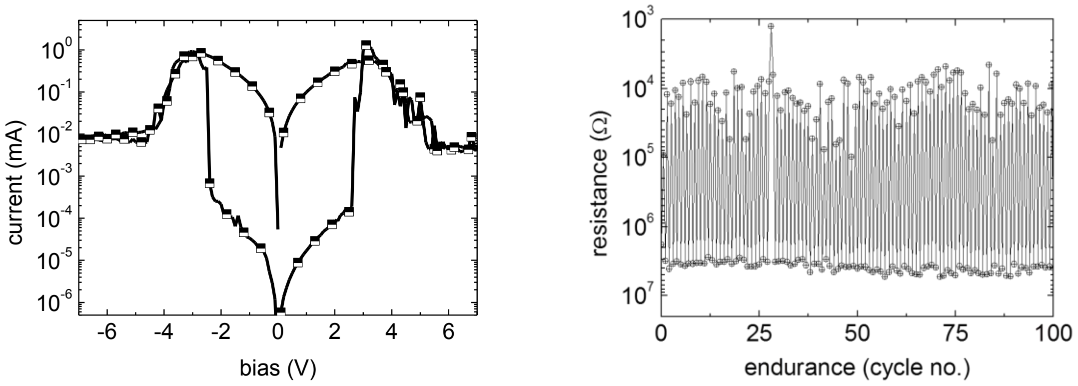

Figure 2.2. Symmetry of the IV-curve (left) and cycling test (right) of an ITO/Alq3/Ag device. To switch the device from HRS to LRS and back a bias of 3 V and 7 V was applied, respectively. The states were read-out at 1 V

Intermediate Resistance States

A distinct feature of ORS, is the possibility to address not only the two outer limits (HRS and LRS) but also resistance states in-between, called intermediate resistance states (IMRS). An ORS is therefore capable of storing multi-bit values which is directly related with the *more Moore* concept, as described in the introduction.

An IMRS can be written by selectively applying a bias within the NDR region.[38,39] Figure 2.3 (left) demonstrates this for 4 different intermediate states: the higher the writing voltage, the higher the resulting resistance in the following IV-curve. Notably, all these states are as well non-volatile and stable even if the bias is removed. Figure 2.3 (right) shows the possibility of writing 12 different resistance states from 1 kΩ up to several 10 MΩ by applying the routine as described before.

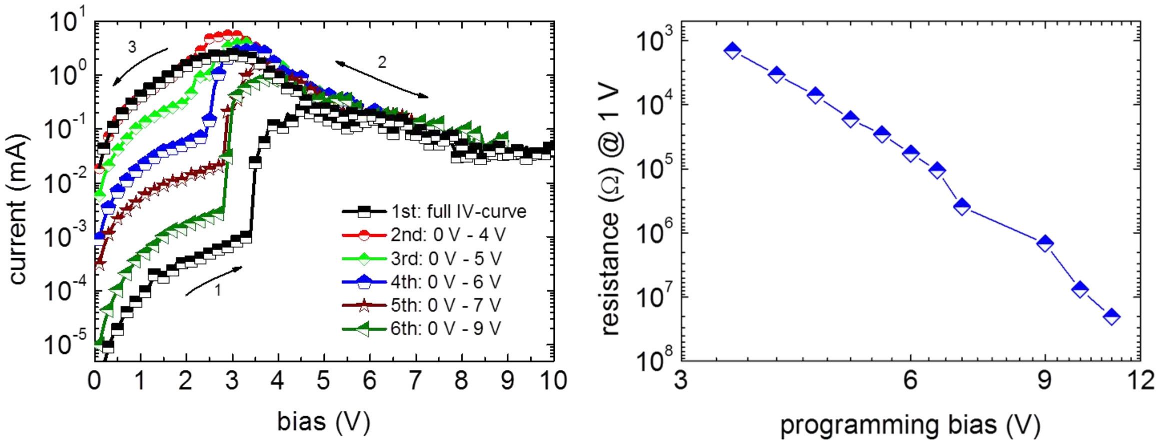

Figure 2.3. Addressing intermediate states by applying a bias in the NDR region (left). In this way 12 IMRS were written (right).

Alternatively, IMRS may be written by adjusting a suitable current compliance (c.c.) during the switching event.[40,41] This principle is demonstrated in Figure 2.4. The dark blue curve depicts the device characteristics recorded without c.c. For the other curves a c.c. was used (1 µA, 10 µA, 100 µA), obviously influencing the switching behavior of the device. After the switching event the resistance of the device was measured by applying the read-out voltage 1.5 V (without c.c.). The sweep without c.c. resulted in device resistance of 2.5 kΩ. For a c.c. of 100 µA, 10 µA and 1 µA the resulting resistance was of 20 kΩ, 100 kΩ and 3 MΩ, respectively. Note that the device was set back to its HRS after each curve. The capability of addressing all resistance values between HRS and LRS forms a quasi-continuum of memory states, making this essentially an analogue device with deep implications in other fields of application like neuromorphic computing.[42]

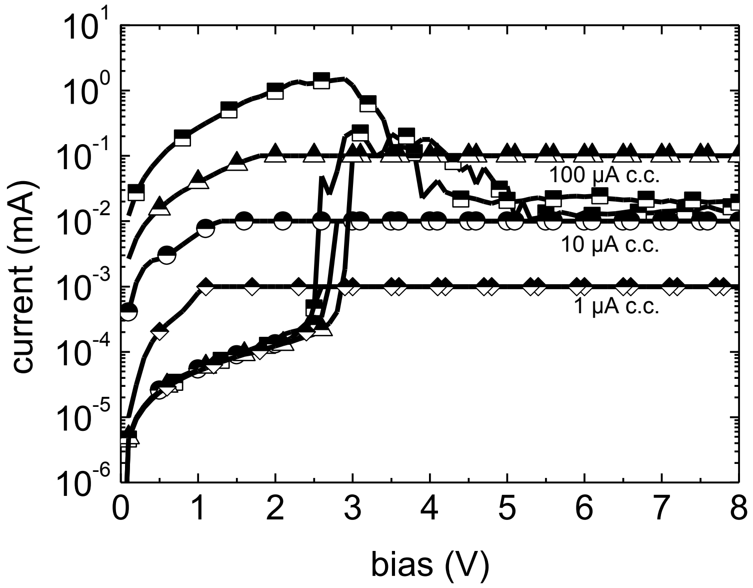

Figure 2.4. Programming of intermediate resistance states using different c.c. values (1 µA: diamonds, 10 µA: circles, 100 µA: triangles). IV-curve with no c.c.: squares

Material independence

A large number of devices distinguished by the used organic materials, interlayer materials and electrodes were fabricated throughout this work. Resistive switching was found for all of them. Three exemplary IV-curves are shown in the following: First, a device based on an commercial photoresist: ITO/40-XT Photoresist/Ag configuration (Figure 2.5); Second, a device with an gold-nanoparticle interlayer: ITO/Alq3/Au/Alq3/Ag (Figure 2.6) and third, a device with an organic hole-transporting semiconductor as organic: ITO/N,N′-Di-[(1-naphthyl)-N,N′-diphenyl]-1,1′-biphenyl)-4,4′-diamine (NPB)/Ag (Figure 2.7). It is evident that the curves are qualitatively equal and differences only occur in the absolute current levels.

A summary of the IV-curves of all fabricated devices can be found in the Appendix.

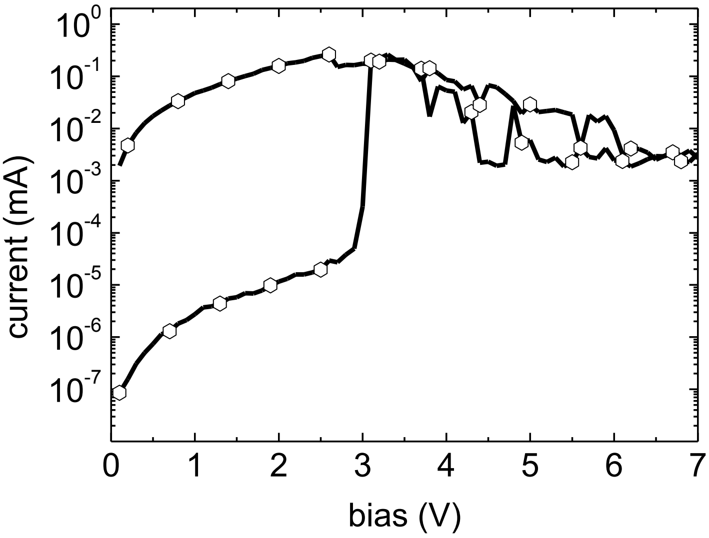

*Figure 2.5. IV-characteristics of an ITO/40-XT Photoresist/Ag device. The device was initially in its high resistive state; Sweeping from 0 V to 7 V leads to a current threshold at ~3.1 V and a region of negative differential resistance from 3.5 V to 7 V; the device remains in a low resistive state when sweeping from 7 V back to 0 V. The ON/OFF-ratio at 1 V is 1.7*10^4. The ITO electrode acts as positive contact.*

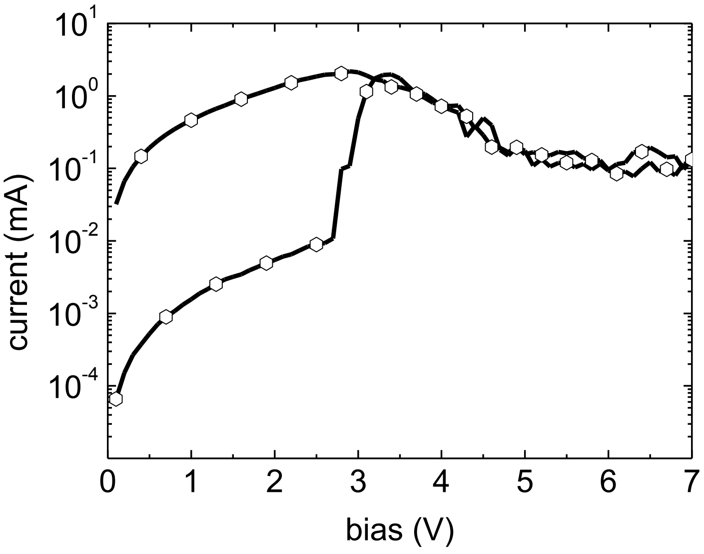

*Figure 2.6. IV-characteristics of an ITO/Alq3/Au/Alq3/Ag device. The Au - intermediate metal was nominally 2 nm thick. The ON/OFF-ratio at 1 V is ~3*10^2. The ITO electrode acts as positive contact.*

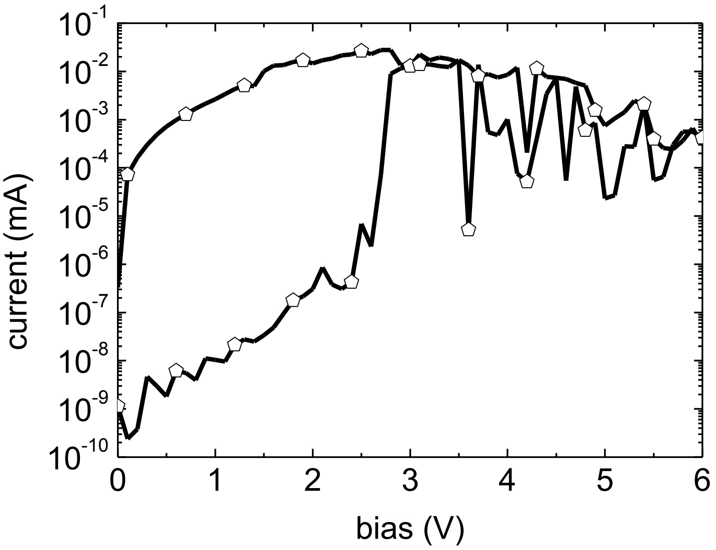

*Figure 2.7. IV-characteristics of an ITO/N,N'-Di-[(1-naphthyl)-N,N'-diphenyl]-1,1'-biphenyl)-4,4'-diamine (NPB)/Ag device. The ON/OFF-ratio at 1 V is ~2.6*10*^{5}*. The ITO electrode acts as positive contact.*

2.2 Integration into Memory Arrays

The integration of a manifold of such 2-terminal resistive switches into crossbar arrays significantly complicates the situation. A passive matrix structure would inevitably lead to a parasitic cross-talk during addressing of single elements caused by significant current bypassing through adjacent non-addressed elements in their LRS (Figure 2.9).[43] To overcome this issue, an additional selector device has to be integrated in series with each cell. For unipolar resistive switches this element can be a rectifying diode. In contrast to a planar transistor, a diode is also a 2-terminal device and therefore does not limit $4F^2$ integration. The integration of ORS with organic diodes (OD) is still rarely presented, mostly due to the strict requirements imposed by the ORS with respect to the absolute current levels of the rectifying element: First, a low onset voltage (< 1 V) and a forward current higher than I_{ON} of the ORS, as the diode should not act as a bottleneck for any of the memory functionalities in forward direction. Second, a low reverse current is required. Under reverse bias, all memory related properties should be suppressed and only reverse current of the OD should dominate, enabling for a proper blocking of cross-talk stemming from neighboring elements. All requirements are graphically summarized in Figure 2.8.

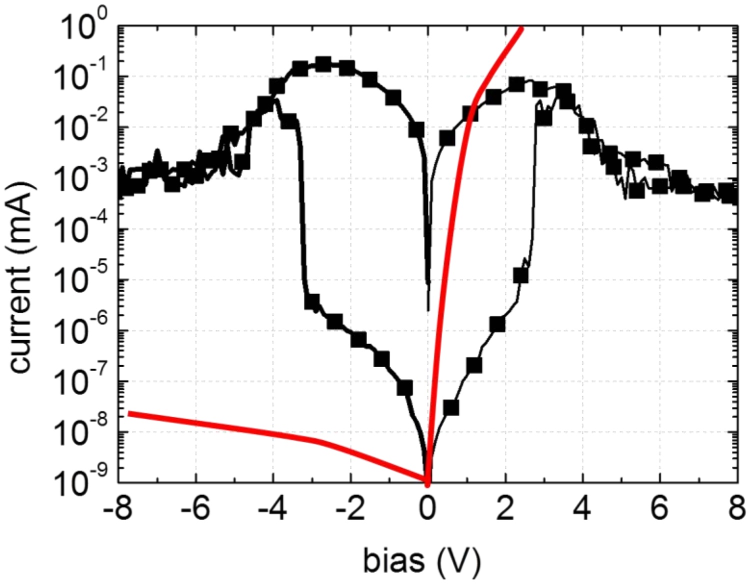

Figure 2.8. The black IV characteristic shows a typical unipolar memory device behavior. To operate the individual memory devices without limitations by the diode an ideal diode characteristic was added, indicated by the red line: In reverse direction, the diode current should be reasonably smaller than the HRS current. In forward direction, the diode characteristics should not limit read-out and switching behavior of the ORS.

The vertical integration of a diode and a resistive switch is usually denoted as 1Diode – 1Resistor setup (1D – 1R). Lee et al. were the first to demonstrate a fully functional 1D-1R system.[44] However they used inorganic Si-based diodes which doubtlessly reduce the advantages of organic electronics. Jen at al. were the first who implemented organic Au/P3HT/Al rectifying devices in series which each ORS for array sizes up to 8 by 8 elements.[45,46]

A priori, the required diode parameters can be estimated using the situation as depicted in Figure 2.9: A noise path must cross an odd number of elements (at least 3) with alternating polarity of the diode, which means that the path includes at least one diode polarized in reverse. Each node can thus provide a current limited by the reverse current I_0 of the diode. Any device collects the current from all the N-1 elements on the same electrode line, thus a maximum noise current for every element is in the order of $N \cdot I_0$. Multiplying this with N lines in the array an upper boundary (worst case) for the noise current in the order of $N^2 \cdot I_0$ can be obtained. Nevertheless, the state of a single memory element can be read out correctly, even if the HRS of the memory is below the noise threshold: If the read pulse leads to a high current, the element is in its LRS (ON state). If the maximum noise current (or smaller) is detected, the element can be considered to be in its HRS (OFF state). Therefore, for arrays an *adapted* I_{ON}/I_{OFF} *ratio*, the ON to maximum-noise ratio (R) is of interest:

$$R = \frac{I_{ON}}{N^2 I_0}$$

Equation 1. Definition of the adapted I_{ON}/I_{OFF} *ratio*

Already for rather small array sizes this equation implies the need for a high performance rectifying diode with maximum reverse current in the order of several nA to ensure a moderate R value of 100. To achieve these strict requirements with an organic Schottky diode, several issues have to be considered: (1) the organic material has to exhibit high charge carrier mobility (like Pentacene[30] or P3HT[45,46]). (2) the electrode configuration has to be highly asymmetric: On the anode side high work function materials (e.g. Au, MoO_3[47]) have to be used, while on the cathode side materials with a low work function are applied (e.g. Ca, LiF, PEIE[48], Al[49]). (3) The diode reverse current can be further reduced by increasing the thickness of the organic layer (> 500 nm) and thus reducing parasitic current.

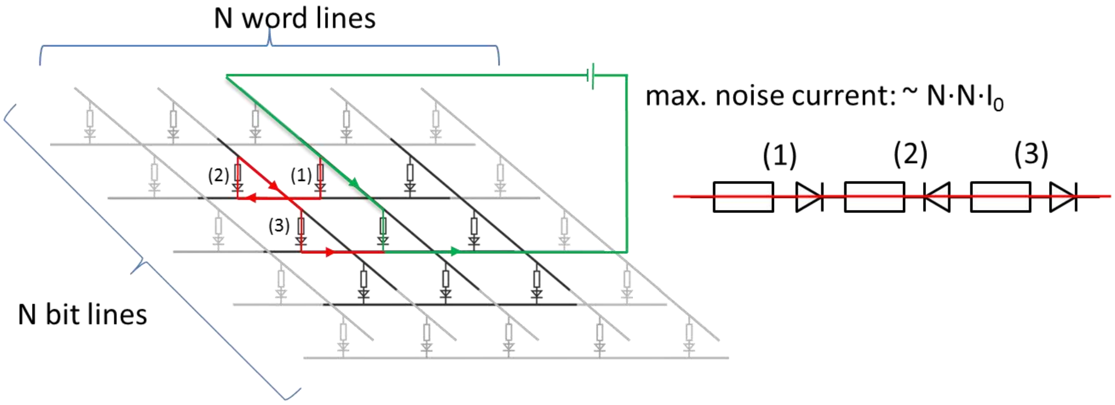

Figure 2.9. Illustration of the origin of parasitic current in crossbar array structures. The green line highlights the desired current pathway, while the red line shows one of the possible parasitic pathways. At least three nodes (always an ODD number) are involved in such a current bypass. A maximum noise current in the order of $N^2 * I_0$ *(with N, the number of bit and word lines) can be estimated from this argumentation.*

Demonstration of the cross-talk problem for a 2 by 2 array test-structure

In order to show the impact of the implementation of a series diode, 2 by 2 arrays with and without additional series diode have been fabricated. Four ITO/Alq3/Ag ORS were implemented. Before they were measured in the actual crossbar grid, the worst case pattern (three devices in LRS, one in HRS) was written in the mutually isolated devices. The resulting resistance values for single pixels are indicated in Figure 2.11a. Afterwards they were connected to a 2 by 2 matrix and the resistance was read-out again. Devices 1-3 are still in their LRS, during read-out of device 4, however, a low resistance is apparently measured from the periphery caused by the low resistance of the three adjacent elements. Thus, no proper read-out is possible (Figure 2.11b).

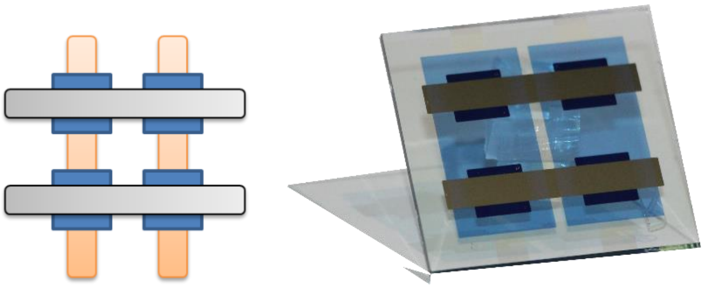

Figure 2.10. Sketch and photograph of a 2 by 2 array. The blueish regions indicate the pentacence thin-film.

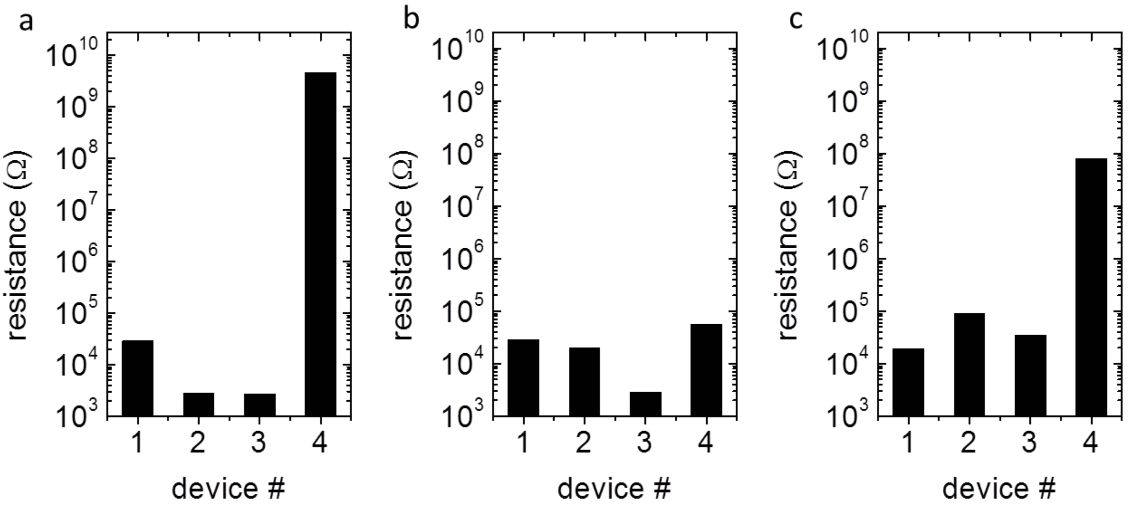

Figure 2.11. Demonstration of the impact of parasitic current for arrays with and without additional series diode. Devices 1 – 3 are set to their LRS state, whereas device 4 is in its HRS. a) no diode, devices electrically isolated from each other. b) no diode, devices connected in an 2 by 2 matrix. c) with series diode, devices connected n an 2 by 2 matrix.

To overcome this issue, four diodes (Au/MoO_3/Pentacene/Ca/Al) were evaporated on top of each element. The IV-curve of such a stack is depicted in Figure 2.12. The resistance of the diode operated in reverse direction now blocks the unwanted current path through adjacent elements and a proper read-out of device 4 is possible. Note that the parasitic current through the diode influences the HRS negatively as a reduction of the HRS of nearly two orders of magnitude is found. However, a clear distinguishing between LRS and HRS is now possible (Figure 2.11c).

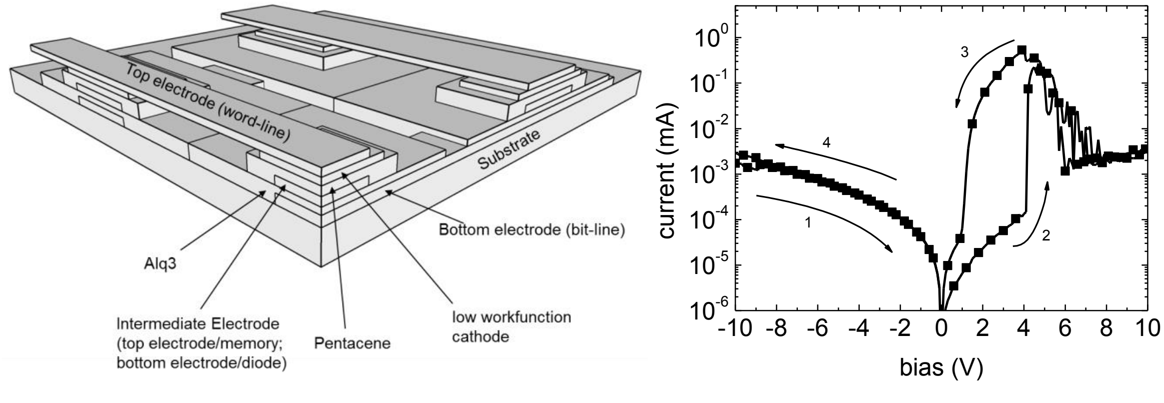

Figure 2.12. Scheme of the fabricated 2 by 2 array (left). IV-characteristics of a single cell of the array. Bistability is effectively suppressed under negative bias. The arrows indicate the direction of the measurement sequence (right).

3 Unravelling the Nature of Resistive Switching in Organic Memories

Despite considerable research efforts in the field of organic resistive switches, the nature of the switching mechanism is still a subject of debate. A general and consistent explanation about all observations is still missing, making the reliable fabrication and engineering of the devices and their properties challenging and clearly limits widespread applications. This chapter presents a novel approach for the investigation of ORS based on the circuit model for photovoltaic devices. The obtained parameters, namely the open circuit voltage (V_{oc}) and the short circuit current (I_{sc}), are used to interpret the memory functionality, and lead to solid evidence that the actual cause of unipolar resistive switching is based on the formation of conductive pathways between the electrodes (e.g. filaments), rather than on charging effects. Impedance spectroscopy is performed in order to distinguish between the capacitive and ohmic influence. Furthermore, the model is extended to devices which cannot be investigated by photovoltaic means, i.e. devices employing insulating materials. From the manifold of the fabricated devices, a series of model devices were selected to demonstrate the origin of resistive switching step by step.

Parts of the content of this chapter are published in:
S. Nau, S. Sax, E. J. W. List-Kratochvil, ‚Unravelling the Nature of Unipolar Resistance Switching in Organic Devices by Utilizing the Photovoltaic Effect‘, Adv. Mater. 2014, 26, 2508.
The author of this thesis planned and performed all experiments, the data analysis and wrote the manuscript.
S. S. and E. J. W. L.-K. supervised the work.

3.1 The Debate about the Working Mechanism

Despite considerable research effort in this field, the true nature of resistive switching is uncertain and a manifold of different switching mechanisms have been proposed. The most prominent are discussed in this sub-chapter.

Simmons-Verderber (SV) mechanism

J.G. Simmons and R.R. Verderber published a work in 1967 exploring resistive switching effects in Al/SiO_x/Au diodes (Figure 3.1).[50] Back then, it was claimed that the electrolytic injection of gold ions into the SiO_x dielectric introduces an impurity band in the semiconductor which is mainly responsible for electrical bistabilty.

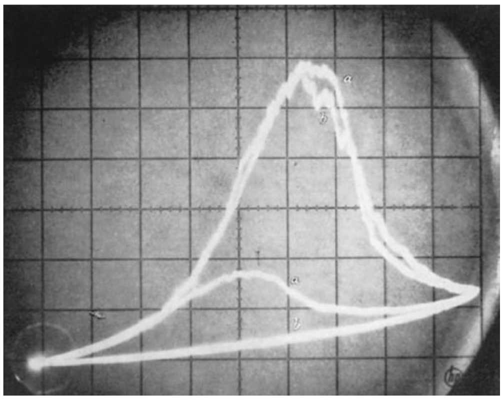

Figure 3.1. IV-curves obtained from an Al/SiO_x/Au device according to Simmons and Verderber.[50]

In dependence of the applied bias, charge carriers are either trapped or de-trapped at these impurity sites. In the case of trapped charge carriers the related space-charge field leads to an inhibition of further charge carrier injection and thus a high resistance of the device stack. As soon as the charge carriers are de-trapped (around the threshold voltage) this space-charge field breaks down and charges can be injected again - the device is found to be in its LRS. The NDR-region, which has also been observed back then, was assigned to the gradual trapping of charge carriers, giving a smooth decrease in current.

The description of this mechanism was taken up by Bozano et al.[51] as they applied the theory to their observations from organic Al/Alq3/Al/Alq3/Al triple-layer devices. The nominal thickness of the intermediate aluminum was kept very thin (less than 10 nm) in order to guarantee separated particles and prevent percolation. It has been shown that these particles are covered with a thin layer of the oxidized dielectric species of Aluminum - Al_2O_3. These core-shell nanostructures are meant to act as charge traps equal to the impurities in SiO_x from the original work of Simmons and Verderber (Figure 3.2). In the following work of Bozano et al., a large degree of material insensitivity of the switching mechanism was found as they used a multitude of hole and electron conducting organic semiconductors. Further also the electrodes (Al, ITO, Cr, Cu, Ni, Au) as well as the granular interlayer (Mg, Ag, Au, Al, Cu) was exchanged. Qualitatively, the observed IV-curves were found to be largely equal.[52] Various groups ascribed their results to be of this type of switching. Mostly, different trapping spots are introduced into the organic layer, including graphene and graphene oxide[53–56], carbon nanotubes[57], silver nanodots[58,59], ZnO nanorods[60], Zinc Selenide[61], silicon oxide nanoparticles[62] or organic materials like phenyl-C61-butyric acid methyl ester (PCBM)[63–65].

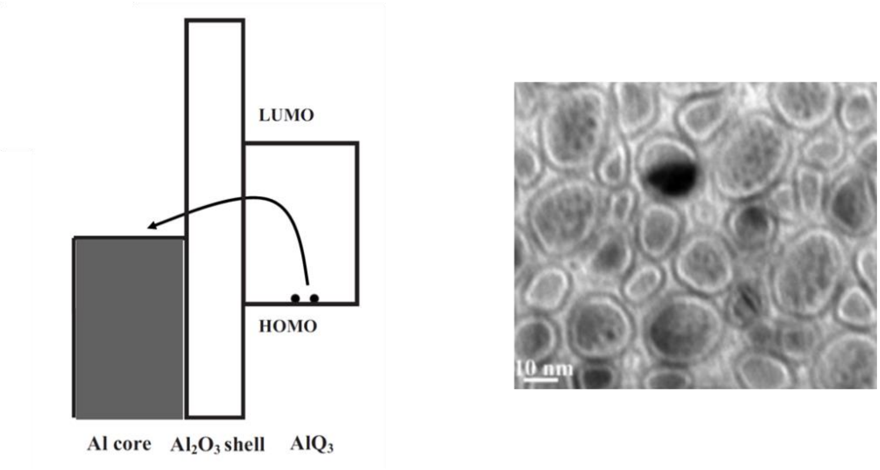

Figure 3.2. Claimed charge trapping mechanism. Upon a high electric field, electrons are tunneling trough the insulating Al_2O_3 shell into the metallic core (left). TEM picture of $Al:Al_2O_3$ core shell nanoparticles . Taken from [38] and modified.

Various ideas have been derived from the SV-mechanism, e.g. bistability in terms of coulomb blockade[66]. Chan et al. on the other hand claimed exactly the opposite with respect to filled traps and the corresponding resistance state.[67] In that particular paper, it was described that as soon as the traps in the organic matrix are filled, the conductivity increases resulting in a low resistance.

Another extensively used charge-based model to describe switching are charge transfer effects in donor-acceptor systems, as discussed in the following section.

Donor-Acceptor Charge Transfer Mechanism

This theory was especially put forward by the group Yang Yang, who initially demonstrated the mechanism on the basis of a three component blend consisting of poly(styrene) (PS), 8-hydroxyquinolin (8HQ) and 1-dodecanethiol protected gold nanoparticles (AuNP), sandwiched between two aluminum electrodes. It was proposed that under the high electric field a charge transfer between the AuNP and 8HQ occurs. In the high resistive state, the concentration of free charge carriers is low. As soon as the applied electric field is larger than the threshold voltage, a charge transfer from the highest occupied molecular orbital (HOMO) of 8HQ through the insulation capping layer of the AuNP is believed to happen. Afterwards, the HOMO of 8HQ is partially filled, resulting in a higher conductivity of the system due to free electrons in the now vacant electron state (Figure 3.3).[68] Similar mechanisms have also been described for various other material combinations including polyaniline nanofiber:AuNp blends[69], Cu:tetracyanoquinodimethane blends (Cu:TCNQ)[70] or PS:tetrathiofulvane:PCBM[71] blends.

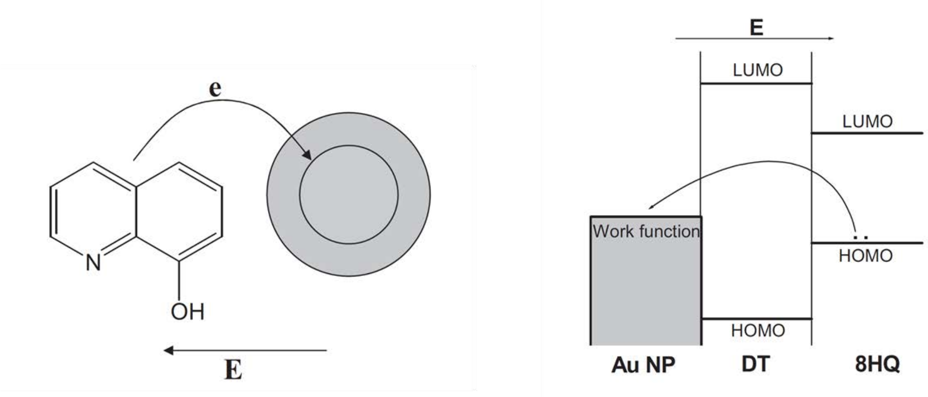

Figure 3.3. Proposed charge transfer mechanism. After a charge transfer from 8HQ to an AuNP, its HOMO is partially filled, leading to a modification of its conductivity. Taken and modified from [72]

The SV-model and derived 'charge-based' theories are still extensively used to describe resistance switching in ORS[58,63,73–79], even though there is significant disagreement between the predictions of the model and experimental observations; e.g. pristine ('as prepared') devices are expected to be in their LRS (particles uncharged) during the first measurement, which is typically not observed.[80] Also, it was reported that the device capacity is constant, regardless of the resistance state.[81]

Formation of Filaments

Switching of the device resistance was explained by the formation of highly conductive and localized pathways (filaments), essentially shortening the organic layer between the two electrodes.[82] Various experiments evidenced the presence of such filaments. Cölle et al. observed the appearance of localized spots on the device area by means of infrared microscopy upon switching to the LRS.[83] Various groups claimed the direct observation of filaments using electron microscopy.[84–86] Moreover, the found device area independence of the absolute LRS-current[87], delayed switching effects[88] and conductance quantization[89] can only be explained by filament formation processes. Although there is evidence that filaments are present in organic devices, the nature of their composition is not well understood. In the simplest case, a filament is of strictly metallic origin, where redox-driven processes[84,90,91] or thermochemical reactions[17] are held to be responsible for the formation. Also the migration of polarized metal atoms from the electrodes was suggested to play an important role.[92] As an alternative mechanism, local carbonization[35,36] of the organic material due to pyrolysis was proposed. Furthermore Österbacka et al. demonstrated that high-conductivity pathways may also originate from the alignment of PCBM molecules with higher conductivity in an insulating matrix.[93]

The typical unipolar IV-curve can be well explained by the filament model. At the threshold voltage, one or possibly many filaments are fully formed resulting in a LRS. With increasing bias and current, the power dissipation by Joule heating in the filamentary channel increases, resulting in a gradual degradation (or thinning) of the filament, explaining the NDR region.[94] Also the symmetric IV-curve is not in contradiction with the model, since both electrode materials can contribute to the formation of a filament. In any case, the unintended incorporation of metal during the deposition of the top electrode through film non-uniformities is thought to be significant to induce/promote the growth of a filament.[95]

Conformational changes

Changing the conformation of single molecules or clusters is often accompanied by a modification of the effective conjugation length and thus of its conductivity. This effect is is also held responsible for switching effects in organic devices. However, a strong material dependence has to be expected in this case. The theory was developed from Pal et al., who claimed that electroreduced Rose-Bengal molecules (Figure 3.4), with its manifold of energetically possible conformations, may undergo an conformational change upon high electric fields.[96] These devices have later been reproduced by another group who found strong evidence that switching in Rose-Bengal films is more likely to be due to the formation of conductive filaments.[97]

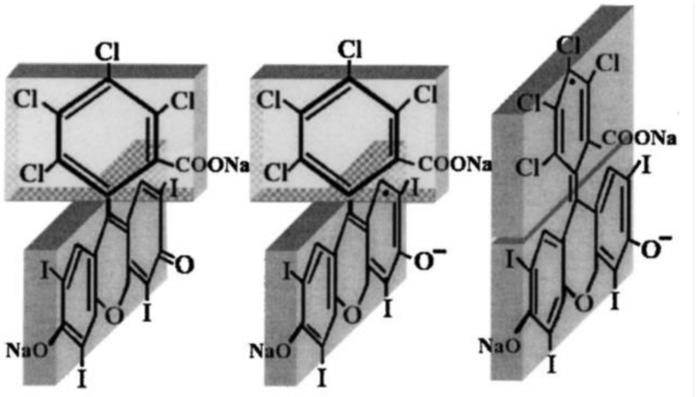

Figure 3.4. Resistive switching due to a conformational change in Rose-Bengal molecules. Initial state, perpendicular planes (left); electroreduced state with perpendicular planes (middle); electroreduced state with coplanar planes (right). Taken from [96] *and modified.*

Similar mechanism were also claimed for poly(vinyl carbazole) (PVK) based devices, where it was possible to achieve a certain twist of the PVK side-chain unit in dependence of the length of various spacer groups. [98,99]

Remarks

From the manifold of presented devices and proposed working mechanisms it is evident that there is still a lack of knowledge about the actual origin of resistive switching. It cannot be excluded that several of the above mentioned mechanisms contribute to the device characteristics, however it is difficult to believe that fundamentally different working mechanisms lead to one and the same IV-curve. Often not all of the necessary and relevant investigations are carried out and a serious evaluation of the data presented in literature is not possible. For demonstration reasons a device – commonly known as the prototype for the charge-transfer mechanism[100] – was reproduced during this work. Indeed this device (Al/PS:8HQ:AuNP/Al) exhibited resistive switching. However, it turned out that both control devices (Al/PS/Al, Al/PS:8HQ/Al; not shown in the original publication), also did so in absence of AuNP (Figure 3.5). From this point of view the donor-acceptor mechanism has to be excluded for this type of device.

The following part of this chapter provides a detailed investigation on the actual origin of the working principle of unipolar resistive switching.

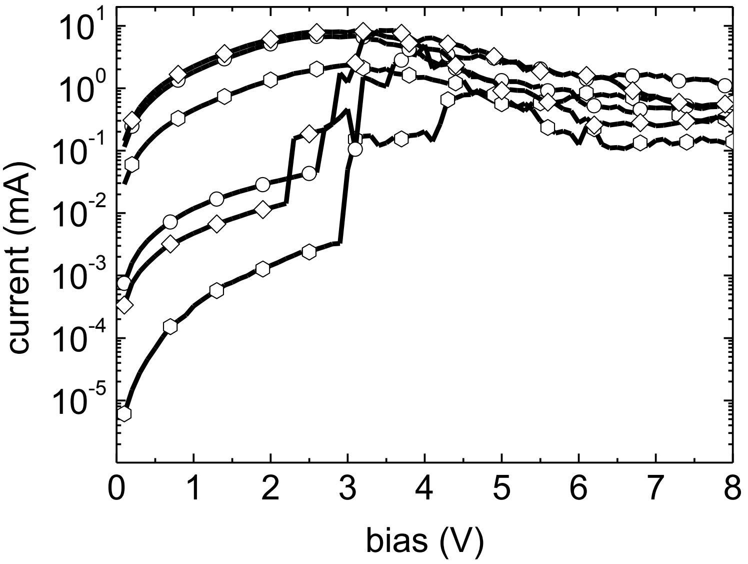

Figure 3.5. IV-characteristics of an Al/PS/Al device (hexagons); an Al/PS:8HQ/Al device (circles) and an Al/PS:8HQ:AuNPs/Al (diamonds).Obviously, the influence of AuNP on resistive switching is negligible.

3.2 Basic I-V characterization

Three prototypical resistive switching devices were chosen for the investigations of the working mechanism: **I**: an ITO/Aluminium-tris(8-hydroxychinolin) (Alq3)/Ag single layer system, **II**: a tri-layer approach ITO/Alq3/Al/Alq3/Ag, and **III**: an Ag/Poly(methyl methacrylate) (PMMA)/Ag configuration. The basic IV – characterization from these assemblies are depicted in Figure 3.6.

Device **I** can be considered as the reference device to the tri-layer device **II**, one of the most commonly presented device types which is also regarded as a prototypical SV - nanotrap memory[80,101]: the thin intermediate layer (~ 10 nm) of aluminum is slowly thermally evaporated onto the first organic layer, forming Al-oxide covered particles, which are meant to act as charge traps. Obviously both device structures expose a similarly shaped IV-curve. For device **III** a spin coated layer of PMMA was chosen, being a model assembly for devices with insulating organic materials. Also here, qualitatively the same IV-characteristics was found during these experiments, making the claimed role of π-conjugation and metallic nanotraps questionable already at this point.

As depicted in Figure 3.6, all devices have two clearly distinguishable and non-volatile resistance states for bias values < 2.7 V, a distinct HRS to LRS threshold voltage at 2.7 V – 3.8 V and a region of NDR between 4 V and 8 V. The shape of the IV-curve as well as the location of the threshold can be considered as prototypical for most reported unipolar ORS systems. Nevertheless, a major difference of the characteristics is defined by the absolute current through the device, either of the LRS or the HRS state. For device **III** with the insulating PMMA as active material, the HRS current is in the order of 10 pA at 1 V. For device **I** and **II**, using the semiconducting Alq3 as the organic material**,** the HRS current is increased by two orders of magnitude when compared to device **III**. On the other hand, the variations between the LRS currents from devices **I-III** are significantly smaller and in the range of 70 µA to 150 µA (at 1 V). Consequently, the ratio between the individual resistance values of the HRS and LRS at 1 V (ON/OFF – ratio) was found to be $1.2*10^5$ for **I**, $1.1*10^4$ for **II** and $2.9*10^6$ for **III**, respectively. In addition to these variations of the current levels, the pre-conditioning or forming procedure needed to establish the resistance switching is determined by the actual device setup. While for device **II** bi-stability was immediately present within the first sweep, the other configurations typically developed bi-stability after a forming procedure of about 10 (device **I**) and about 50 (device **III**) IV-sweeps.

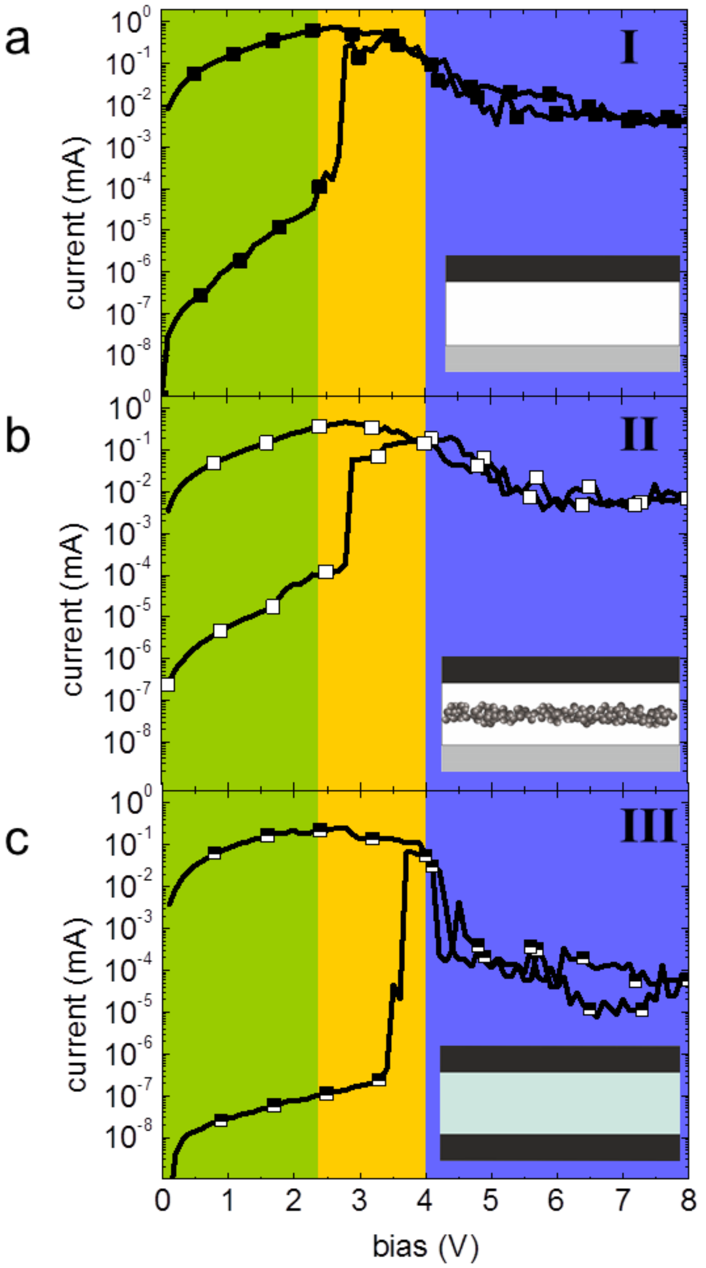

Figure 3.6. Current-Voltage characteristics of device I: ITO/Alq3/Ag (a, upper figure); device II: ITO/Alq3/Al/Alq3/Ag (b, middle) and device III: Ag/PMMA/Ag (c, lower). The colored areas indicate the three specific regions: For each device two distinctive resistance states are present at low voltages (green), representing the read-out margin. A current threshold can be found between 2.4 V and 4 V, representing the switching from the devices from their HRS to its LRS (yellow). For higher bias levels, a pronounced region of NDR is observed. Applying a bias at the end of this NDR region sets the device back to its initial HRS (blue). All devices were initially in their HRS. The curves were recorded as a double-sweep starting from 0 V to 8 V and again back to 0 V. Sketches of the general setup are shown in the insets.

3.3 Photovoltaic Investigations

Device **I** and **II** can in principle be also considered as organic photovoltaic devices. Irrespective of the cause of their electrical bistability, the measurement of photovoltaic parameters from these devices may deliver insight to the underlying working mechanisms.[102,103] When the organic semiconductor of the memory device gets illuminated with a wavelength matching with its optical bandgap, photovoltaic parameters such as the short circuit current I_{sc} (current at zero bias) and the open circuit voltage V_{oc} (voltage at zero current) can be determined. The presented devices are not designed as organic (bulk) hetero-junction cells and extractable charge carriers and the resulting photocurrent is therefore mainly generated at the specific organic semiconductor/electrode interfaces.[104] The built-in potential is then largely determined by the work function difference of the two electrode materials determining the obtained open circuit voltage. Although this setup is a rather inefficient solar cell, one can gain insight into the working mechanism of the memory device.

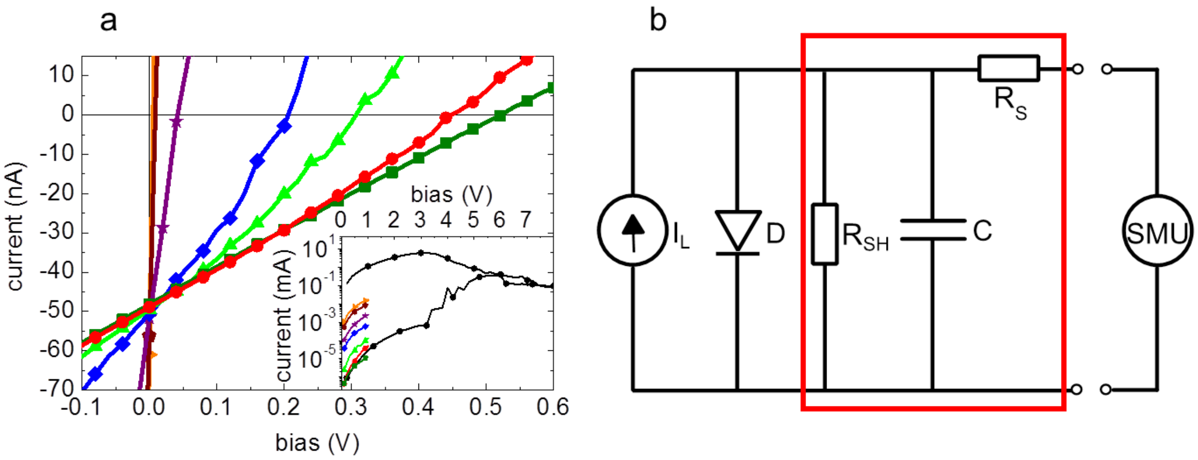

Figure 3.7. Photovoltaic investigation of a organic memory device: a) IV characteristics of different intermediate resistance states from a device of type I under illumination. The inset shows a typical IV characteristics in a half-logarithmic scale with indicated intermediate state b) Equivalent circuit diagram of an organic photovoltaic device, consisting of a current generating element (i.e. free charge carriers generated by light), a diode (D, accounting for the rectifying ability), a series resistor (R_S, the bulk and contact resistance) and a shunt resistors (R_{SH}, accounting for power dissipation pathways e.g. by material defects or pinholes). The capacitive contribution to the model is considered by C. The red square highlights the components relevant for the switching mechanism.

It is well known that the described ORS devices can take stable intermediate resistance states in-between the two extremes by applying a bias in the NDR region (see chapter 2.1). As indicated in Figure 3.7a (inset) seven different resistance states were established in this way for device **I** and for each state the IV-curve between -0.1 V and 0.6 V was recorded under constant illumination from a light source with high spectral overlap with the absorption of Alq3 (Figure 3.8). For the highest resistance, an open circuit voltage of $V_{oc} \sim 524$ mV was found. Changing the resistance state from the HRS to the LRS via IMRS, the open circuit voltage decreases as well ($V_{oc} \sim 524$ mV → 450 mV → 307 mV → 207 mV → 42 mV → 10 mV), and finally ends up at 4 mV (Figure 3.7a). On the other hand, I_{sc} (current at V = 0 under illumination) remains remarkably constant at 50 nA - independent of the device resistance state and of the decrease of V_{oc}. Also for type **II** devices, photovoltaic measurements reveal the same tendency with respect to V_{oc} and I_{sc} (Figure 3.9).

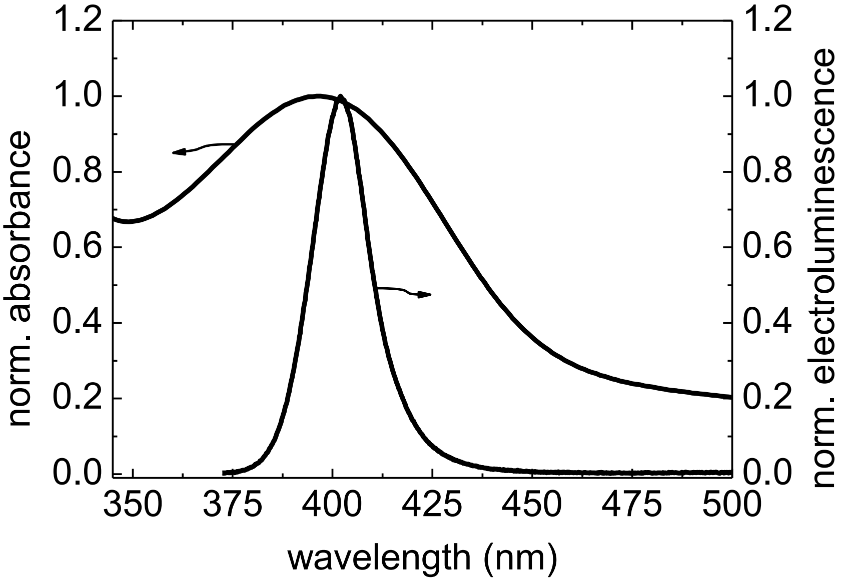

Figure 3.8. Spectral overlap between the normalized absorbance spectrum of Alq3 (black line) and the normalized emission spectrum of the used excitation light source (blue line). Alq3 has a broad absorption spectrum with its maximum at around 397 nm. The excitation LED shows a narrow emission with its maximum at 402 nm/FWHM = 17nm.

Variations in the IV-curve of a photovoltaic cell are explained by leakage currents resulting from a variable shunt resistance.[105] Such shunting pathways typically result in a reduction of V_{oc} while I_{sc} remains constant[106,107], which fits exactly with the observations made for the presented ORS. The studies on shunt pathways in the field of solar cells suggest that these defects are mostly due to the incursion of the electrode material at film non-uniformities and are thus highly localized[108,109], which is very similar to the model of filamentary conduction in organic resistive switching devices.

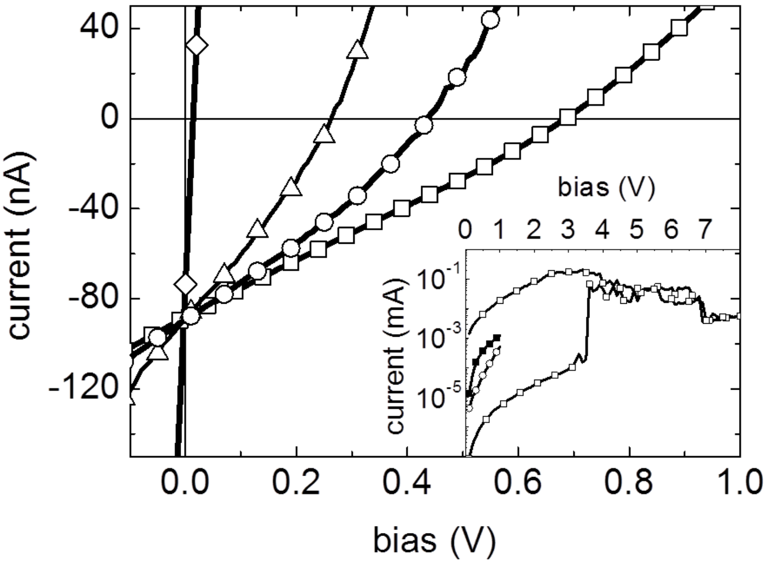

Figure 3.9. I/V-characteristics of four different resistance states from a device of type II under illumination. The obtained open circuit voltage is strongly dependent on the resistance state, whereas the short circuit current is largely constant. The inset shows a typical I/V-characteristics in a half-logarithmic scale with indicated intermediate states.

On the other hand, in the SV-model the variation of V_{oc} can in principle be attributed to modification of the built-in potential due to charge accumulation; still, the constant short circuit current is in strong contradiction to his model: Since any variation of the space-charge density/distribution capable to change the overall device resistance by several orders of magnitude within the device or at the interfaces, would necessarily lead to a variation of the extracted short circuit current due to the modification of the charge transport properties and the injection/extraction barriers.[110]

To test for the validity of the introduced photovoltaic viewpoint, the devices were modelled with the basic equivalent circuit diagram (ECD) of solar cells (Figure 3.7b). By changing from the DC to the AC regime, also possible capacitive contributions (considered by C in the ECD) to resistance switching effect can be revealed. Starting again from the two suggested hypothesis, the expected impact on the building blocks of the ECD was analyzed. In the charging based model, significant changes of the capacitance C are inevitable to explain the switching, whereas C should be largely unaffected in the case of filamentary conduction.

3.4 Impedance Spectroscopy

A method to determine whether the device functionality is dominated by capacitive or ohmic changes is given by impedance spectroscopy, where the overall impedance Z and the phase φ are measured as a function of the applied frequency f. The obtained impedance and phase spectra are largely unaffected by illumination of the device, leading to equal Z-f and φ-f spectra with respect to the individual resistance state (Figure 3.10). This validates the ECD for devices of type **III,** where the previously introduced photovoltaic method is not feasible due to the lack of optical absorbance of the insulating organic layer.

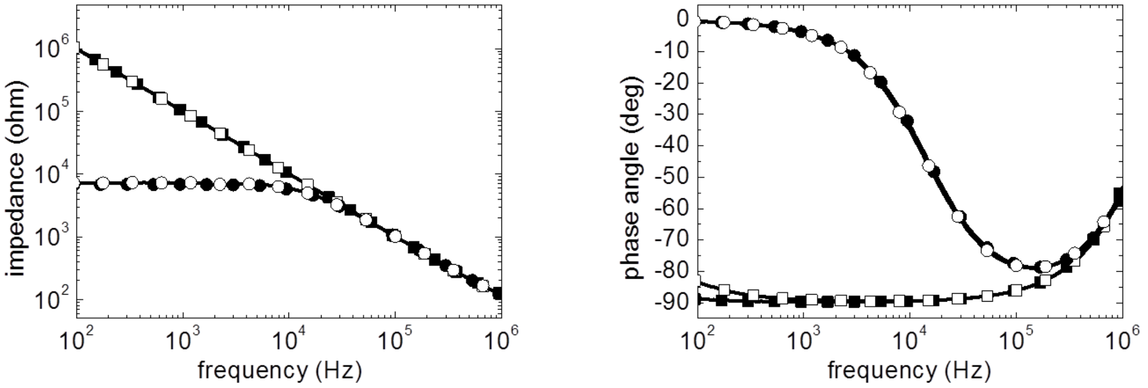

Figure 3.10. Impedance (left) and phase-angle (right) spectra of a type I device in its high resistance state (squares) and the low resistance state (circles). The spectra in dark (closed symbols) were found to be largely equal to the spectra obtained from illuminated samples (open symbols). The small variation in the φ-f spectrum at low frequencies of the HRS is accounted to photoconductivity.

Figure 3.11a – f depict the impedance- (Z-f) and the phase-spectra (φ-f) of the LRS, HRS and one selected IMRS of **I**, **II** and **III** devices, respectively. In order to avoid a change of the device resistance state during the measurement, the semi-amplitude (0.5 V) of the applied signal was kept well below V_T of the devices.

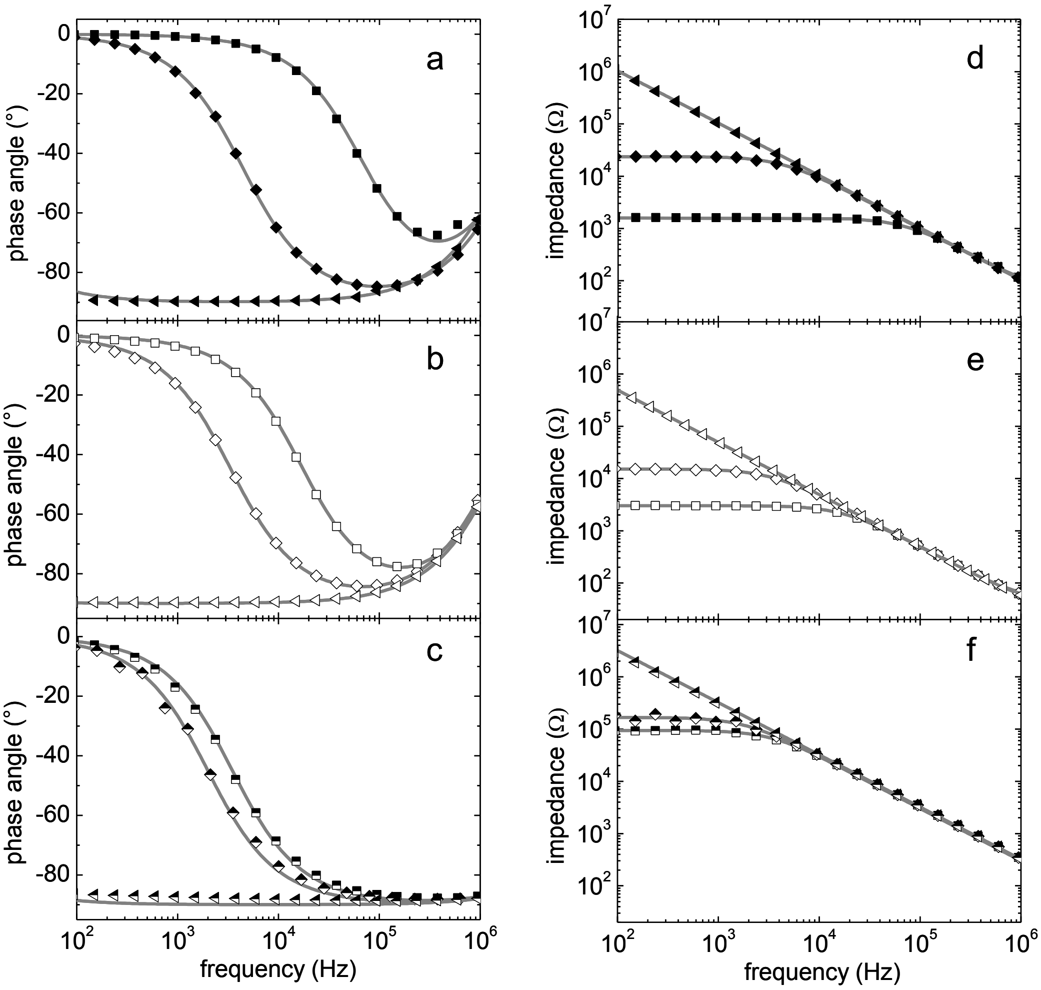

Figure 3.11. Impedance and phase angle spectra from device types I-III for different resistance states: a-c) phase angle d-f) impedance in dependence of the applied frequency from device I (a & d), device II (b & e) and device III (c & f) in different resistance states. Triangles: HRS; Diamonds: IMRS; Squares: LRS. The grey lines represent the fits of the data points according to the equivalent circuit diagram.

Apart from quantitative variations in the individual impedance- and phase-spectra of the three different device configurations, qualitatively the same trend was found: Independent on the device geometry and the organic material a strictly linear dependence of the impedance (Figure 3d, e, f) as a function of the frequency was found for all devices in the HRS. Furthermore, the measured phase angle (Figure 3a, b, c) for the HRS of all three devices remains largely constant at -90°, representing a system mainly dominated by a constant capacitance.

By switching the device from the HRS to an IMRS, the phase angle is shifted close to 0° at low frequencies. Along with this shift, each impedance spectrum shows a nearly frequency independent part which bends downwards at a certain cut off frequency. A further modification of the device state to the LRS extends the frequency independent impedance region as well as the frequency range where the phase angle is close to 0°.

Obviously the impedance characteristic of the HRS represents the limiting curve for all other devices states. Above the cut off frequency of the specific device states, the impedance spectra match with the shape of HRS curve. This overlap shows that the capacitive contribution is constant and can therefore not be responsible for the conductivity of the individual device states. Below the cut off frequency, the phase and the impedance spectra clearly show that the device behavior is dominated by ohmic conduction.

In contrast to device **I** and **II**, the φ-f curve for device **III** does not show this distinctive phase shift to lower angles at high frequencies (f > 10^5 Hz), which is attributed to the reduced contribution of R_s due to the Ag bottom electrode instead of ITO.

Based on the ECD of a solar cell, analytical expressions for the impedance- and the phase response as a function of the frequency, the series resistance R_s, the shunt resistance R_{sh} and the capacity C were derived (Equation 2 and Equation 3).

$$\tan\varphi = \frac{\dfrac{2\cdot\pi\cdot f\cdot C\cdot {R_{SH}}^2}{1+4\cdot\pi^2\cdot f^2\cdot C^2\cdot {R_{SH}}^2}}{R_s+\dfrac{R_{SH}}{1+4\cdot\pi^2\cdot f^2\cdot C^2\cdot {R_{SH}}^2}}$$

Equation 2. Relation for the phase angle in dependence of capacity C, the series resistance R_S and the shunt resistance R_{SH} derived from the equivalent circuit diagram presented in Figure 3.7.

$$Z = R_S + \frac{R_{SH}}{1+4\cdot\pi^2\cdot f^2\cdot C^2\cdot {R_{SH}}^2} + j\cdot\frac{2\cdot\pi\cdot f\cdot C\cdot {R_{SH}}^2}{1+4\cdot\pi^2\cdot f^2\cdot C^2\cdot {R_{SH}}^2}$$

$$|Z| = \sqrt{\Re e(Z)^2 + \Im m(Z)^2}$$

Equation 3. Relation for the impedance in dependence of the capacity C, the series resistance R_S and the shunt resistance R_{SH} derived from the equivalent circuit diagram presented in Figure 3.7.

On the basis of these equations, the spectra were fitted using the Levenberg-Marquardt method. Table 3.1 shows the fitting parameters obtained from the φ-f spectra for each device configuration and state. Additionally, fit results from the Z-f spectra qualitatively and quantitatively confirm these values with high accuracy (Table 3.2): In contrast to the capacitance and the series resistance, which shows no significant dependency on the device state, the corresponding shunt resistance changes by several orders of magnitude.

Table 3.1. Capacitive and resistive parameters from the three different ORS in dependence of different resistance states obtained from fits of the φ-f spectra (Figure 3.11a-c)

	ITO/Alq3/Ag			ITO/Alq3/Al/Alq3/Ag			Ag/PMMA/Ag		
	C [nF]	R_S [Ω]	R_{SH} [Ω]	C [nF]	R_S [Ω]	R_{SH} [Ω]	C [nF]	R_S [Ω]	R_{SH} [Ω]
HRS	1.56	58.2	1.70 * 10^7	3.16	33.8	1.43 * 10^8	0.45	13.6	1.44 * 10^8
IMRS	1.56	49.8	2.30 * 10^4	3.13	36.9	1.51 * 10^4	0.41	15.7	1.96 * 10^5
LRS	1.55	50.5	1.49 * 10^3	3.32	31.8	2.79 * 10^3	0.48	15.0	9.53 * 10^4

Table 3.2. *Capacitive and resistive parameters from the three different ORS in dependence of different resistance states obtained from fits of the Z-f spectra (Figure 3.11d-f)*

	ITO/Alq3/Ag			ITO/Alq3/Al/Alq3/Ag			Ag/PMMA/Ag		
	C [nF]	R_S [Ω]	R_{SH} [Ω]	C [nF]	R_S [Ω]	R_{SH} [Ω]	C [nF]	R_S [Ω]	R_{SH} [Ω]
HRS	1.56	45.1	1.56*10^7	3.23	38.9	1.30*10^8	0.50	12.90	1.56*10^8
IMRS	1.60	52.6	2.36*10^4	3.26	43.2	1.51*10^4	0.52	12.0	1.66*10^5
LRS	1.54	39.4	1.57*10^3	3.17	32.4	2.98*10^3	0.50	5.00	9.41*10^4

3.5 Evidence for Localized Pathways by Optical Microscopy

Previously it was shown that localized spots of high heat dissipation can be found when looking onto the devices top electrode under operation by means of infrared microscopy.[83] Alternative, ORS with a transparent ITO bottom electrode can be operated under an optical microscope. It turns out that most of the devices exhibit a glowing spot, rather randomly found at the device area (Figure 3.12) It is noteworthy that upon switching between HRS and LRS multiple times, the spot mostly (but not always) appeared on the same location. On the one hand this shows that most likely there is only one path which is carrying most of the current in an LRS. This filament can be, but not necessarily has to be, the same one after it was previously dissolved by an erase pulse.

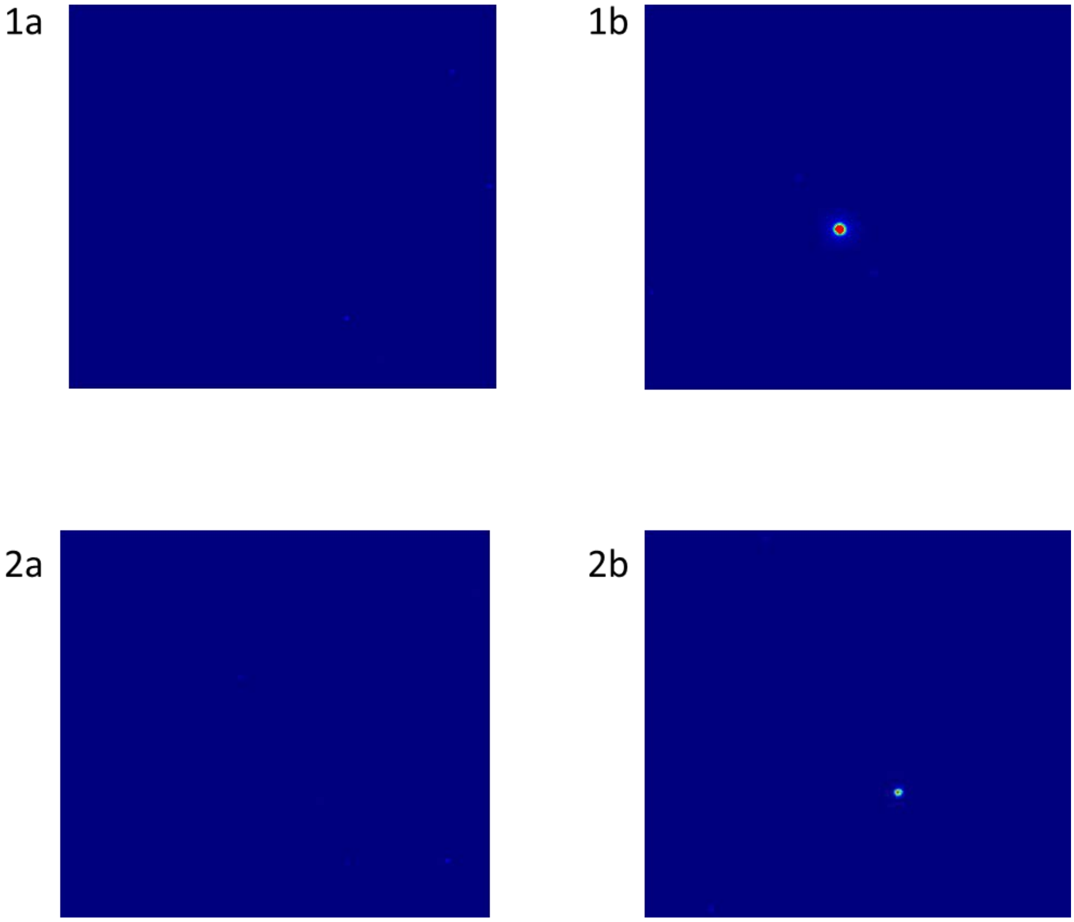

Figure 3.12. Observation of glowing spots by means of optical microscopy for two different devices (false color image). 1a & 2a: HRS. 2a & 2b: LRS

3.6 Experimental Section

Device fabrication

Each device described in this chapter was fabricated on ITO covered quartz or quartz glass solely. The substrates were cleaned with acetone, 2-propanol and toluene in an ultrasonic bath and subsequently dried. Alq3 was purchased from Sigma-Aldrich and used without further purification. The material was thermally evaporated in a vacuum coating unit at a base pressure lower than $1*10^{-6}$ mbar. The silver electrodes were deposited immediately afterwards without breaking the vacuum. For PMMA based devices, silver electrodes were thermally evaporated onto quartz glass. Afterwards, solutions of PMMA were applied by spin-coating and subsequently dried on a hotplate for 10 minutes at 130 °C. In a final step, Ag top electrodes were again thermally evaporated. The size of all devices was 10 mm^2.

Characterization

The basic IV-characterization was performed after contacting the device with tungsten tips using an Agilent B1500A Parameter Analyzer. Impedance and phase spectra were recorded with an Agilent E4980A LCR-Meter. For the IV-measurements of samples under illumination, an inorganic 400 nm LED was used as a light source. All fabrication and characterization steps were performed in an argon filled glovebox (residual gas: < 1 ppm O_2 and < 1 ppm H_2O).

Optical microscopy was performed with an Olympus BX-51 microscope. During measurement, the devices were operated in an sealed measurement chamber.

3.7 Summary

Photovoltaic measurement based analysis of ORS combined with impedance spectroscopy provide a solid proof that the picture of the equivalent circuit of a solar cell is valid and memory functionality can be assigned to a variable shunt resistance (e.g. due to the growth and rupture of a conductive filament). The charging based model can be clearly ruled out to play a major role due to the constant short circuit current of devices under illumination as well as due to the constant capacitive contribution in the AC-spectra, independent of the individual resistance state. Moreover, all presented devices show qualitatively similar IV-characteristics independent of their specific architecture and the used organic- and electrode materials, except from the absolute device currents. The strong variation in the HRS currents can be explained by the different bulk conductivity of the organic materials as well as by the different architectures. As expected, PMMA based devices have the lowest HRS-current. Even though smaller, a variation can also be observed for the LRS current attributed to the stochastic nature of the filament formation process.[41] A strong difference was found during the forming of bi-stability. While single layered device need an extended conditioning procedure, devices with additional metal particles incorporated in the organic matrix quickly show bi-stability, indicating that the metallic particles promote the growth of a filament.

4 Inkjet-printed Resistive Switching Memory based on Organic Dielectric Materials: From Single Elements to Array Technology

This chapter reports on the fabrication of organic resistive switches (ORS) by inkjet printing and their integration into fully functional hybrid crossbar array structures. A route towards the first all inkjet-printed ORS is shown as all preparation steps of the functional components (top and bottom electrode and organic layer) are replaced (step-by-step) from classical fabrication to inkjet-printing. Inexpensive and air stable PMMA was used as organic layer for all devices. For each device configuration a distinct impact to the IV – characteristics is found and analyzed. The requirements for a rectifying diode as selector element in an array application are predicted by an analytical estimation. Within this context, a high-performance pentacene-based 2-terminal organic diode fulfilling the discussed needs is presented. Finally, the proper cross-talk handling in the resulting 1 Resistor - 1 Diode (1R-1D) structure is demonstrated by writing the several patterns into an array.

This chapter is part of a publication in preparation.

4.1 Introduction

Besides the nowadays well known preferable properties, the use of organic materials also paves the way towards environment friendly ‘green’ fabrication routes. Various innovative printing techniques are capable of contributing to this ambitious goal with benefits like reduced material waste due to additive maskless patterning and low-temperature processing.[34] To date, several organic devices have been successfully inkjet-printed including field-effect transistors[111,112], photodetectors[48], infrared detectors[113], light emitting electrochemical cells[114], light emitting diodes[115], photovoltaic devices[116] as well as ferroelectric memories[117]. Still, the printing process is challenging mostly due to the complex interplay between a large number of involved parameters like ink viscosity, surface tension of substrate and ink or drying kinetics. From a fabricational point of view a number of additional issues have to be considered like organic layer ↔ solvent interaction during printing of multilayer structures and the elevated curing temperatures needed for most nanoparticle based metal inks. From this it is evident that also the processing has a large influence on the device performance. Here, the fabrication of the first all inkjet-printed organic resistive switch is reported.

4.2 Towards the first all inkjet-printed organic resistive switch

Figure 4.1a displays the unipolar N-shaped IV-characteristics of an Ag/PMMA/Ag ORS, fabricated by means of classical techniques i.e. thermal evaporation of the metal contacts and spin coating of the PMMA layer.

In a first step, the evaporated bottom electrode was replaced by an Ag-electrode printed from a nanoparticle based silver ink followed by a thermal sintering step to establish its conductive properties. The subsequent layers were spin-coated and evaporated, respectively. Compared to the reference devices, the IV-curve (Figure 4.1b) shows a clear deviation of I_{OFF}, which is assigned to the increased number of parasitic defect pathways in the HRS state caused by the higher surface roughness of the inkjet-printed bottom electrode. Consequently the I_{ON}/I_{OFF} -ratio is reduced to $\mathbf{6.5 \cdot 10^4}$.

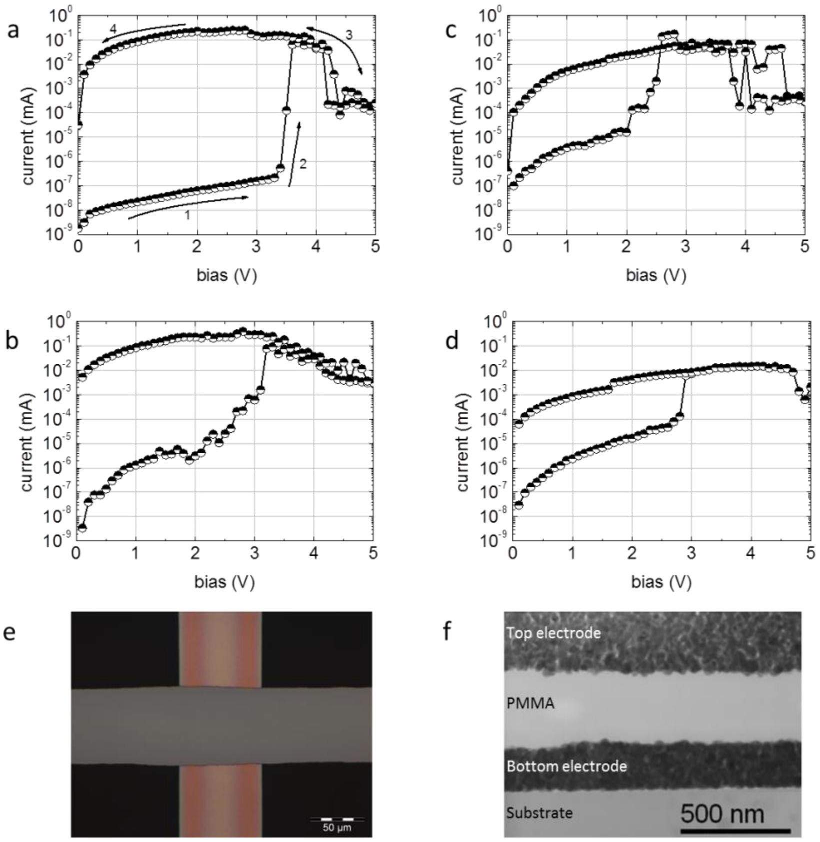

Figure 4.1. IV-characteristics of organic resistive switching devices with different inkjet-printed components. For all devices the organic layer was spin coated with the same parameters. a) IV-curve of a standard fabrication device. The bottom and the top electrode were evaporated, leading to an I_{ON}/I_{OFF} *ratio of* $3 \cdot 10^6$ *(at 1 V). b) Only the bottom electrode is inkjet-printed -* I_{ON}/I_{OFF}*:* $6.5 \cdot 10^4$ *(at 1 V). c) Only the top electrode was inkjet-printed -* I_{ON}/I_{OFF}*:* $2 \cdot 10^3$ *(at 1 V). d) Bottom and top electrode inkjet-printed -* I_{ON}/I_{OFF}*:* $2.8 \cdot 10^2$ *(at 1 V). e) inkjet-printed memory element: both electrode line width are in the range of 70 µm; f) high-resolution TEM cross-section through a memory with both electrodes inkjet-printed.*

The third device (Figure 4.1c) had a reversed built-up, i.e. an evaporated bottom electrode and a printed top electrode. An oxygen plasma treatment of PMMA layer was necessary to adjust the wettability of the ink. Here, a further decrease in the ON/OFF ratio was found (**$2 \cdot 10^3$**), which is ascribed to the solvent load during the printing of Ag-ink onto the PMMA layer accompanied by a partial dissolution of the organic layer and interdiffusion of metallic particles. Further it is suggested that the postprocessing of the silver electrodes leads to increased defect formation in the film due to interdiffusion of the metal.[118] The fourth device combines the printing of the top and the bottom electrode, consequently also combining both I_{ON}/I_{OFF} ratio reducing effects and resulting in the lowest value of **2.8 · 10²** (Figure 4.1d). A micrograph of such a device can be found in Figure 4.1e. A high resolution TEM cross section from the device with both electrodes printed is displayed in Figure 4.1f, clearly showing the granular morphology of the sintered Ag – ink. It is evident that the poor I_{ON}/I_{OFF} ratio is mostly governed by localized defects in the organic film. A significant increase of the layer thickness can therefore also increase the I_{ON}/I_{OFF} ratio by decreasing the OFF-current. Therefore, in order to achieve a satisfactory ratio from the final all inkjet-printed device, a rather high PMMA layer thickness of about 500 nm was chosen and printed using a single nozzle print head. The whole fabrication process was carried out at ambient atmosphere. The resulting IV-characteristics is shown in Figure 4.3a. Indeed this device led to a decrease of I_{OFF} and increase of the I_{ON}/I_{OFF} ratio to ~ $3.5 \cdot 10^4$. Figure 4.2 shows endurance of an all inkjet-printed ORS in a cycling test. The yield for these devices, however, was significantly lower compared to devices with spin coated organic layer. Due to the low failure tolerance in array applications this is considered to be not sufficient. Therefore, for the devices presented in the following, the organic layer was spin coated, while the electrodes were printed. Since a structured application of PMMA is not strictly advantageous (no impact on the memory array performance and no cost related issue w.r.t to PMMA), this approach can be seen as more practical.

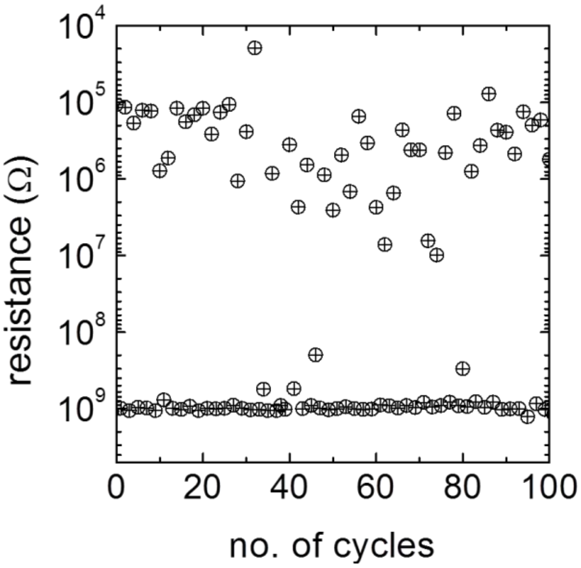

Figure 4.2. Endurance test of a typical device obtained by writing (3 V), reading (1 V), erasing (6 V) and reading again the memory state. The resistance states at the reading bias are displayed as a function of the cycle number. Although variations of the absolute current levels of the LRS state are observed, a clear discrimination between HRS and LRS is mostly possible.

4.3 Array Integration

According to the requirements described in chapter 2.2 a thermally evaporated organic rectifying diode was developed as access device in the array. Figure 4.3b depicts the IV - curve of an thermally evaporated Au/MoO_3/Pentacene/Ca/Al device stack: In forward direction (Au-electrode positively biased, Al-electrode negatively biased), the device has a steep onset at about 0.5 V and a high forward current of ~2 µA (at read-out bias); Under reverse bias a good blocking behavior can be found and a low current of ~14 pA (at -2 V) was measured. On the basis of Equation 1, a maximum array size of 34 by 34 elements with a fixed minimum R of 100 can thus be estimated.

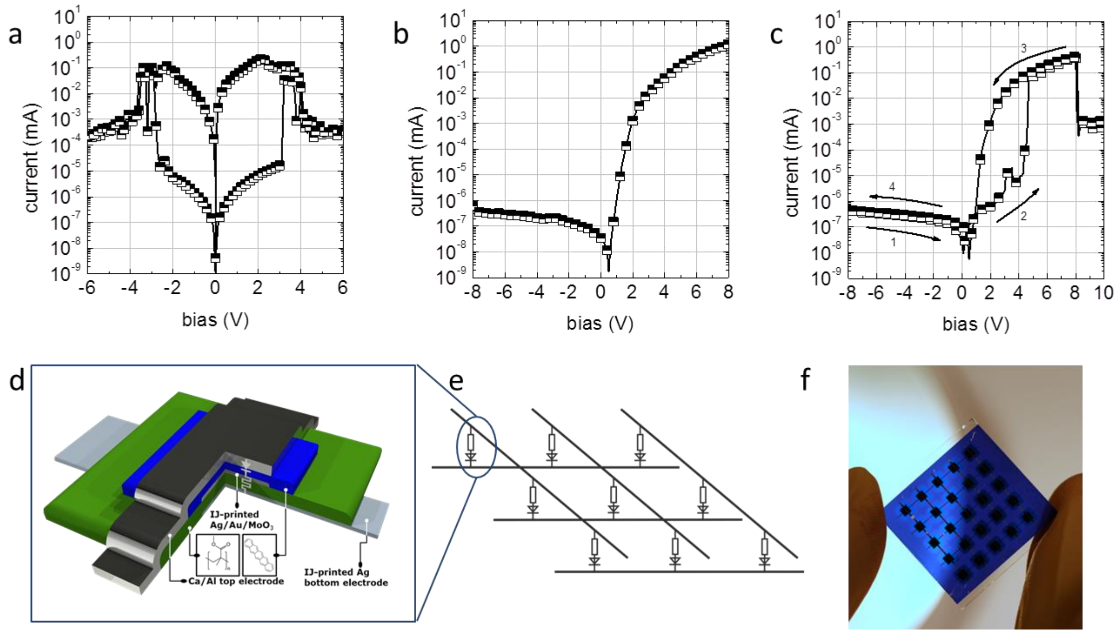

Figure 4.3. IV-characteristics of an ORS, the OD and the 1R-1D stack. a) IV-curve of the all inkjet-printed Ag/PMMA/Ag ORS. A nearly symmetric behavior is observed in the characteristics: threshold voltage ~ ± 3 V; read-out region |U| < 2 V; NDR 3 V – 6 V. b) IV curve of an Au/MoO_3/Pentacene/Ca/Al diode with an onset voltage of 0.5 V. Current is effectively blocked under reverse bias (< 50 pA up to -8 V) leading to an rectification ratio of > 10^6 (at 5 V). c) IV-curve of a stack of an ORS with an OD on top: Ag/PMMA/Ag/Au/MoO_3/Pentacene/Ca/Al: In forward direction, the OD, does not act as a current bottleneck for the ORS, whereas under reverse bias conditions, the IV-curve is dominated by the reverse current of the OD solely, irrespective of the resistive state of the ORS. The measurement sequence is indicated by the arrows. d) Illustration of a 1 resistor – 1 diode single memory cell; e) wiring of individual 1 resistor – 1 diode elements in a passive crossbar array structure; f) photograph of a fully functional hybrid memory array with inkjet-printed memory elements and pentancene based high performance diodes.

Such a diode structure was directly applied on top of each memory cell of a 5 by 5 array (Figure 4.3d) and connected with the top Al-line, leading to an Ag/PMMA/Ag/Au/MoO_3/Pentacene/Ca/Al multilayer configuration. The IV-characteristics of this vertical 1 resistor – 1 diode stack is depicted in Figure 4.3c, showing a close to ideal behavior: Initially, the device is in its HRS and the IV – sweep was started at -8 V. In the reverse polarization, only the reverse current of the diode is measured. In forward direction (0 V – > 8 V – > 0 V), the highly conductive pentacene diode does not limit the ORS, therefore leading to a threshold event and a typically shaped IV-curve of an ORS is found. The ORS is now in its LRS, however when going back to -8 V, the diode acts as a current limiter and again only the low reverse current of the diode is present in the IV – curve.

To test for a proper cross-talk handling, several scenarios were programmed into a 2 by 2 sub array. Figure 4.4 displays the current levels obtained for an information pattern where no, one, two and three (worst case) devices in the 2 by 2 array are in their LRS. As it is evident from the figure, cross-talk is effectively suppressed by the rectifying diode and the read-out of device 4 in its HRS isn't significantly influenced. Note that all other nodes in the 5 by 5 array contribute to the detected sneak current, although they are in their HRS.

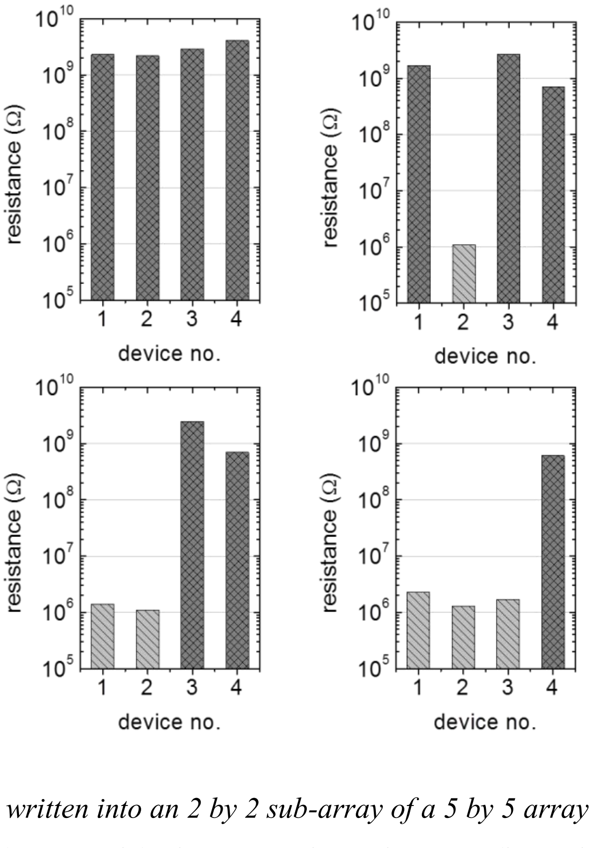

Figure 4.4. Test patterns written into an 2 by 2 sub-array of a 5 by 5 array: all devices HRS (upper left); device 2 in its LRS (upper right); device 1 and 2 in their LRS (lower left) and device 1, 2 and 3 in their LRS (lower right). This last pattern renders the 'worst-case' scenario for such an array, however, the resistive state (HRS) of device 4 can still be clearly distinguished from an LRS.

4.4 Experimental Section

Device fabrication

Printing of the Ag-electrodes was performed using a PixDro LP50 printer equipped with a FujiFilm Dimatix (Spectra) S-Class 128 nozzle piezoelectric printhead. Cabot CCI-300 Ag nanoparticle based ink formulation was used as ink. After printing the bottom electrode, the samples were cured at 200°C for 30 min. Before printing the top electrode, the substrate was exposed to oxygen plasma to achieve proper wetting of the ink on the PMMA layer. In order to reduce metal diffusion into the organics caused by the elevated curing temperatures, different curing parameters (150°C, 2h) were chosen. Both curing procedures led to conductive behavior of the Ag contacts. The typically electrode height obtained was in the range of 200-400 nm (typical height profile displayed in Figure 4.5). The organic material was printed with a single nozzle printhead (MicroFab Technologies Inc. MJ-AT-01-50; Orifice diameter: 50 μm) mounted on a PixDro LP50 printer leading to a thickness of ~ 500 nm. For the reference devices, Ag-electrodes were thermally evaporated in a vacuum coating unit at a base pressure lower than $1 \cdot 10^{-6}$ mbar. PMMA was applied by spin-coating and subsequently dried on a hotplate for 10 minutes at 130 °C.

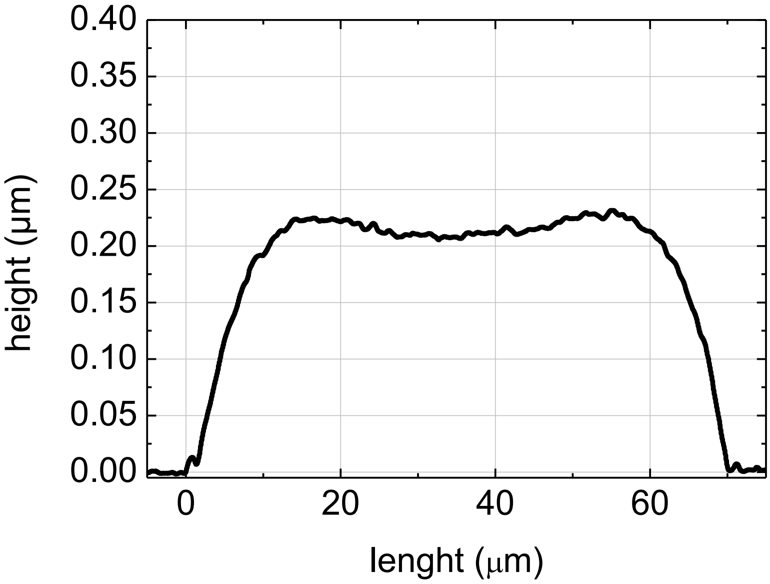

Figure 4.5. Typical height profile of a silver electrode line.

Characterization

The IV-characterization was performed after contacting the device with tungsten tips using an Agilent B1500A Parameter Analyzer. The characterization was performed in an argon filled glovebox (residual gas: < 1 ppm O_2 and < 1 ppm H_2O) if not stated otherwise.

4.5 Summary

To summarize, the first all inkjet-printed resistive memory elements and their integration into crossbar array structures with high-performance organic rectifiers as selector elements has been demonstrated. The distinct impact of printing individual building blocks was shown and analyzed, which finally led to an optimized all inkjet-printed PMMA-based resistive memory element, completely fabricated under ambient conditions. The integration of printed ORS in a 5 by 5 array was achieved with a hybrid approach by stacking a pentacene-based high performance diode (rectification ratio: ~ 10^6 at 5 V) on top of each ORS. Further, an analytical expression to estimate the requirements for a diode for a given array size was deduced. The proper cross-talk handling was demonstrating on the basis of a series of information patterns written into a 2 by 2 sub array. Future work on the topic of printing memory arrays will have to focus on increasing of the yield of all inkjet-printed devices as well as the development and processing of solution processable low workfunktion materials for inkjet-printed organic Schottky diodes.

5 Organic Non-Volatile Resistive Photo-Switches for Flexible Image Detector Arrays

In this chapter, a unique imaging device concept and its utilization in an organic, flexible detector array with a simple passive matrix wiring is introduced. The application of photo-switchable non-volatile resistive multi-bit 2-terminal devices as pixels is demonstrated. This approach is based on a vertical stack consisting of an OPD, acting as photosensitive element and an organic non-volatile multi-bit resistive switch (ORS), acting as image information storage element. Both devices exhibit a variable resistance, i.e. the OPD changes its resistance dynamically upon illumination and the ORS changes its resistance in dependence of the applied bias and retains this resistance state permanently even after bias is removed. The combination of these device intrinsic features in a serial connection of both elements is used to simultaneously convert the light induced dynamic resistance change induced at the OPD to a non-volatile resistance change at the ORS. In addition to a basic on/off operation mechanism, a grey-scaling capability based on the multi-bit capability of the ORS is demonstrated up to 4-bit. Moreover in the serial connected device stack the OPD not only acts as the light-sensitive element but given its high rectifying behavior (>10^5) also renders a selector element allowing for passive matrix addressing in the array. The proper functionality of this concept is demonstrated in single elements and array structures up to 32 by 32 cells (1024 bit), integrated into an organic and flexible passive-matrix image detector array.

Parts of this chapter are submitted for publication:
S. Nau, C. Wolf, S. Sax, E. J. W. List-Kratochvil, 'Organic Non-Volatile Resistive Photo-Switches for Flexible Image Detector Arrays'
The author of this thesis planned and performed all experiments, the data analysis and wrote the manuscript.
C. Wolf assisted during the experiments, S. S. and E. J. W. L.-K. supervised the work.

Parts of this chapter are filed for a Patent:
S. Nau, S. Sax, Emil J. W. List, 'Speicher-Sensoranordnung mit einem Sensorelement und einem Speicher, Österreichische Patentanmeldung A50442/2013.

5.1 Introduction

To date, charge-coupled devices (CCD) and complementary metal-oxide-semiconductor (CMOS) active pixel sensors represent the two major flat-panel image detector technologies. Although both implementations are at a very mature technological level, each detector technology suffers from particular limitations either due to the utilized Si-technology (rigidity, weight, restrictions in chip size and strong scaling of production costs with the detector area) or due to device inherent limitations such as read out speed, destructive read-out or noise. Due to these restrictions there is a growing industrial demand for cheap and easy-to-fabricate, lightweight, large-area and flexible detector array systems. It is expected that organic electronics based technologies are able to fill this gap. Over the past years first organic devices such as optical data links[119], x-ray detectors[120,121], high-resolution image detectors[122], color[123] and infrared[124] image detectors, sensor systems[125], or even retinal prosthesis[126–128] were demonstrated. Potential future applications fields for these devices will be machine vision systems, x-ray based material inspection and medical imaging applications like computed tomography, radiography or angiography.

Organic photodiodes (OPDs) are devices which change their resistance upon illumination due to photo-generated charge carriers (photoconductivity). While the performance of single OPDs can be considered as sufficiently well developed for most demands, the integration in complex, pixelated detector arrays is significantly less progressed: In the simplest scenario, OPDs are placed at the cross points of perpendicular oriented electrode lines.[128] Though this passive matrix wiring is simple, significant dark currents due to cross talk from adjacent non-addressed elements - scaling with the number of illuminated cells - has to be expected during read-out. To overcome this issue an additional selector element (transistor) is usually included in conjunction with the OPD in each pixel (active matrix design – similar to CMOS detectors).[129] In sophisticated systems, such as the active pixel sensor design, three (or more) transistors are used per pixel for detection, selection and signal amplification in one building block.[130] This more complex circuitry certainly increases fabrication related demands and thus increases costs while it limits the possible integration density due to the larger footprint of a single pixel. Although most of the to date presented organic image detector systems utilize π-conjugated materials as photo-active component in the OPDs, the selector devices are still fabricated using conventional inorganic electronic devices to obtain the full dynamic range of the OPD.[27]

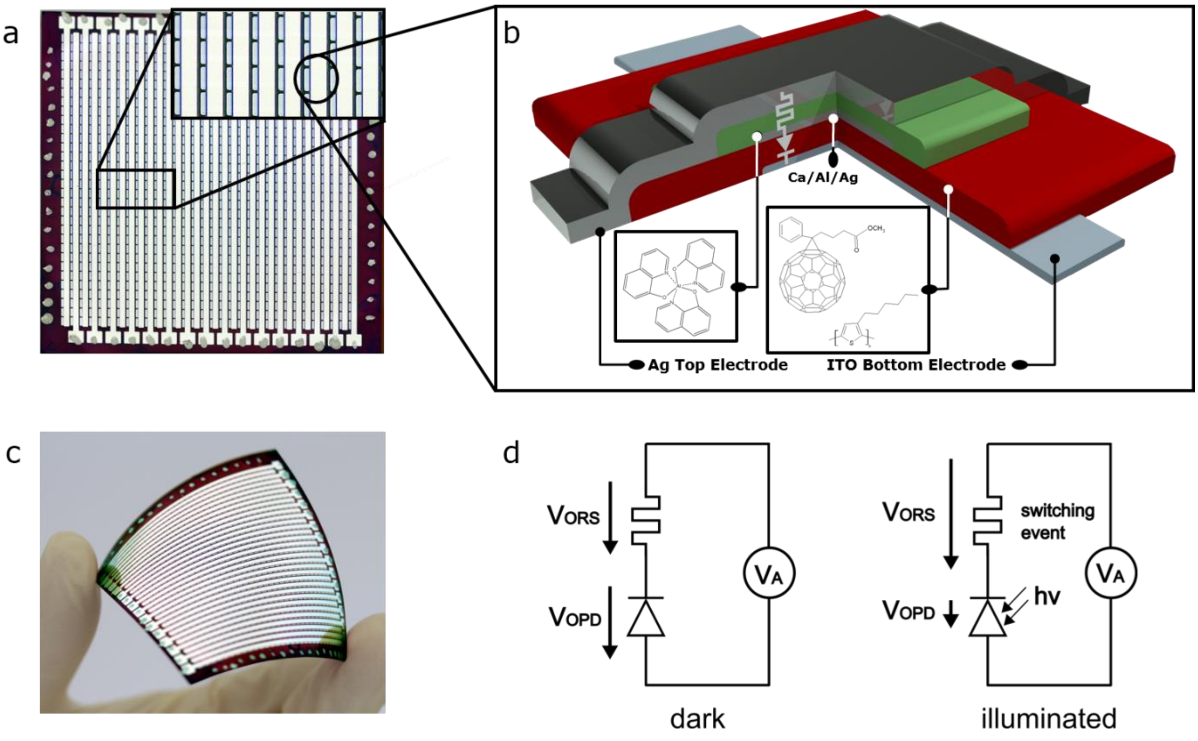

Figure 5.1. Photographs and illustration of the assembly and the image detection principle. a) Micrographs of the 32 by 32 pixel detector array. The ITO bottom electrodes (perpendicular oriented to the Ag top electrode lines) are not visible due to the opacity of the photoactive layer (dark red). b) Schematic cross-section through a single pixel and the materials used. c) Photograph of the image detector array on a flexible substrate. d) Detection principle of a single pixel: illumination of the OPD leads to a redistribution of the voltage drops across the two devices. This is used to trigger a threshold event which leads to a non-volatile resistance change in the ORS.

5.2 Individual Building Blocks

As illustrated in Figure 5.1, a single pixel of the presented image detector concept comprises a vertical stack of an OPD and an ORS. As OPD, a well-known system based on a photo-active layer consisting of a blend of regio-regular poly(3-hexylthiophen-2,5-diyl) (rr-P3HT) and phenyl-C61-butyric acid methyl ester (PCBM), forming an p-n bulk-heterojunction in-between the two electrodes, was used.[27,131] To calculate the responsitivity (sensitivity) of the fabricated photodiode the photocurrent was measured in dependence of the irradiance (in mW cm^{-2}) at a bias of -3 V. Figure 5.2 shows the results obtained from a inorganic green LED ($\lambda_{max} = 525$ nm; FWHM = 17 nm) as light source with a high spectral overlap with the absorption of rr-P3HT:PCBM. The obtained relation is close to linear for more than four orders of magnitude of irradiance. From this dataset the responsivity can be calculated according to equation.

$$R = \frac{I_{ph} - I_{dark}}{P_{opt}}$$

Equation 4. Responsivity in dependence of the measured current under illumination (I_{ph}), the dark current (I_{dark}) and the incident light power (P_{opt})

A responsivity of 200 mA W^{-1} was obtained, largely constant over the given irradiance region. A dark current density of < 50 nA cm^{-2} at -3 V was found. Compared to other rr-P3HT:PCBM OPDs, both values can be considered as typical.[27] The data discussed here was measured directly in the OPD-ORS stack by connecting the anode and the intermediate metal electrode, acting as cathode. A typical IV-curve of the OPD at different illumination conditions is shown in Figure 5.3a

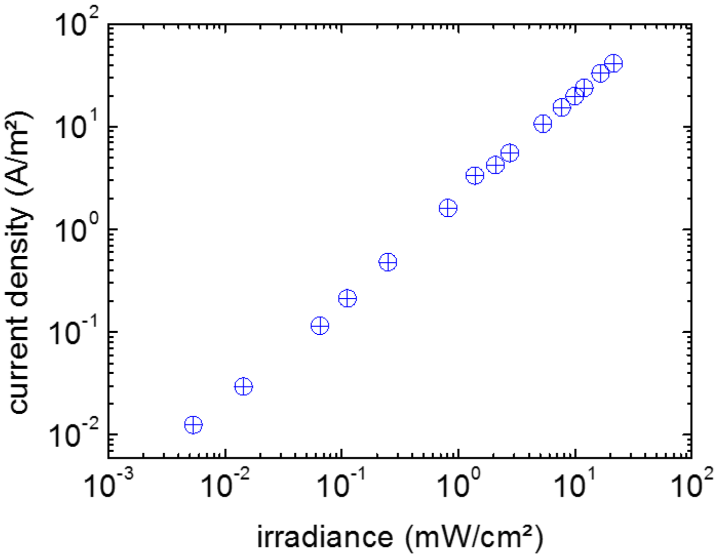

Figure 5.2. Photocurrent at -3 V in dependence of the irradiance. A linear dependency is found for more than 4 orders of magnitude.

ORS represent, compared to other organic electronic devices, a relatively new field of research. While their inorganic counterparts are about to revolutionize the memory market, large progress is also made for organic devices. ORS are typically assembled in a 2-terminal electrode/organic/electrode sandwich architecture. This makes a high density, $4F^2$-footprint crossbar array implementation possible - a superior feature compared to other emerging memory technologies. The IV-curve of an Ag/Alq3/Ag device, a typical ORS, is shown in Figure 5.3b.

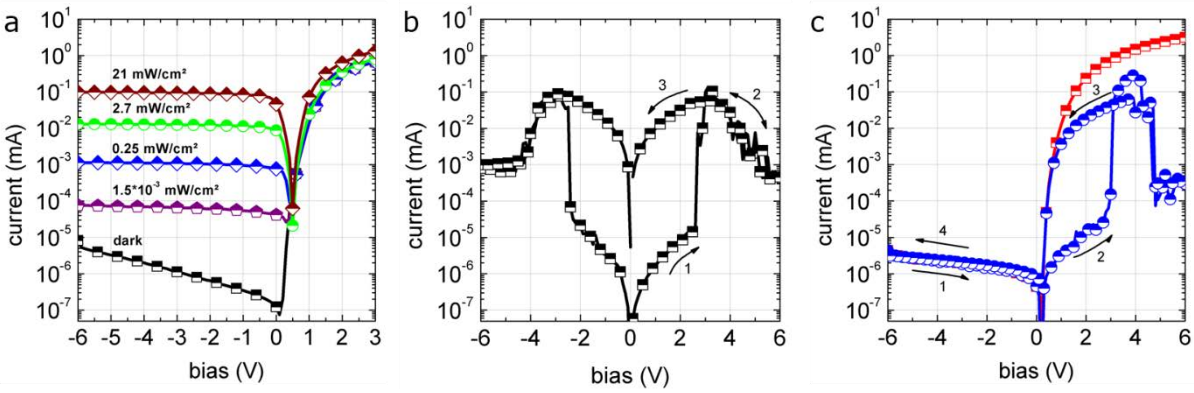

Figure 5.3. IV characteristics of the OPD, the ORS and a stack consisting of both devices. a) IV curve of the OPD under dark conditions (black line) and different illumination conditions. b) typical IV-curve of an Alq3 based ORS device. Device relevant figures of merit can be deduced from this curve: read-out region < 2 V, threshold voltage ~ 3 V, negative differential resistance 3 V - 5 V, delete voltage > 5 V. The measurement sequence is indicated by the arrows. c) IV- curve of a stack of an ORS on top of an OPD (blue) and IV-curve of the OPD solely under dark conditions (red). Under reverse bias conditions, the IV-curve is dominated by the reverse current of the OPD. In forward direction, the OPD does not limit the distinct characteristics of the ORS. The measurement sequence is indicated by the arrows.

5.3 Single Detector Pixel

A stack of an OPD and an ORS represents a serial connection. When applying a voltage across the this stack, the setup can be considered as a voltage divider: According to Kirchhoff's laws, a fixed applied voltage ($V_{APPLIED}$), splits up into a voltage drop across the OPD (V_{OPD}) and across the ORS (V_{ORS}), depending on the resistance of the two individual building blocks ($V_{APPLIED} = V_{OPD} + V_{ORS} = R_{OPD} \cdot I + R_{ORS} \cdot I$). V_{OPD} decreases as the resistivity of the OPD decreases upon increasing irradiance, resulting in a corresponding increase of V_{ORS}. As illustrated by Figure 5.1d, this principle is used to trigger the threshold event in the ORS: As soon as V_{ORS} exceeds V_T, the resistive switching element changes its resistance state. This resistance state is preserved, even if illumination and the voltage is turned off and can be read-out at any time later. Thus the image information is stored in each pixel until a reset pulse (+ 7 V) is applied. Compared to CCD detectors, which exhibit a destructive read-out, unlimited access to the image information is possible.

Based on this principle of operation, a vertical stack consisting of an Alq3 - ORS on top of an rr-P3HT:PCBM - OPD, resulting in an ITO/rr-P3HT:PCBM/Ca/Al/Ag/Alq3/Ag assembly, was realized. The IV-curve of the vertically stacked combination of both devices is shown in Figure Figure 5.3c and can be described as follows: Initially the ORS is in its HRS. The IV – sweep was started at -6 V and bias was decreased to 0 V, detecting only the reverse current of the diode. In forward direction (0 V – > 6 V – > 0 V), the photodiode is conductive and does not act as current-bottleneck for the ORS. The typical shaped IV-characteristics of a single ORS can be observed. When going back to -6 V again, the low reverse current of the diode dominates, although the ORS element was switched to its LRS.

ORS typically have an on/off ratio (LRS to HRS ratio) up to 10^7 and a high amount of intermediate resistance state in-between these two extremes can be addressed. This gives the system a distinct grey scaling capability. An intermediate state can be written by applying a voltage pulse in the NDR region. The same effect can be obtained by adjusting a suitable current compliance value during the switching event which programmes this resistance into the memory element (see also Figure 2.4). Photoconductivity of the OPD at certain illumination conditions renders an 'intrinsic' and analogue current compliance for the ORS in the OPD-ORS stack allowing to store various greyscale values.

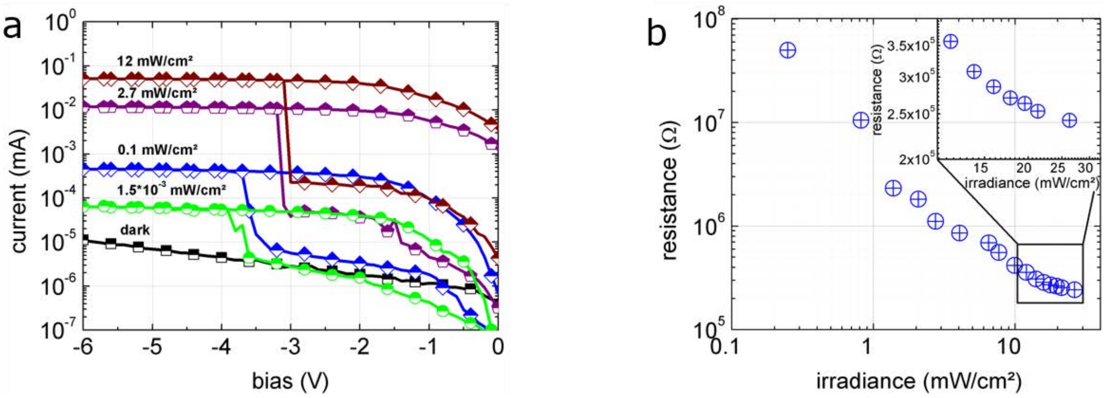

Figure 5.4. Grey scaling mechanism and capability of a single pixel of the memory array. a) IV-curve (reverse bias) of the OPD-ORS stack for various illumination conditions. In dark, the IV-curve is dominated by the low reverse current of the OPD and no threshold event can be observed (black curve). Under illumination, a threshold can be observed and the generated photocurrent in the OPD determines the resulting resistance of the ORS. b) By means of this principle, 16 different resistance states (4-bit) were written.

Figure 5.4a shows the IV-curve at reverse bias of the OPD-ORS stack under different illumination conditions. A voltage applied to the detector element leads to voltage drops across OPD and ORS depending on their specific resistance. Under reverse bias, the resistance of the OPD (dark) typically exceeds the resistance of the ORS in its HRS by a factor of more than 10 and therefore most of $V_{APPLIED}$ drops across the OPD. The remaining small voltage drop across the ORS is not sufficient to trigger a threshold event (Figure Figure 5.4, black line). Under illumination, the photoconductivity of the OPD leads to a modification of its resistance resulting in a redistribution of V_{ORS} and V_{OPD}. If $V_{ORS} > V_T$, the ORS changes its resistance state determined by the photocurrent supplied by the OPD. Figure 3a demonstrates this principle for four different irradiance values where four corresponding resistance states between 60 MΩ and 100 kΩ are programmed into the ORS. So far, 4-bit grey scaling was realized in this way (Figure 5.4b).

Note that a small additional photocurrent is generated in the Alq3-based ORS. It has been shown, however, that illumination does not influence the switching behavior[132] and an additional darkening of this element is not necessary.

One detection cycle of a single pixel can be summarized as follows: 1) the stack is set to a bias of -5 V (well above V_T). 2) Depending on the light exposure, the ORS element changes its state. 3) The written information can be read by measuring the resistance of the system (at 1.5 V) under dark conditions. 4) The procedure is finished by resetting the system and preparing it for a new exposure (+7 V).

5.4 Integration into detector arrays

Irrespective of the specific application case, a passive 2-terminal crossbar array structure suffers from parasitic sneak current caused by adjacent non-addressed elements, bypassing the addressed one. To avoid this problem, an additional element with a particular non-linearity in its IV characteristics has to be integrated in series to each node. For a passive array of ORS, this element can be a rectifying diode, matching with the absolute current levels of the ORS. As a distinct feature of the presented concept, the rr-P3HT:PCBM photodiode is not only used as a photosensitive element, but also fulfills the desired requirements (high forward current, low reverse current and low onset voltage) under dark conditions (Figure 5.3a). Thus it can also be used as non-linear rectifying device, enabling a proper read-out of the stored image information in the resistive switch. Figure 5.3c clearly indicates that the diode current does not limit the IV-curve of the ORS in forward direction, ensuring that the full on/off ratio of the ORS is available to store image information. Under reverse bias, the low reverse current of the diode dominates the circuitry, guaranteeing a proper blocking of current contributions from neighboring elements.

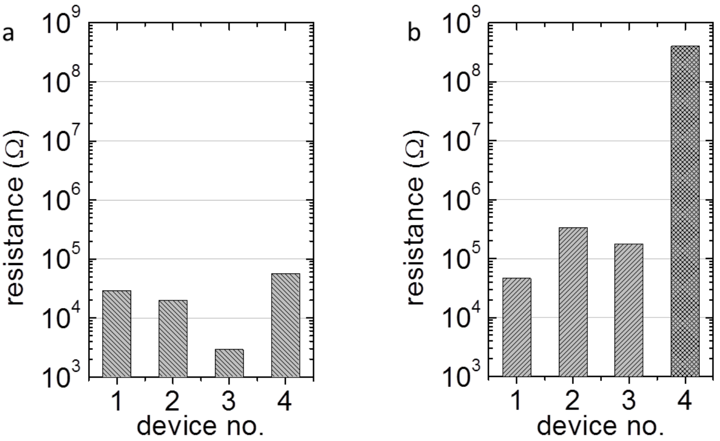

Figure 5.5. Demonstration of the necessity of a rectifying element in arrays of ORS. Devices 1 – 3 are in their LRS, device 4 is in its HRS a) Obtained resistance values of an array of ORS solely – a proper read-out is not possible, due to the bypassing of the addressed element via non-addressed adjacent elements in their LRS. b) Obtained resistance values of an array implementing an ORS and the rectifying (photo) diode in each pixel. A proper read-out is thus possible.

To verify for an appropriate sneak current handling in the detector array, the worst case scenario - being an element in its HRS surrounded by elements in their LRS - was imitated. Figure 5.5a demonstrates this issue for 2 by 2 cells of ORS without and with photodiode in comparison. Figure 4a show the read-out contrast of an array of solely ORS (no OPD): devices 1-3 are in their LRS and device 4 is in its HRS. During read-out of device 4, however, a low resistance is apparently measured from the periphery caused by the low resistance of the three adjacent elements. Thus, no proper read-out is possible. The same pattern was written in a 1 photodiode – 1 resistor array (Figure 5.5b). Here, parasitic current is effectively blocked by the diode and the read-out of device 4 in its HRS is not significantly influenced by the other three elements.

Although a slight increase of sneak current (dark current) was observed during the characterization of the 32 by 32 pixel detector array, it was possible to show the full functionality of the cells. Figure 5.6 shows various IV curves obtained from different cells in the array. Note that the reverse current of the stack increases compared to single elements due to cross-talk in the array, however the full functionality of the cells can be obtained. Due to fact that the thicknesses of both organic layers (rr-P3HT:PCBM and Alq3) are larger than 300 nm, the effect of thin-film defects was limited and the number of short devices was kept at an minimum.

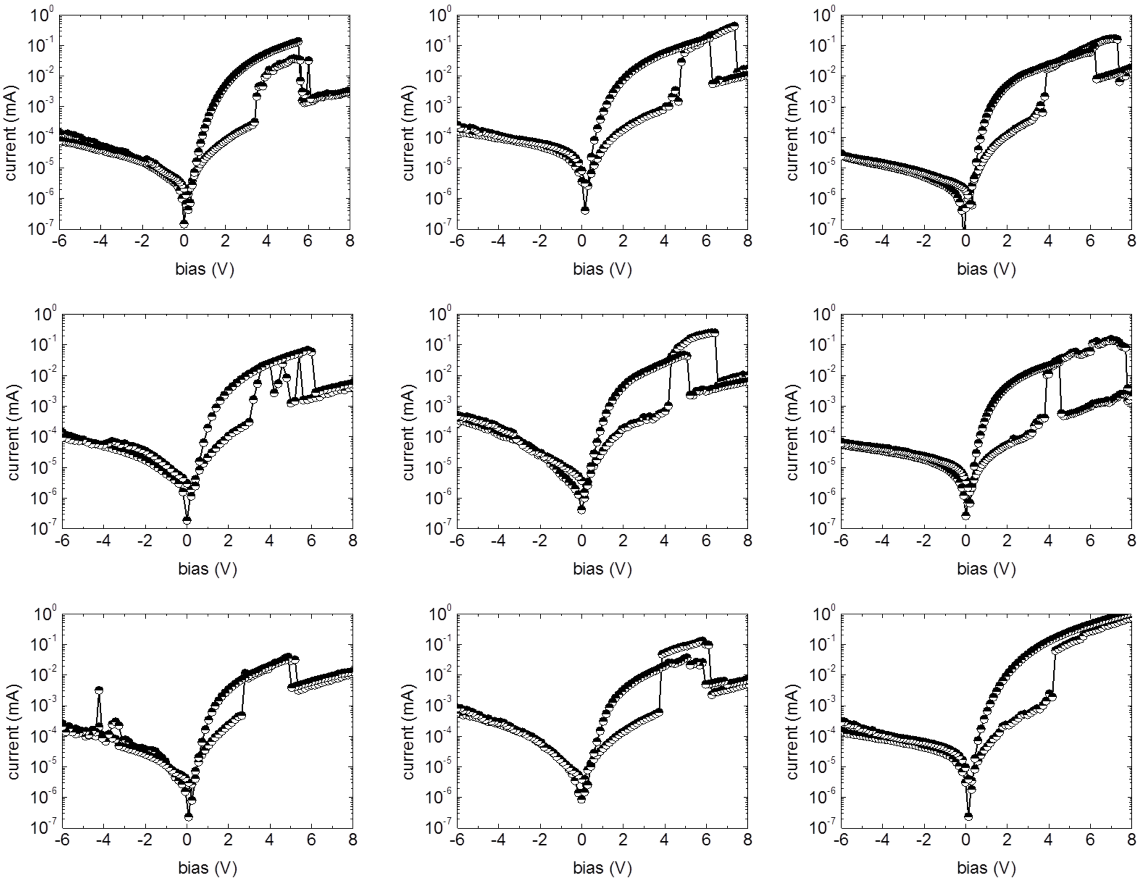

Figure 5.6. Typical IV-curves obtained from different cells in the 32 by 32 array.

A detection cycle in the array is basically equal to that of the single element: 1) all pixels are set to a constant bias of -5 V simultaneously (by connecting all word and bit lines, respectively). 2) only illuminated pixels change their resistance state. 3) the detected pattern is read by sequentially measuring the resistance of each cell (+ 1.5 V). 4) a reset bias of +7 V, again simultaneously applied to each cell, makes the system again ready for the next frame. Figure 5.7 shows four different illumination patterns, sequentially written into 3 by 3 cells by using the described routine. It can clearly be observed that only the illuminated devices change their resistance state by orders of magnitude.

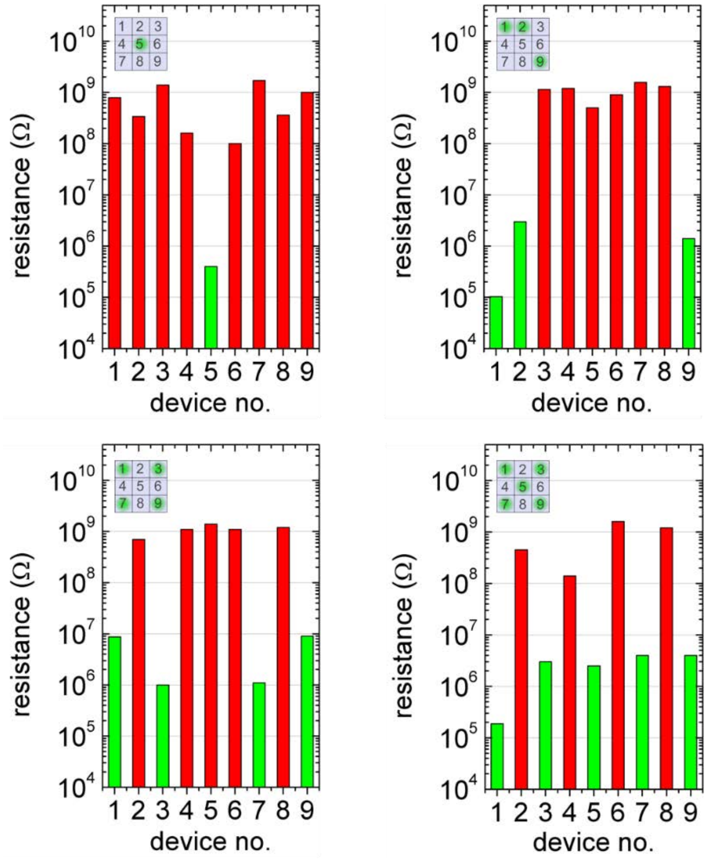

Figure 5.7. Patterns written in a 3 by 3 pixel detector according to the presented detection scheme. A voltage of -5 V was applied to all elements, simultaneously during light exposure. For illumination, green emitting LEDs were directly placed below the selected elements (see inset). The written patterns were properly stored in the detector array.

5.5 Expanding the concept to X-Ray detectors

Most of today's available x-ray detectors (CCD or CMOS based) make use of a scintillator coating that converts x-rays into visible light. Although different studies suggest that an P3HT:PCBM photodiode can in principle be used to directly detect x-ray radiation[120], the induced photocurrent is by far too low for practical applications. Therefore, typically a scintillator material is integrated with the detector element. The here demonstrated detection principle, based on a stack of an non-volatile memory and an organic photodiode together with a scintillator material (Figure 5.8) has many conceptual advantages compared to other presented x-ray detection systems, e.g. the possible simple passive matrix integration and the resulting small footprint.

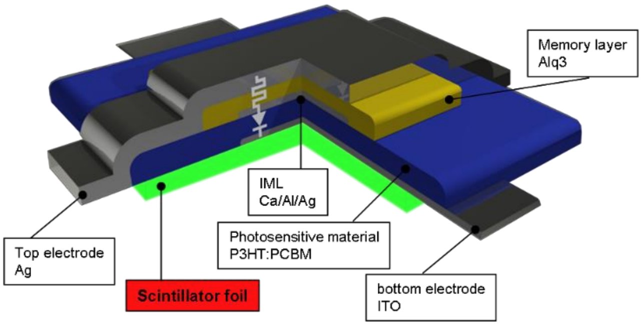

Figure 5.8. Schematic representation of the novel x-ray detector

Here a commercially available x-ray intensifying screen which is typically used in medical x-ray diagnostics (Intensifying screen G 400 obtained from Primax Berlin GmbH) was chosen. These foils are based on a polymer matrix with embedded x-ray luminophors (doped with different rare earth materials) and show green luminescence ($\lambda_{max} \sim 545$ nm) when illuminated with x-rays.

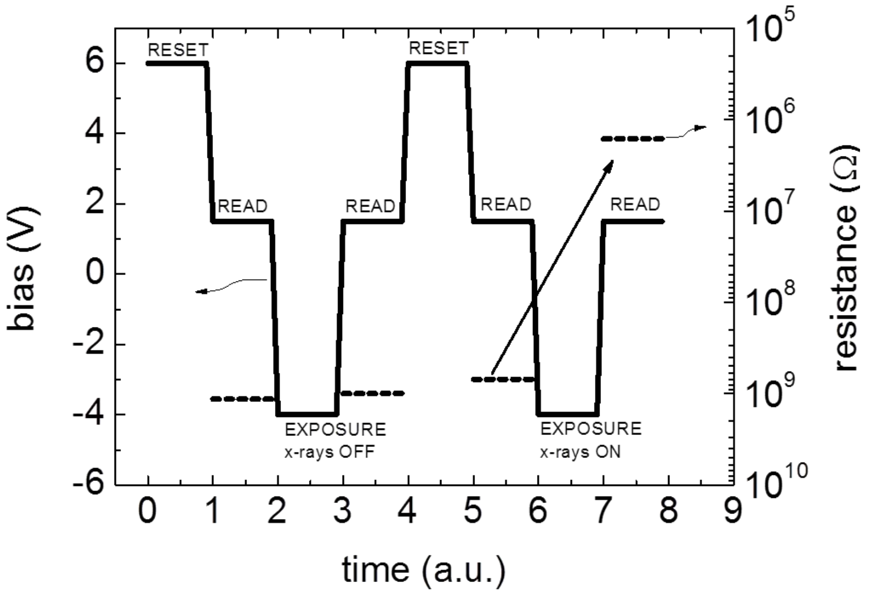

Figure 5.9. Detection capability of 8 kV x-rays. In the first part, the device was set to its exposure mode (-4 V) while the x-ray source was turned off. As expected, no significant change of the resistance state was found. In the second part, the x-ray source was turned on and a change of the resistance state of the resistive switching element was detected afterwards (factor of ~ 450).

A detection cycle can be summarized as follows: First, the system is initialized by applying the RESET voltage (+ 6 V). Then the stack is set to the detection - bias of -4 V (well above the specific threshold voltage). The resistive switch changes its resistance state in dependence of the light exposure. Afterwards, the written information can be read by measuring the resistance of the system (at 1.5 V) under dark conditions. The procedure is finished by resetting the system and making it ready for a new exposure (+6 V).

Figure 5.9 demonstrates a full cycle including a ‘dark’ reference measurement (noise level detection) at the beginning. As it is obvious, the device does not change its resistance state without illumination (and thus without x-rays). After turning on the x-ray source, the device changes its resistance from $7 * 10^8\ \Omega$ to $1.6 * 10^6\ \Omega$ (equals a ratio of ~ 450). This cycle was repeated several times on different devices.

5.6 Experimental Section

All fabrication and characterization steps were performed in an argon filled glovebox (residual gas: < 1 ppm O_2 and < 1 ppm H_2O).

Device fabrication

For the single devices and the 3 by 3 arrays, ITO coated quartz substrates with R <= 15 ohm/sq were patterned and used as substrate/transparent electrode. For the 32 by 32 array, ITO coated PET with a total thickness of 178 µm was used as transparent and flexible electrode (obtained from Solutia Inc.). The substrates were cleaned with deionised water, 2-propanol (for PET) and additionally acetone and toluene (for quartz) and subsequently dried. rr-P3HT and PCBM were purchased from Sigma-Aldrich and solved in a 1:1 ratio in high concentrations (80 mg/ml) in dichlorobenzene, heated up to 80°C and stirred for ~ 12 hours. Afterwards the solution was spin-coated on the cleaned substrates and dried at 80°C in vacuum for 30 minutes. A high solid content was chosen to ensure thick layers which significantly reduces dark current density. Finally the Ca/Al/Ag intermediate electrode, the Alq3 layer and the silver top electrode were deposited at a base pressure smaller than 10^{-6} mbar in a vacuum coating unit using different shadow masks. Note that the vacuum was not broken throughout the whole process.

Characterization

A -test stand for the characterization of the 32 by 32 pixel detector array was fabricated using a drop on demand 3D printer (OBJET 30 Pro) (Figure 5.10). Vero White (Objet) was used as ink. The wiring was done using basic electronic components. In the final design each bottom and top contact was simultaneously contacted. Each wire is then connected to a switching system, which was used to connect individual bottom and top electrodes with the source-measure unit (Agilent B1500A Parameter Analyzer). The measurements were done by biasing to the bottom contact, while the top contact was set to 0 V. A inorganic LED with $\lambda_{max} = 525$ nm and FWHM = 17 nm, well matching with the absorption spectrum P3HT:PCBM, was used as light source.

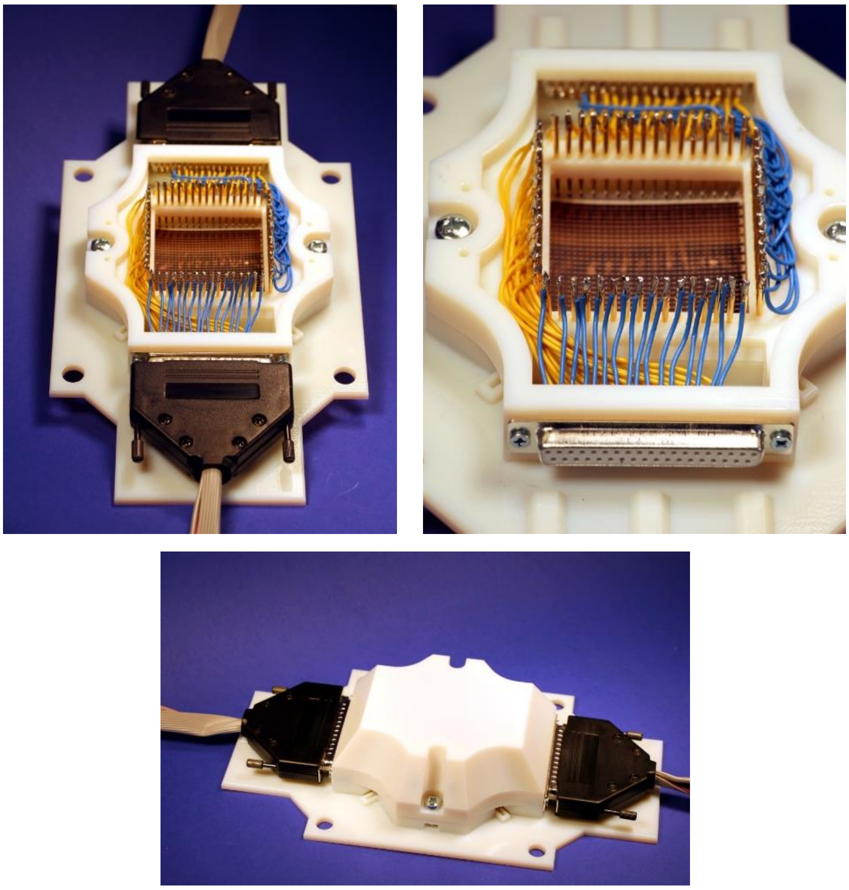

Figure 5.10. *Photographs of the custom-made test stand for the 32 by 32 pixel image detector.*

X-Ray detector

The devices were place in a customized measurement cell with a quartz window. X-rays are strongly attenuated in quartz and therefore any radiation induced damage of the organic device could be excluded. The scintillator was placed in close proximity of the window. Note that the used intensifying screen is opaque for visible light; therefore any contributions of ambient light could be excluded. The measurement cell was placed in front of an 8 kV x-ray source.

5.7 Summary

The prototype of a unique organic image detection array technology having many conceptual advantages compared to existing organic and inorganic image detector technologies has been presented. By vertically integrating an organic photodiode and an organic resistive switching element in one pixel, no additional building blocks such as transistors are needed for addressing the single nodes in an array. The 2-terminal wiring of two vertically stacked devices significantly reduces the footprint of a single pixel down to the theoretical limit of $4F^2$, allowing an integration with a high fill-factor. The presented features of simultaneous detection and storage of the image information directly in one pixel is closely related to the properties of inorganic CCD technology, but unlike CCD this detector array does not show a destructive read-out and does not exhibit any integrating behavior. By integration of 32 by 32 of these pixels in a crossbar setup, a 1024 bit image detector was fabricated on a flexible substrate and 4-bit grey scaling was demonstrated. With these essential features, the easy fabrication and simple wiring in combination with the advantages of organic electronics, the presented detector array is a substantial step towards industry imposed specifications. Upcoming work will focus on application related development towards the implementation of scintillator materials with our prototype and the realization of conformable x-ray detector arrays. Also, alternative to a photodiode, every other resistive sensor (e.g. pressure sensors or temperature sensors) might be suitable candidates for the integration together with resistive memories.

6 Electroluminescence Intensity and Color Tuning of Organic Light Emitting Diodes by Organic Resistive Switches

In this chapter, a unique optoelectronic device comprising solution processed polymer light emitting diodes (PLED) and ORS is presented. By fabricating an ORS on top of a PLED, it can be used to control the voltage drop across the PLED and thus the current. By selectively switching one or more ORS to different resistive states the emission properties – luminance or emission color - of the PLED can be tuned at constant operation voltage. This fact enables for driving the whole device with a constant voltage source e.g. a conventional battery and for a simple circuitry. In this context, a detailed discussion about the fabrication of highly efficient and color-stable PLEDs is given in the first part of this chapter.

Parts of this chapter 7.1 are published in
S. Nau, N. Schulte, S. Winkler, J. Frisch, A. Vollmer, N. Koch, S. Sax, E. J. W. List, ‚Highly Efficient Color-Stable Deep-Blue Multilayer PLEDs: Preventing PEDOT:PSS-Induced Interface Degradation ‘ Adv. Mater. 2013, 25, 4420.
The author of this thesis planned and performed all experiments, the data analysis and wrote the manuscript. N. Schulte synthesized the materials, S. W. and J. F. supervised the UPS measurements, A. V., N. K., S. S. and E. J. W. L. supervised the work.

Chapter 7.2 is part of a publication in preparation.

6.1 Highly Efficient and Color-Stable Polymer Light Emitting Diodes

This chapter reports on the electro-optical properties of novel light emitting copolymers (**CP**, further called **CP-AE**, **CP-ABCD**, **CP-ACD**) comprising different light emitting and transport supporting building blocks (Figure 6.1). In particular, the chemical degradation of the emissive units assigned to the acidity of PEDOT:PSS and a route to fabricate highly efficient and color-stable multilayer PLEDs will be addressed.

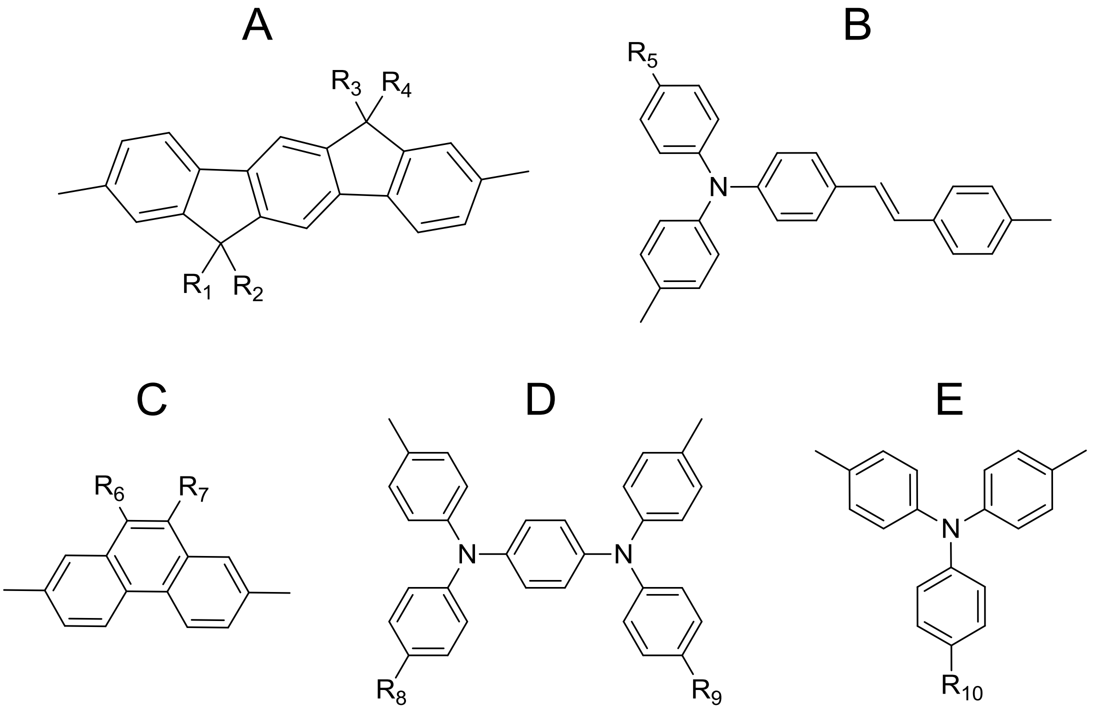

Figure 6.1. Chemical structure of the individual copolymer building blocks: ***A****: 9,9,12,12-tetraorganyl-6,12-dihydroindeno[1,2-b]fluorene;* ***B****: (E)-4-organyl-N-phenyl-N-(4-styrylphenyl)aniline;* ***C****: 9,10-diorganylphenanthrene* ***D****: N1,N4-bis(4-organylphenyl)-N1,N4-diphenylbenzene-1,4-diamine and E: 4-organyl-N,N-diphenylaniline; R1 - R10: organyl groups. CP-AE consists of component A and E, in the ratio of 50:50, CP-ABCD consists of component A, B, C and D in the ratio of A:B:C:D=46:2:50:2, CP-ACD consists of component A, C and D in the ratio of A:C:D=48:50:2.*

6.1.1 Introduction

Since the report on the first small molecule based thin film organic light emitting device[24] and the first polymer light emitting device (PLED)[25] remarkable efforts of the involved research community and a resilient industrial contribution have led to a number of commercial OLED-based products beyond the niche markets with large area applications in the field of flat-panel displays and lighting devices.[133] While fast improvements in the chemical stability of the active materials and reliability of the devices have led to well established red and green[134] fluorescent and phosphorescent emitters (both small molecules and conjugated polymers), there is still a quest for improved stability for materials emitting in the blue spectral range.

Amongst others, for the application as blue emitting conjugated polymers, poly(para-phenylene) (PPP) type and poly(pyrene)[135] type polymers are rather promising for stable PLED applications and therefore of particular interest. In addition to a well defined chemistry, PPP type polymers also allow for an effective emission color tuning from UV-blue to blue emission by increasing the number of aryl-aryl bridges; stretching from PPP[136] with a dominating UV emission, over poly(fluorene)[137,138] (UV-blue) and poly(indenofluorene)[139–141] (PIF - emitting further in the visible) to poly(pentaphenylene)[142], yielding deep blue emission perfectly matching with the sensitivity of the human eye for the blue color.

Besides the chemical stability of the particular emitter material and a high radiative quantum yield of the emissive unit, efficient and bright PLED devices with long lifetimes require a balanced charge carrier injection and an effective and balanced transport of electrons and holes towards the electro-optical active layer. Moreover a pinning of the emission zone to the center of the device, using heterojunctions with appropriate type II band level offset, to avoid quenching at either of the electrode interfaces has also been found to be rather favorable.[143] Modifications of the PEDOT:PSS surface as well as auxiliary injection layers[144–146], doped interface regions[147] or multiple tandem structures including interconnecting layers[148] have been used to enhance and balance charge injection/transport as well as exciton formation in the device.

Irrespective of the individual preparation techniques, the crucial issue of solution processed multilayer PLEDs is not to redissolve the preceding polymer layer by the solvent used to deposit the polymer of the subsequent layer. Different approaches have been suggested, ranging from liquid buffer layers between the individual polymer layers[149], in situ converted or crosslinked polymer layers[150–153] to the application of orthogonal solvent systems[154,155]. Alternatively, the stability against redissolving of a polymer film can be significantly increased by a thermal bake-out process.[156–158]

Independent of the specific device structure, the majority of polymer based light emitting diodes nowadays comprise a poly(3,4 ethylenedioxythiophene):poly(styrenesulphonic acid) (PEDOT:PSS) layer on top of the transparent bottom electrode due to its reasonable workfunction (4.8 to 5.6 eV), high conductivity range (~10^{-5}–10^{2} S/cm) and good hole injection ability.[159–163] Since the surface moiety of a PEDOT:PSS layer is sensitive to the preparation/storage conditions – vacuum annealed samples tend to form PSS rich surfaces while water vapor supports the decrease of the PSS concentration on top of the layer[164] - the overall performance of a PLED can be considerably altered. In particular, enhanced concentrations of the insulating PSS moieties are held to be responsible for electron blocking at the interface.[165,166] In the case of using the desired low workfunction cathode materials, electrons, representing the charge carrier majority, tend to accumulate at the PSS rich phase increasing the hole injection because of strong electric fields in the anode region, leading to improved charge carrier balance and higher device efficiencies.[167]

Even though PEDOT:PSS is widely used for PLEDs due to its beneficial properties, it suffers from many drawbacks like its acidic character[168,169], exciton quenching[170], field induced migration of PEDOT-cations[171] and the possible chemical degradation of the light emitting polymer[172]. These impacts can be avoided or at least minimized by integrating an appropriate acid stable interlayer between the organic-PEDOT:PSS interface.

The molecular design of the copolymers was optimized with particular emphasis on a) efficient exciton formation, b) light emission in an energy region of reasonable eye sensitivity for the blue color, c) enhanced charge carrier transport properties for electrons and holes, d) appropriate energy level positions facilitating both charge injection and blocking in a polymer heterostructure and e) suppression of PEDOT:PSS induced spectral degradation of the emissive units. As hole-transport and -injection layer the alternating copolymer **CP-AE** is used, which contains component **A** (indenofluorene) and **E** (triphenylamine) A:E=50:50. Copolymer **CP-ABCD**, comprising an indenofluorene unit (**A**), an (E)-4-organyl-N-phenyl-N-(4-styrylphenyl)aniline emissive unit (**B**), electron transport supporting phenanthrene (**C**) and hole transport supporting amine (**D**) units in the ratio A:B:C:D=46:2:50:2, is used as emissive layer. Additionally the copolymer **CP-ACD** (A:C:D=48:2:50) was investigated in comparison to **CP-ABCD** which only differs by the additional emissive unit **B**.

6.1.2 Photo-physical investigations

Figure 6.2a, Figure 6.2b and Figure 6.2c show the thin film absorbance and photoluminescence (PL) spectra of the three utilized CP's as well as the PL film spectra of CP layers deposited on PEDOT:PSS and CP films mixed with trifluoroacetic-acid (TFA) to demonstrate the possibility of a chemical degradation of the emissive units of the copolymers. As depicted in Figure 6.2a, **CP-AE** shows an unstructured absorption spectrum with its maximum at 406 nm. The emission maximum of the **CP-AE** thin film PL spectrum was found at 435 nm with the first vibronic peak at 461 nm. Except for a bathochromic shift of ca. 10 meV, which is attributed to the high concentration of copolymerized amine based hole transport units[173], both the emission and absorption spectra are prototypical for PIF. Figure 6.2b shows the absorption spectrum of **CP-ACD** with its maximum located at 404 nm and a slight shoulder at 385 nm. The thin film emission maxima, found at around 423 nm and 451 nm, are assigned to the π-π* transition and the first vibronic progression of the copolymer. As it becomes evident in Figure 6.2c, the absorption spectrum of **CP-ABCD** does not show any significant modifications compared to **CP-ACD** since the additional emissive component **B** is only present in a low concentration. Nevertheless, the PL emission spectrum is seriously influenced by the introduced co-emitter **B**; the maximum of the spectrum is shifted towards longer wavelengths by ca. 20 meV to 457 nm with a shoulder at 480 nm. This significant shift of the PL emission spectrum as well as the strong reduction of the **CP-ACD** emission peak at 423 nm clearly demonstrates the distinct impact of component **B,** resulting in a perfect overlay with the sensitivity of the human eye.

Yet, it is known from literature that polymers containing pyridine units[174], vinylene units[175] or distinct end-chain groups[176] may be prone to degradation in an acidic environment. Therefore all copolymers have been tested for possible influences to the emissive spectrum by PEDOT:PSS and in particular by the PSS-rich phase at the interface. As depicted in Figure 6.2c, the emission spectrum of **CP-ABCD** undergoes a considerable change when comparing a thin film PL spectrum on glass and on PEDOT:PSS, where for the latter one finds a reduction of the emission peak at 457 nm by more than 60%. To clarify the acidic influence on the emission **CP-ABCD** was also blended with TFA and the PL of thin films was measured, where indeed exactly the same reduction of the PL emission at 457 nm was observed. In accordance with the spectra obtained from PEDOT:PSS/copolymer double layer systems, where essentially no alteration for **CP-ACD** and **CP-AE** on PEDOT:PSS was found, also the blends TFA:**CP-ACD** (Figure 6.2b, Figure 6.3) and TFA:**CP-AE** (Figure 6.2a, Figure 6.3) did not exhibit any significant changes in the PL spectrum. Comparing the chemical structures of **CP-ACD** and **CP-ABCD,** the observed spectral change can be attributed to an electrophilic addition of the acid with the nucleophilic carbon double bond of the vinylene units[175] (component **B**), leading to a strong quenching of the PL at this copolymer site.

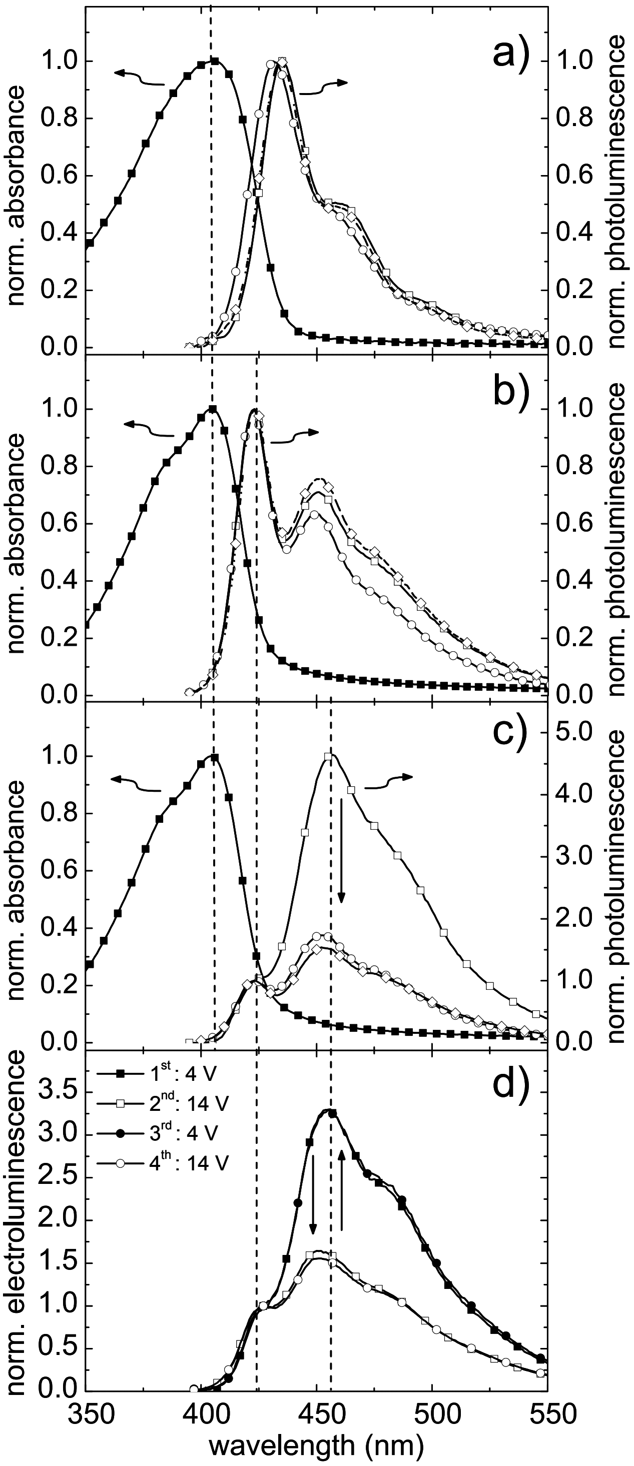

Figure 6.2. Absorbance and photoluminescence spectra of a) CP-AE, b) CP-ACD, and c) CP-ABCD; thin film absorbance spectra (filled squares); thin film PL spectra (open squares); thin film PL spectra of a PEDOT:PSS/CP double layer (open circles); thin film PL spectra of a CP-trifluoroacetic acid blend (open diamonds). d) Normalized electroluminescence emission spectra of an ITO/PEDOT:PSS/CP-ABCD (60 nm)/Ca (10 nm)/Al (100 nm) device biased at 4 V (1st, full squares, 3rd, full circles) and 14 V (2nd, open squares, 4th, open circles), respectively.

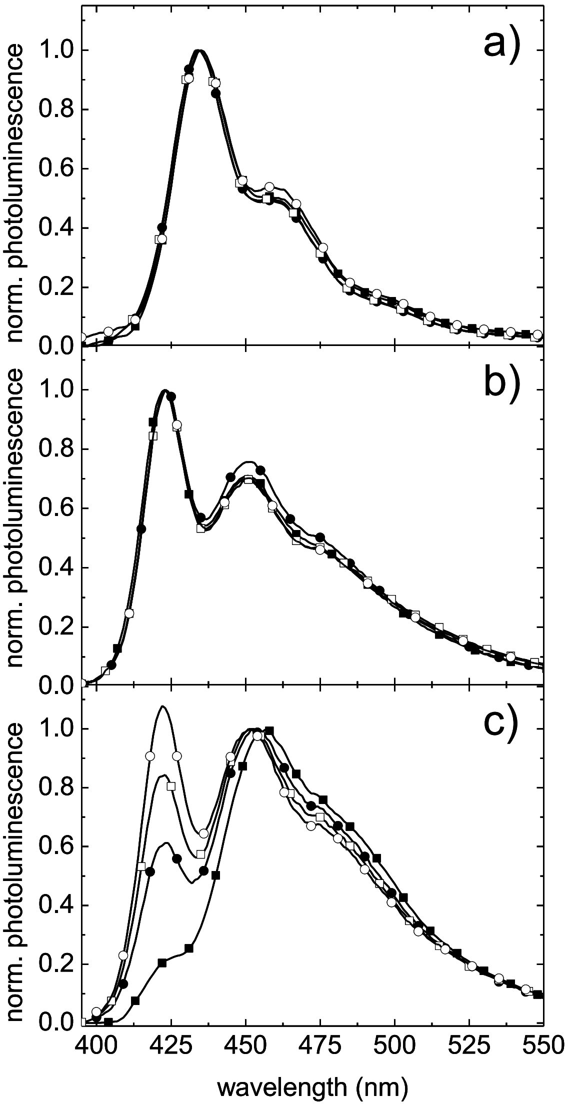

Figure 6.3. Normalized PL thin film emission spectra of a) CP-AE b) CP-ACD and c) CP-ABCD on glass substrates in dependence of TFA concentration; PL spectra without acid (full squares); PL spectra with 0.5 % TFA blended to the solution (full circles); PL spectra with 1% TFA blended to the solution (open squares); PL spectra with 2% TFA blended to the solution (open circles). For CP-AE and CP-ACD no influence of the acid was found. For CP-ABCD, the emission feature at 424 nm develops to a distinct peak with increasing acidic content.

6.1.3 Investigations on PLED devices

In addition to PL measurements, the influence of PEDOT:PSS on **CP-ABCD** was also investigated in a PLED device structure (ITO/PEDOT:PSS/**CP-ABCD**/Ca/Al PLED). As depicted in Figure 6.2d the electroluminescence (EL) spectrum can be reversibly changed as a function of the bias voltage with respect to the emission peak at 457 nm. At 4 V, the EL spectrum mostly equals the corresponding **CP-ABCD** single layer PL spectrum (Figure 6.2c, open squares) with a maximum at 455 nm and two additional features at 426 nm and 482 nm. Increasing the bias voltage to 14 V leads to a reduction of the maximum emission peak at 457 nm of more than 50%, comparable to the change found in the PL spectrum from the PEDOT:PSS/**CP-ABCD** double layer or the TFA:**CP-ABCD** films (Figure 6.2c, open circles; open diamonds). Since this behavior is shown to be fully reversible, general device degradation can be excluded and the change in the EL spectrum can be assigned to a voltage dependent movement of the recombination zone[177–179] forwards and backwards with respect to the PSS/**CP-ABCD** interface with degraded vinylene units due to the interaction with PSS.

While tentatively discussed in literature[172] the here presented result clearly demonstrates that the acidity of the PEDOT:PSS layer can distinctively alter the device performance/stability due to exciton quenching at the emissive units at the interface, accompanied by changes in the overall spectral emission characteristics and a reduction of the device stability. Particularly when using low workfunction cathode materials, where the charge carrier recombination zone tends to shift towards the anode, the chemical stability of the emissive units close to the interface with PEDOT:PSS is of crucial importance.

In order to impede interactions at the PEDOT:PSS/**CP-ABCD** interface in PLEDs as well as to improve hole transport towards the **CP-ABCD** layer an additional hole transport layer using **CP-AE** was integrated. To avoid a redissolving during the device preparation the **CP-AE** layer was stabilized by thermal curing at 200°C for 1 hour in argon. This bake-out did not result in any significant change of the absorbance or of the PL spectrum (Figure 6.4). Atomic force microscopy investigations reveal that **CP-AE** films cured at 200°C did not show a noteworthy film thickness decrease after being washed with pure solvent, whereas films baked at 70°C can still be completely removed.

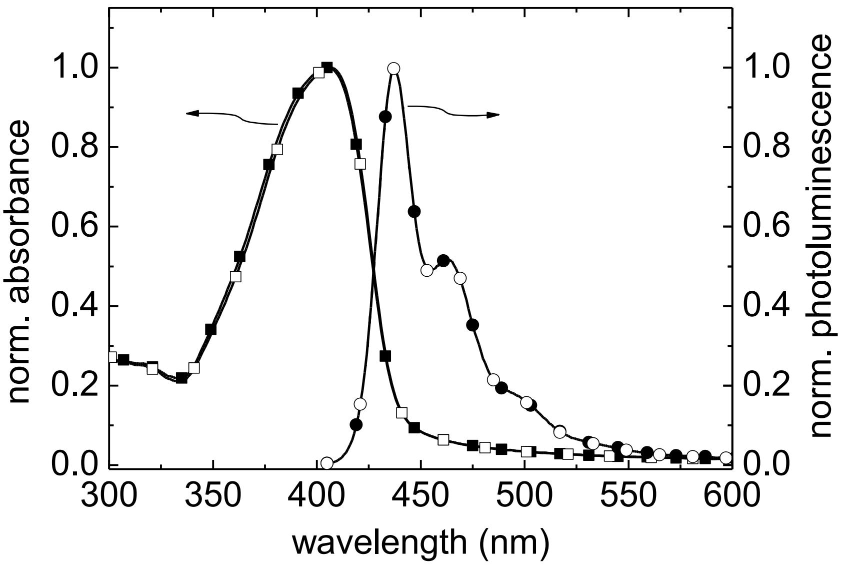

Figure 6.4. *Influence of a thermal bake out to the photophysical thin film properties of CP-AE. Spectra were recorded before (absorbance: full squares; PL: full circles) and after (absorbance: open squares; PL: open circles) a 200°C curing process for 1 hour in argon. No distinct changes can be found for the normalized spectra.*

Compared to devices without CP-AE, ITO/PEDOT:PSS/CP-AE/CP-ABCD/Ca/Al devices did not show the distinct bias voltage dependent change of the EL emission spectrum (Figure 6.5) but a significant device efficiency enhancement from 1 cd A^{-1} to 1.9 cd A^{-1} at 1000 cd m^{-2} (Table 6.1). In Figure 6.5, only a slight broadening of the spectrum of ITO/PEDOT:PSS/CP-AE/CP-ABCD/Ca/Al was obtained for higher bias levels which can be ascribed to a broadening of the recombination zone, leading to an overlap of the spectral contribution of CP-AE with the major spectral contribution from CP-ABCD. Since higher bias values led to a permanent device breakdown, only spectra up to 10 V are shown for the CP-AE/CP-ABCD multilayer device.

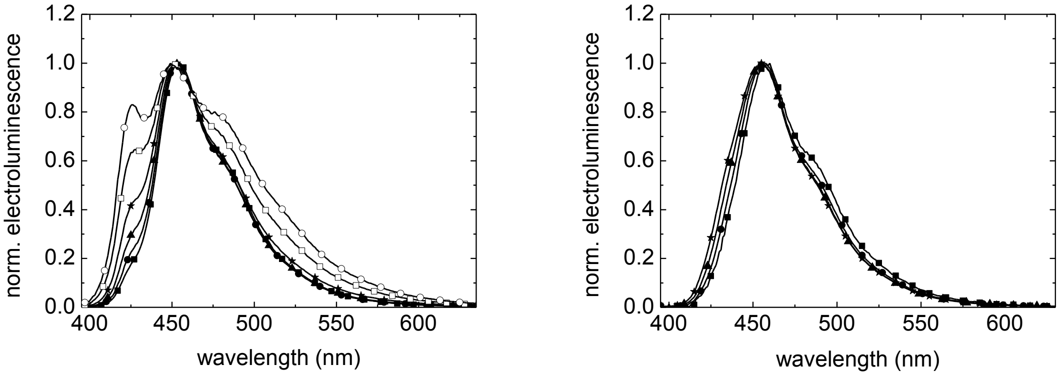

Figure 6.5. Electroluminescence spectra obtained from an ITO/PEDOT:PSS/CP-ABCD/Ca/Al device (left) and an ITO/PEDOT:PSS/CP-AE/CP-ABCD/Cs2CO3/Al device (right) in dependence of the applied bias voltage: full squares: 4 V; full circles: 6 V; full triangles: 8 V; full stars: 10 V; open squares: 12 V; open circles: 14 V.

Besides the enhanced hole transport properties of **CP-AE**, this significant performance enhancement is a result of an optimum type II band alignment at the **CP-AE**/**CP-ABCD** interface as determined by photoelectron spectroscopy (UPS) (Figure 6.6). Therefore valence band region spectra and the secondary electron cut off was measured after each layer deposition step. **CP-AE**´s (**CP-ABCD**´s) low binding energy onset is 0.6 eV (0.9 eV) below the fermi level; this energy offset corresponds to the hole injection barrier from PEDOT:PSS. Together with the work function determined from the secondary electron cutoff, the corresponding ionization energy can be found at 5.5 eV (5.8 eV). Based on the optical band gaps, the onset of the lowest unoccupied molecular orbital (LUMO) can be assumed to be at 2.6 eV for **CP-AE** and 2.8 eV for **CP-ABCD** below the vacuum level. Consequently, **CP-AE** is operative as an additional energy level in this staggered heterojunction, enabling stepwise hole injection from PEDOT:PSS into **CP-ABCD**. In contrast, electrons are blocked at the **CP-AE**/**CP-ABCD** interface, being favorable for the device performance.

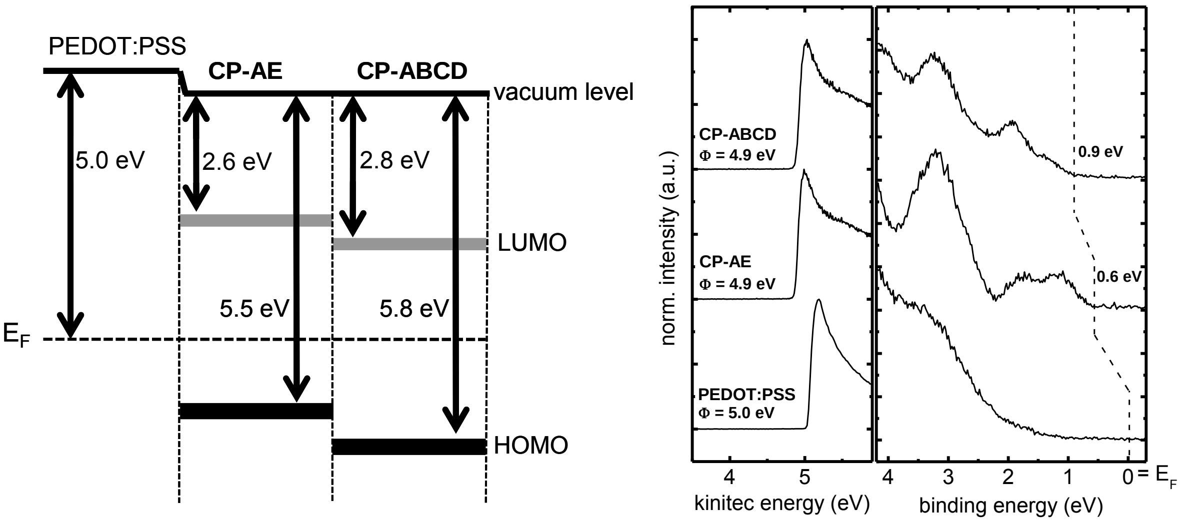

Figure 6.6. Schematic energy level diagram of the PEDOT:PSS/CP-AE/CP-ABCD multilayer structure obtained from layer by layer UPS investigation (left). Secondary electron cutoff (left) and valence region UPS (right spectra) of the multilayer structure (right)

In a final step, a further considerable device efficiency enhancement was achieved by using a caesium carbonate cathode (Cs_2CO_3, workfunction around 2.1 eV[180]) instead of a calcium cathode with its significantly higher workfunction around 2.9 eV. Figure 6.7 shows the voltage-current and the voltage-luminescence characteristics as well as the corresponding electroluminescence spectrum of the optimized ITO/PEDOT:PSS/**CP-AE**/**CP-ABCD**/Cs_2CO_3/Al structure. The inset shows the electroluminescence spectrum of the **CP-AE**/**CP-ABCD** double layer device with its maximum at 459 nm and a weak shoulder at around 480 nm. Changing the cathode material from calcium to caesium carbonate nearly doubles the efficiency from 1.9 cd A^{-1} to 3.7 cd A^{-1} at 1000 cd m^{-2}. Figure 6.8 shows the device efficiency in dependence of the current density for the three **CP-ABCD** based devices. At low current densities, a high efficiency with an initial value of 9.7 cd A^{-1} was found for the optimized structure, but a high roll-off is observed as well. Since no roll-off is present for the two other **CP-ABCD** based devices, we ascribe this to the strongly enhanced electron injection at high bias levels and a progressive unbalance of electrons and holes. Nevertheless, independent of the applied current density the obtained device efficiencies are at least three to four times higher than for the device without the **CP-AE** interlayer. Additionally to the high current efficiencies, a high brightness with luminance values up to 10600 cd m^{-2} was found for this multilayer approach.

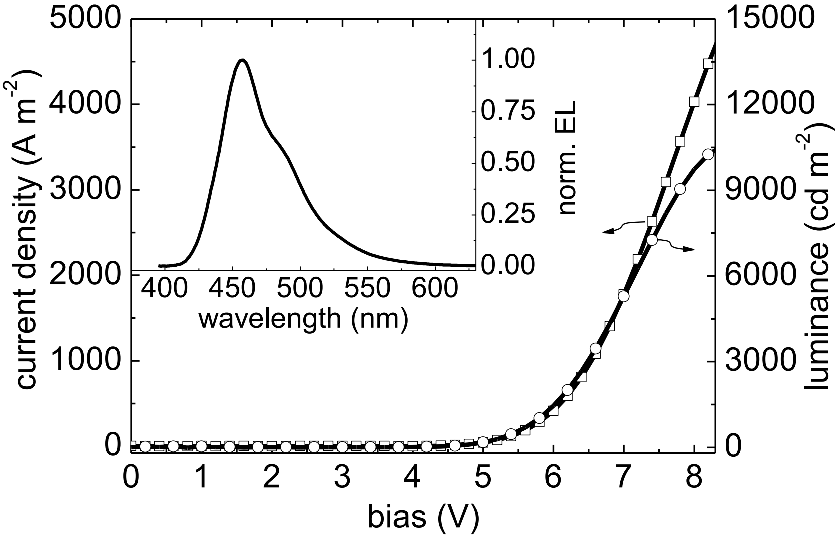

Figure 6.7. Current density (open squares) and luminance (open circles) as a function of the bias voltage in an ITO/PEDOT:PSS (60 nm)/CP-AE (20 nm)/CP-ABCD (60 nm)/Cs$_2$CO$_3$ (0.15 nm)/Al (100 nm) device. The inset shows the normalized EL spectrum of the device with CIE coordinates x=0.144; y=0.129.

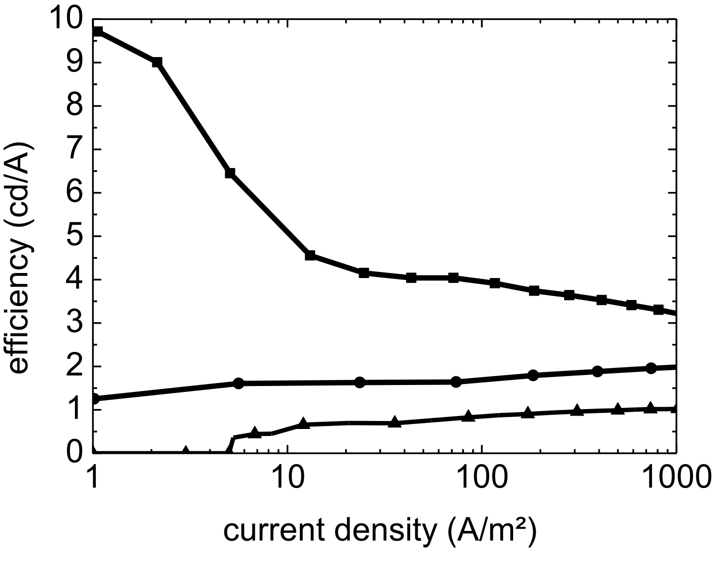

Figure 6.8. Device efficiency in dependence of the current density for an ITO/PEDOT:PSS/CP-ABCD/Ca/Al device (triangles), an ITO/PEDOT:PSS/CP-AE/CP-ABCD/Ca/Al device (circles) and an ITO/PEDOT:PSS/CP-AE/CP-ABCD/Cs$_2$CO$_3$/Al device (squares).

In order to demonstrate the distinct contribution of component **B** to the device efficiency, the reference copolymer **CP-ACD**, was examined in an ITO/PEDOT:PSS/**CP-AE**/**CP-ACD**/Cs_2CO_3/Al configuration, leading to a lower overall efficiency of 2.8 cd A^{-1} at 1000 cd m^{-2}.

Table 6.1 Electro-optical properties of single and multilayer devices with different electrode configurations

PLED configuration	max. Efficiency [cd A^{-1}]	Efficiency @1000 cd m^{-2} [cd A^{-1}]	CIE1931 coordinates
ITO/PEDOT:PSS/CP-AE/CP-ACD/Cs_2CO_3/Al	7.3 cd A^{-1}	2.8 cd A^{-1}	x=0.148; y=0.149
ITO/PEDOT:PSS/CP-ABCD/Ca/Al	1.0 cd A^{-1}	1.0 cd A^{-1}	x=0.144; y=0.125
ITO/PEDOT:PSS/**CP-AE**/**CP-ABCD**/Ca/Al	2.1 cd A^{-1}	1.9 cd A^{-1}	x=0.144; y=0.125
ITO/PEDOT:PSS/**CP-AE**/**CP-ABCD**/Cs_2CO_3/Al	9.7 cd A^{-1}	3.7 cd A^{-1}	x=0.144; y=0.129

6.2 Integration of OLEDs with Organic Memories

Although OLEDs outperform their inorganic counterparts in some aspects, the lack in performance of organic selector devices (organic field-effect transistors) makes the use of inorganic transistors necessary to obtain the full performance and dynamic range for display applications. This certainly limits the impact of the claimed advantages of organic electronics as flexibility, weight, transparency, etc. and is furthermore a substantial additional cost factor.

Various different attempts were made to use memory devices as a switch to control light emission. Ferroelectric switches were used to drive OLED devices in a passive matrix array.[181] Resistive switches, similar to the ones described in this thesis, were used, but their functionality was reduced to a simple ON/OFF switch for the OLED.[182–186] Similar attempts have been also demonstrate for completely inorganic systems.[187] In each case, tuning of luminance was only possible by changing the driving bias. In the following, a novel device capable of manipulating luminance or the electroluminescence spectrum and as such the emission color is presented. By fabricating an ORS on top of a PLED (Figure 6.9), it can be used to control the voltage drop across the PLED and thus the current. Selectively switching one or more ORS to different resistive states the emission properties – luminance or emission color - of the PLED can be tuned at *constant* operation voltage. This allows to drive the whole device with a constant voltage source e.g. a conventional battery and a simple circuitry.

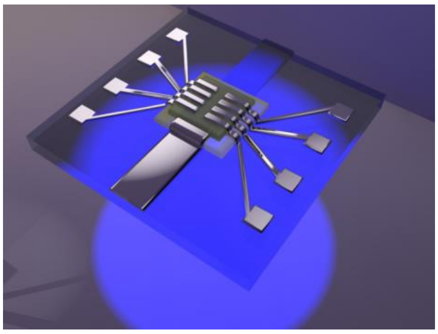

Figure 6.9. Illustration of the device stack consisting of a PLED with eight ORS on top

6.2.1 Luminance control

For the presented application, a high current in the LRS is required to drive the light emitting device. However, due to the lack of knowledge about the filament forming process the maximum current levels can only be influenced to a limited extend. Typical current through a filament was found to be in the range of 10 µA – 1 mA (at 1 V). Since this parameter seems to be fixed, here a PLED with a high current efficiency was implemented to ensure proper functionality of the device stack. A blue light emitting poly(indenofluorene) based PLED with efficiencies up to 9.7 cd/A and a luminance up to 20000 cd/m^2 was chosen and fabricated as reported in chapter 6.1. The IV and luminescence-V characteristics as well as the electroluminescence spectrum (CIE1931 x = 0.141; y =0.125) are shown in Figure 6.7.

Eight individual ORS devices were processed on top of the cathode of the PLED resulting in a ITO/PEDOT:PSS/HIL/LEP/Ca/Al/Ag/Alq3/Ag stack. The luminance of such a stack can be increased straightforwardly by switching the ORS cell by cell to its LRS resulting in an increase of the voltage drop across (and thus current through) the PLED. This is done by applying the SET voltage to a single element as indicated in Figure 6.10. Accordingly, the luminance can be decreased by switching the individual ORS back to the HRS by applying the RESET voltage.

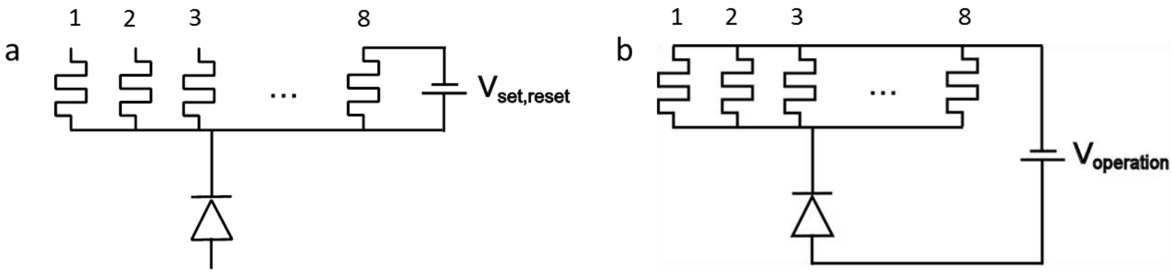

Figure 6.10. Sketch of the operation principle of the introduced device stack. a) To manipulate the resistance state of an individual ORS, it is connected to the voltage supply via an additional electrode. All other terminals are floating. b) For the ORS controlled PLED operation, the operation voltage is applied to the whole stack.

This procedure results in the data presented in Figure 6.11, where the luminance was stepwise tuned from 0 cd/m² up to 450 cd/m², back to 0 cd/m² and up again. Importantly the driving bias of the full device remained unchanged throughout the whole sweep. It is observed that the individual ORS devices do not contribute equally to the current/luminance, which is due to large resistance range covered by LRS – states . Certainly more effort to control this issue is necessary.

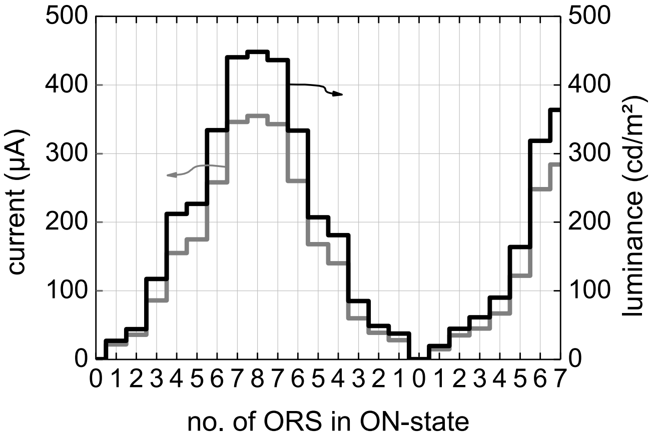

Figure 6.11. Control of luminance by selectively switching up to eight ORS into their LRS. The driving voltage of the whole stack was kept constant at 5.5 V

6.2.2 Color tuning

The very same principle can be used to tune the emission color of a PLED. The focus here lies on the tuning of the color temperature of white light emitting diodes. Amongst others, white light emission can be achieved by carefully balancing the emission spectrum of the light emitting diode by using different luminophores as poly(fluorene) and Poly[2-methoxy-5-(2-ethylhexyloxy)-1,4-phenylenevinylene] (MEH-PPV) in certain weight ratios.[188] This leads to largely bias independent emission spectra as it is usually desired. To tune the emission color we here introduced an emissive host-guest system comprising a blend of polymers as host (matrix) and a phosphorescent transition metal complex as guest (dopant). Such systems exhibit the desired features, namely white light emission and a voltage dependent emission spectrum. The latter is caused by saturation of the dopant at higher current densities[188–190], caused by the strong imbalance of excited state lifetimes between fluorescent (~ ns) and phosphorescent (~µs-ms) materials and the strongly different weight ratios. This principle is demonstrated in Figure 6.12, where a fluorescent poly(indenofluorne) derivative is doped with a red phosphorescent dye. Strong emission color dependence is found.

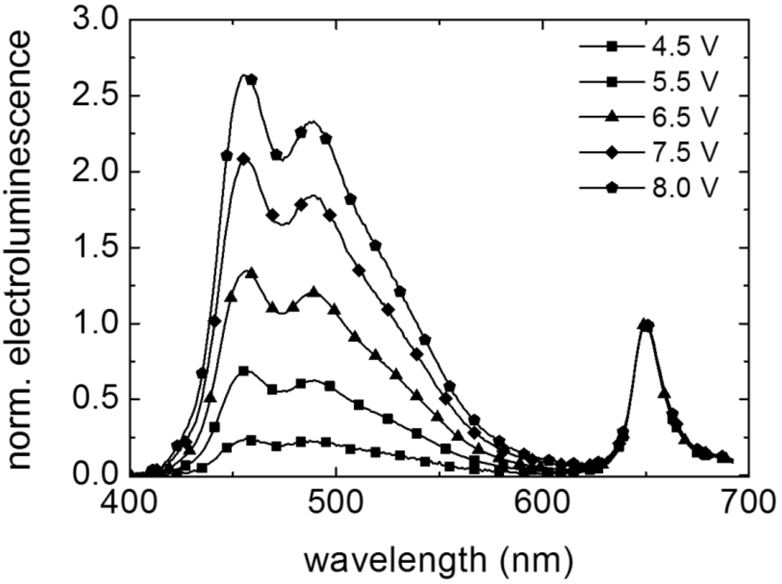

Figure 6.12. Dependence of the electroluminescence spectrum on the driving voltage.

For the actual application with the ORS, poly(indenofluorene):MEH-PPV blend was used as the fluorescent host material, whereas the phosphorescent triplet emitter platinum octaethylporphyrin (PtOEP)[191] was used as guest. The device setup was similar to the above discussed: ITO/PEDOT:PSS/PIF:MEH-PPV:PtOEP/Ca/Al/Ag/Alq3/Ag. If all ORS are switched to their HRS (all OFF), strong red emission is found with slight contributions from the blue region (Figure 6.13). By gradually increasing the number of ORS in their LRS, the blue spectral components start to emerge. This process ends up with a balanced emission between red and blue when each ORS in its LRS. The corresponding CIE 1931 coordinates can be found in Table 6.2. Note that the driving voltage of the stack was constant (5.5 V) at any time of the experiment. The emission is found to be close to the Planckian locus.

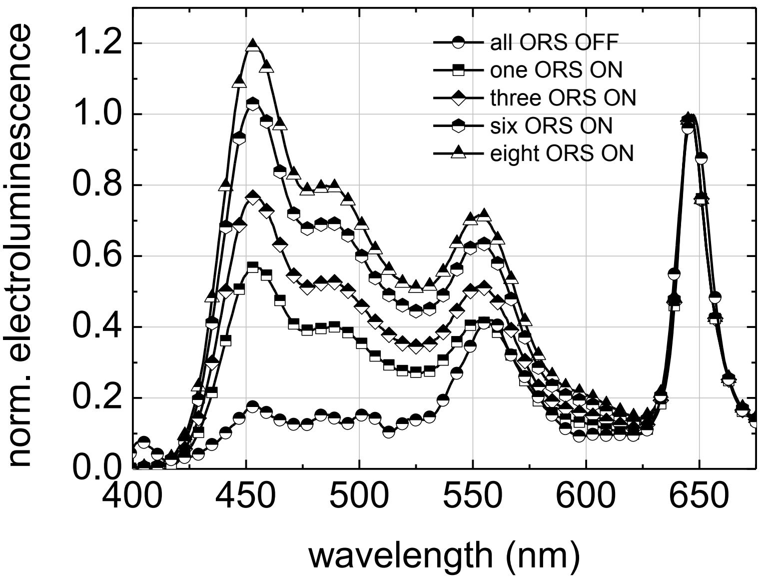

Figure 6.13. Electroluminescene spectrum in dependence of the number of ORS switched to their LRS. The drving voltage of the stack was constant at 5.5 V

Table 6.2. CIE 1931 coordinates of the electroluminescence emission characteristics in dependence of the number of ORS devices in theirs LRS

	CIE 1931 coordinates	
Number of ORS in the LRS	x	y
0	0,372	0,392
1	0,283	0,314
2	0,286	0,316
3	0,269	0,305
4	0,268	0,305
5	0,266	0,303
6	0,255	0,296
7	0,254	0,296
8	0,250	0,293

6.3 Experimental

UV-Photon Spectroscopy

Ultraviolet Photoemission Spectra were recorded using a hemispherical electron spectrometer (Scienta SES 100, resolution 120 meV) at the end station SurICat (beamline PM4) of the synchrotron light source BESSY II, consisting of an interconnected sample preparation and analysis chamber in ultrahigh vacuum (UHV), with a base pressure of 10^{-8} mbar and 10^{-10} mbar, respectively. The excitation energy was 35 eV and for measurement of the secondary electron cutoff the sample was biased at -10 V to clear the analyzer work function.

Optical spectroscopy

For the basic characterization of the absorption and the PL behavior a two beam Perkin Elmer Lambda 900 spectrometer and a Shimadzu RF-5301 PL spectrofluorophotometer were used. All PL spectra were corrected with the detector specific sensitivity curve.

Device fabrication/characterization

ITO covered glass substrates were cleaned in acetone, toluene and isopropanol and subsequent exposed to oxygen plasma. PEDOT:PSS (H.C. Stark Al 4083) layers were spin coated under ambient conditions and dried at 120°C under inert atmosphere. Each copolymer was solved in toluene with a concentration of 3 g/l (**CP-AE**) and 4 g/l (**CP-ABCD**, **CP-ACD**) and spin coated on top of the PEDOT:PSS layer resulting in film thicknesses of about 20 nm/60 nm. The **CP-AE** interlayer was thermally stabilized at 200°C for 60 minutes under argon atmosphere whereas the subsequently coated **CP-ABCD** was dried at 70°C for 60 minutes under high vacuum.

For the devices where color tuning was demonstrated, 0.5 wt% of MEH-PPV and 0.4 wt% PtOEP (both solved in toluene) were blended into a solution of CP-ABCD with a solid content of 4 g/l. All layer thicknesses were measured by atomic force microscopy (Veeco Dimension V and a Nanoscope V Controller). The multilayer cathode was thermally deposited in a vacuum coating unit at base pressures less than 10^{-6} mbar. The luminescence/voltage (LV) measurements were performed using a silicon photodiode and a computer controlled Keithley 2612 source measurement unit. Spectral characterization was done with a LOT-ORIEL Multispec equipped with a DB 401-UV CCD camera from Andor

6.4 Summary

In conclusion, the fabrication of highly efficient blue light emitting multilayer PLEDs was demonstrated to be possible without using orthogonal solvable polymers by employing the novel combination of the copolymers **CP-AE/CP-ABCD** with optimized building blocks. We demonstrate that the hole transporting polymer **CP-AE** leads to more balanced charge carrier injection as well as charge blocking at the polymer interface due to an optimum band level alignment. Therefore the recombination zone is shifted away from the PEDOT:PSS interface, which was shown to cause defect induced exciton quenching and spectral changes, into the **CP-ABCD** layer. The introduction of the **CP-AE** layer not only led to an enhanced spectral stability but also to a clearly increased device efficiency (Table 6.1). A further efficiency increase was obtained by changing the cathode material from calcium to caesium carbonate. The final ITO/PEDOT:PSS/**CP-AE**/**CP-ABCD**/Cs_2CO_3/Al PLED showed pure blue emission (CIE x=0.144; y=0.129), a high luminescence intensity and notably, up to now, one of the highest ever reported current efficiencies for blue multilayer PLEDs of 9.7 cd/A.

The second part of the chapter showed how to interface this PLED with several ORS. By fabricating up to eight ORS on top of a PLED, they can be used to manipulate the voltage drop across the light emitting diode. Depending on the composition of the light emitting material, two different operation modes have been identified. Firstly, for monochromatic emitters, luminance tuning was shown to be possible (0 cd/m^2 to 450 cd/m^2). Secondly, by introducing a white light emitting host – guest system as emissive layer it was shown that the emission color can be tuned over a large range.

7 Conclusions

The main scope of this thesis was the investigation of organic resistive switching devices, the clarification of their working mechanism, the exploration of alternative low-cost fabrication techniques and their emerging applications in the field of photonics.

One major topic of this work was the clarification of the working mechanism of ORS (Chapter 3). Photovoltaic measurement based analysis of ORS combined with impedance spectroscopy provided a solid proof that the picture of the equivalent circuit of a solar cell is valid and memory functionality can be assigned to a variable shunt resistance (e.g. due to the growth and rupture of a conductive filament). The charging based model can be clearly ruled out to play a major role due to the constant short circuit current of devices under illumination as well as due to the constant capacitive contribution in the AC-spectra, independent of the individual resistance state. Moreover, all presented devices showed qualitatively similar IV-characteristics independent of their specific architecture and the used organic- and electrode materials, except from the absolute device currents. The strong variation in the HRS currents can be explained by the different bulk conductivity of the organic materials as well as by the different architectures. As expected, PMMA based devices have the lowest HRS-current. Even though smaller, a variation can also be observed for the LRS current attributed to the stochastic nature of the filament formation process. A strong difference was found during the forming of bi-stability. While single layered device need an extended conditioning procedure, devices with additional metal particles incorporated in the organic matrix quickly show bi-stability, indicating that the metallic particles promote the growth of a filament.

The experimental results strongly indicate a filament formation mechanism as the dominant resistance switching process. In strong contrast to previously published work, it was possible to exclude contributions of π-conjugation and charge trapping. It is suggested that unipolar resistance switching is a fundamental property of metal/organic/metal systems, making this finding significant for researchers working on other organic thin-film ‘sandwich’ devices. For example in devices like organic photovoltaic devices or organic light emitting diodes, the formation of parasitic pathways through the device is doubtless an undesired side-effect. The understanding of their working mechanism is essential for all following fabrication related topics and applications.

Inkjet printing as an alternative fabrication method was explored (Chapter 4). The first all inkjet-printed resistive memory elements and their integration into crossbar array structures with high-performance organic rectifiers as selector elements has been demonstrated. The integration of printed ORS in a 5 by 5 array was achieved by stacking a pentacene-based high performance diode on top of each ORS. Further, an analytical expression to estimate the requirements for a diode for a given array size was deduced. Proper cross-talk handling was demonstrated on the basis of a series of information patterns written into a 2 by 2 sub array. This unambiguously shows that ORS are perfectly suited for low cost inkjet-printing based fabrication methods. Especially their insensitivity with respect to ambient preparation conditions significantly simplifies this process.

The device functionality of ORS is not limited to memory applications. Here, the prototype of a unique organic image detection array technology with many conceptual advantages compared to existing organic and inorganic image detector technologies was presented (Chapter 5). By vertical integration of an organic photodiode and an organic resistive switching element in one pixel, no additional building blocks such as transistors are needed for addressing the single nodes in an array. The 2-terminal wiring of two vertically stacked devices significantly reduces the footprint of a single pixel down to the theoretical limit of $4F^2$. The presented features of simultaneous detection and storage of the image information directly in one pixel is closely related to the properties of inorganic CCD technology, but unlike CCD this detector array does not show a destructive read-out and does not exhibit any integrating behavior. Through the integration of 1024 pixels in a 32 by 32 crossbar setup, an image detector was fabricated on a flexible substrate and 4-bit grey scaling capability was demonstrated. With these essential features and the easy fabrication as well as the simple wiring in combination with the advantages of organic electronics, the presented detector array is a substantial step towards industry imposed specifications. As an advancement of this novelty, the additional integration of scintillator materials, allowing for the detection of X-Rays, was shown.

The final part of this thesis showed a luminescence and color tunable OLED (6.2). Fabricating up to eight ORS on top of a PLED, they can be used to manipulate the voltage drop across the light emitting diode. Depending on the composition of the light emitting material, two different operation modes have been identified. First, for monochromatic emitters, luminance tuning was demonstrated. Second, by introducing a white light emitting host – guest system as emissive layer it was shown that the emission color can be tuned over a large spectral range. Due to the fact that organic transistors mostly do not exhibit the required performance parameters to properly act as selector device for OLEDs or OPDs, ORS might be a possible candidate to fill this gap.

Along these lines, also the fabrication of a highly efficient solution processed blue light emitting diode was presented by employing the novel combination of the copolymers CP-AE/CP-ABCD with optimized building blocks (Chapter 6.1). It was shwon that the hole transporting polymer CP-AE leads to more balanced charge carrier injection as well as charge blocking at the polymer interface due to an optimum band level alignment. Therefore the recombination zone is shifted away from the PEDOT:PSS interface, which was shown to cause defect induced exciton quenching and spectral changes, into the CP-ABCD layer. The introduction of the CP-AE layer not only led to an enhanced spectral stability but also to a clearly increased device efficiency. A further efficiency increase was obtained by changing the cathode material from calcium to caesium carbonate. The final ITO/PEDOT:PSS/CP-AE/CP-ABCD/Cs_2CO_3/Al PLED showed pure blue emission (CIE x=0.144; y=0.129), a high luminescence intensity and notably, up to now, one of the highest ever reported current efficiencies for blue multilayer PLEDs of 9.7 cd/A.

The interplay of all of the presented topics together with the essential selling points of organic electronics, namely cheap, simple and ‘green’ fabrication routes, mechanical flexibility and robustness of the devices, lightweight, etc. clearly show the great prospects of ORS and their evolving applications. There are, without any doubt, severe drawbacks and much work has to be done, however the worldwide vital interest promises a great future of the topic.

Curriculum Vitae

Sebastian Nau was born on 25.09.1984 in Carinthia/Austria where he finished secondary school (School for Higher Technical Education in Villach) with great honors. After one year of civil service he went to Graz to study Technical Physics. He received his bachelor's degree in 2009. In 2010 he joined the group of Prof. E. J. W. List-Kratochvil at the NanoTecCenter Weiz Forschungsgesellschaft and worked on his master project on blue polymer light emitting diodes. He graduated from Graz Univeristy of Technology with honors in 2011. Afterwards he remained in the group of Prof. E. J. W. List-Kratochvil and started working on the PhD project which is presented in this work.

List of Publications[i]

1. T. Qin, W. Wiedemair, **S. Nau**, R. Trattnig, S. Sax, S. Winkler, A. Vollmer, N. Koch, M. Baumgarten, E. J W List, K. Müllen, 'Core, shell, and surface-optimized dendrimers for blue light-emitting diodes' *Journal of the American Chemical Society* 2011**,** *133*, 1301.

2. **S. Nau**, N. Schulte, S. Winkler, J. Frisch, A. Vollmer, N. Koch, S. Sax, E. J. W. List, 'Highly Efficient Color-Stable Deep-Blue Multilayer PLEDs: Preventing PEDOT:PSS-Induced Interface Degradation' *Advanced Materials* 2013, *25*, 4420.

---

[i] Publication number 2, 4, 5 and 6 are included in this work

3. **S. Nau**, R. Trattnig, L. Pevzner, M. Jäger, R. Schlesinger, M. V. Nardi, G. Ligorio, C. Christodoulou, N. Schulte, S. Winkler, J. Frisch, A. Vollmer, M. Baumgarten, S. Sax, N. Koch, K. Müllen, E. J. W. List-Kratochvil, 'All solution processed blue multi-layer light emitting diodes realized by thermal layer stabilization and orthogonal solvent processing' Organic Light Emitting Materials and Devices XVII, Proceedings of SPIE Vol. 8829 (SPIE, Bellingham, WA 2013), 88290Z.

4. **S. Nau**, S. Sax, E. J. W. List-Kratochvil, 'Unravelling the Nature of Unipolar Resistive Switching in Organic Devices by utilizing the Photovoltaic Effect' *Advanced Materials* 2014, *26*, 2508.

5. **S. Nau**, C. Wolf, K. Popovic, A. Blümel, F. Santoni, A. Gagliardi, A. di Carlo, S. Sax, E. J. W. List-Kratochvil, 'Inkjet-printed Resistive Switching Memory based on Organic Dielectric Materials: From Single Elements to Array Technology', submitted for publication.

6. **S. Nau**, C. Wolf, S. Sax, E. J. W. List-Kratochvil, 'Organic Non-Volatile Resistive Photo-Switches for Flexible Image Detector Arrays', submitted for publication.

7. C. Wolf, **S. Nau**, S. Sax, Y. Busby, J.-J. Pireaux, E. J.W. List-Kratochvil, 'Resistive switching based on filaments in metal/PMMA/metal thin film devices', submitted for publication.

8. Y. Busby, **S. Nau**, S. Sax, E. J. W. List-Kratochvil, J. Novak, R. Banerjee, F. Schreiber, J.-J. Pireaux, 'Metal Diffusion and Filament Formation in AlQ3-based Organic Resistive Memories', submitted for publication.

List of Patents

1. R. Dixon, R. Preston, **S. Nau**, C. Wolf, E. J. W. List-Kratochvil, ‚Capacitive Touch Sensitive Board Game based on Dielectric Coupling', US Patent Application.

2. **S. Nau**, S. Sax, Emil J. W. List, 'Speicher-Sensoranordnung mit einem Sensorelement und einem Speicher, Österreichische Patentanmeldung A50442/2013.

Conference Contributions[ii]

Talks

1. **S. Nau**, S. Sax, E. J. W. List, ‘Hybrid Resistive Switching-Based Memory Elements: Fundamentals and Integration Aspects’, 6th Winterschool on organic electronics - Self-Assembly and Hybrid Devices 2012, Planneralm, Austria.

2. **S. Nau**, C. Wolf, S. Sax, E. J. W. List-Kratochvil, ‘The origin of resistive switching in organic electronic devices and evolving applications and opportunities‘, International Conference on Synthetic Metals (ICSM) 2014, Turku, Finland.

3. **S. Nau**, C. Wolf, S. Sax, E. J. W. List-Kratochvil, ‘Resistance Switching in Organic Electronic Devices: Mechanism and Applications‘, International Conference on Electroluminescence and Organic Optoelectronics (ICEL) 2014, Cologne, Germany.

Posters

1. **S. Nau**, S. Sax, E. J. W. List, ‘Hybrid Resistive Switching-Based Memory Elements: Fundamentals and Integration Aspects’, 6th Winterschool on organic electronics - Self-Assembly and Hybrid Devices 2012, Planneralm, Austria.

2. **S. Nau**, S. Sax, E. J. W. List, ‘Hybrid Resistive Switching-Based Memory Elements: Fundamentals and Integration Aspects’, Nano and Photonics 2013, Mauterndorf, Austria.

3. **S. Nau**, S. Sax, E. J. W. List, ‘Shining light on organic memories: Influence of photonic excitation on organic and organic/inorganic hybrid memory devices, MRS Spring Meeting 2013, San Francisco, USA.

[ii] only conference contributions are listed where S. Nau was the presenter.

References

[1] M. Hilbert, P. López, *Science* **2011**, *332*, 60.

[2] G. E. Moore, *Electronics* **1965**, 114.

[3] Y. Sun, H. Y. Yu, N. Singh, N. S. Shen, G. Q. Lo, D. L. Kwong, **2010**, *31*, 390.

[4] J. Kim, A. J. Hong, S. M. Kim, K.-S. Shin, E. B. Song, Y. Hwang, F. Xiu, K. Galatsis, C. O. Chui, R. N. Candler, S. Choi, J.-T. Moon, K. L. Wang, *Nanotechnology* **2011**, *22*, 254006.

[5] M. N. Baibich, J. M. Broto, A. Fert, N. N. van Dau, F. Petroff, P. Eitenne, G. Creuzet, A. Friederich, J. Chazelas, *Phys. Rev. B* **1988**, *61*, 2472.

[6] W. Rainer, Ed., *Nanoelectronics and Information Technology (2nd Edition)*, Wiley-VCH, **2005**.

[7] D. Lencer, M. Salinga, M. Wuttig, *Adv. Mater.* **2011**, *23*, 2030.

[8] M. Wuttig, N. Yamada, *Nat. Mater.* **2007**, *6*, 824.

[9] "Phase-change RAM in Nokia Mobiles," can be found under http://www.theregister.co.uk/2012/12/17/micron_pcm_asha/, **2014**.

[10] "Micron drops phase change materials," can be found under http://www.theregister.co.uk/2014/01/14/phase_change_micron_drops_phase_change_memory_products/, **2014**.

[11] C. Li, W. Fan, B. Lei, D. Zhang, S. Han, T. Tang, X. Liu, Z. Liu, S. Asano, M. Meyyappan, J. Han, C. Zhou, *Appl. Phys. Lett.* **2004**, *84*, 1949.

[12] C. Li, D. Zhang, X. Liu, S. Han, T. Tang, C. Zhou, W. Fan, J. Koehne, J. Han, M. Meyyappan, a. M. Rawlett, D. W. Price, J. M. Tour, *Appl. Phys. Lett.* **2003**, *82*, 645.

[13] L. Chua, *IEEE Trans. circuit theory* **1971**, *18*, 507.

[14] L. Chua, *Nanotechnology* **2013**, *24*, 383001.

[15] D. B. Strukov, G. S. Snider, D. R. Stewart, R. S. Williams, *Nature* **2008**, *453*, 80.

[16] A. Benoist, S. Blonkowski, S. Jeannot, S. Denorme, J. Damiens, J. Berger, P. Candelier, L. Perniola, R. Martyrs, B. Allard, U. De Lyon, I. Lyon, *Reliab. Phys. Symp.* **2014**, 5.

[17] R. Waser, R. Dittmann, G. Staikov, K. Szot, *Adv. Mater.* **2009**, *21*, 2632.

[18] K. Szot, M. Rogala, W. Speier, Z. Klusek, A. Besmehn, R. Waser, *Nanotechnology* **2011**, *22*, 254001.

[19] K. Szot, W. Speier, G. Bihlmayer, R. Waser, *Nat. Mater.* **2006**, *5*, 312.

[20] M.-J. Lee, C. B. Lee, D. Lee, S. R. Lee, M. Chang, J. H. Hur, Y.-B. Kim, C.-J. Kim, D. H. Seo, S. Seo, U.-I. Chung, I.-K. Yoo, K. Kim, *Nat. Mater.* **2011**, *10*, 625.

[21] R. Waser, M. Aono, *Nat. Mater.* **2007**, *6*, 833.

[22] J.-B. Yun, S. Kim, S. Seo, M.-J. Lee, D.-C. Kim, S.-E. Ahn, Y. Park, J. Kim, H. Shin, *Phys. status solidi – Rapid Res. Lett.* **2007**, *1*, 280.

[23] C. Chiang, C. Fincher, Y. Park, a. Heeger, H. Shirakawa, E. Louis, S. Gau, A. MacDiarmid, *Phys. Rev. Lett.* **1977**, *39*, 1098.

[24] C. W. Tang, S. A. VanSlyke, *Appl. Phys. Lett.* **1987**, *51*, 913.

[25] J. H. Burroughes, D. D. C. Bradley, A. R. Brown, R. N. Marks, K. Mackay, R. H. Friend, P. L. Burns, A. B. Holmes, *Nature* **1990**, *347*, 539.

[26] C. J. Brabec, N. S. Sariciftci, J. C. Hummelen, *Adv. Funct. Mater.* **2001**, *11*, 15.

[27] K.-J. Baeg, M. Binda, D. Natali, M. Caironi, Y.-Y. Noh, *Adv. Mater.* **2013**, *25*, 4267.

[28] B. G. Horowitz, *Adv. Mater.* **1998**, *10*, 365.

[29] Y. Li, *Synth. Met.* **1999**, *99*, 243.

[30] S. Steudel, K. Myny, V. Arkhipov, C. Deibel, S. De Vusser, J. Genoe, P. Heremans, *Nat. Mater.* **2005**, *4*, 597.

[31] B. M. Schaer, F. Nüesch, D. Berner, W. Leo, L. Zuppiroli, *Adv. Mater.* **2001**, *11*, 116.

[32] M. Jørgensen, K. Norrman, F. C. Krebs, *Sol. Energy Mater. Sol. Cells* **2008**, *92*, 686.

[33] H. Aziz, *Science* **1999**, *283*, 1900.

[34] M. Singh, H. M. Haverinen, P. Dhagat, G. E. Jabbour, *Adv. Mater.* **2010**, *22*, 673.

[35] L. F. Pender, R. J. Fleming, *J. Appl. Phys.* **1975**, *46*, 3426.

[36] Y. Segui, *J. Appl. Phys.* **1976**, *47*, 140.

[37] L. P. Ma, J. Liu, Y. Yang, *Appl. Phys. Lett.* **2002**, *80*, 2997.

[38] V. S. Reddy, S. Karak, A. Dhar, *Appl. Phys. Lett.* **2009**, *94*, 173304.

[39] J. Park, W. Nam, S. Seo, Y. Kim, Y. Oh, G. Lee, U. Paik, *Nano Lett.* **2009**, *9*, 1713.

[40] H. Wang, F. Meng, Y. Cai, L. Zheng, Y. Li, Y. Liu, Y. Jiang, X. Wang, X. Chen, *Adv. Mater.* **2013**, *25*, 5498.

[41] K. Nagashima, T. Yanagida, K. Oka, M. Taniguchi, T. Kawai, J.-S. Kim, B. H. Park, *Nano Lett.* **2010**, *10*, 1359.

[42] S. H. Jo, T. Chang, I. Ebong, B. B. Bhadviya, P. Mazumder, W. Lu, *Nano Lett.* **2010**, *10*, 1297.

[43] J. C. Scott, L. D. Bozano, *Adv. Mater.* **2007**, *19*, 1452.

[44] B. B. Cho, T. Kim, S. Song, Y. Ji, M. Jo, H. Hwang, G. Jung, T. Lee, **2010**, 1228.

[45] Y. Ji, D. F. Zeigler, D. S. Lee, H. Choi, A. K.-Y. Jen, H. C. Ko, T.-W. Kim, *Nat. Commun.* **2013**, *4*, 2707.

[46] T.-W. Kim, D. F. Zeigler, O. Acton, H.-L. Yip, H. Ma, A. K.-Y. Jen, *Adv. Mater.* **2012**, *24*, 828.

[47] K. Chan-mo, C. Hyunduck, L. Hyunkoo, L. Changhee, *J. Korean Phys. Soc.* **2011**, *59*, 470.

[48] G. Azzellino, A. Grimoldi, M. Binda, M. Caironi, D. Natali, M. Sampietro, *Adv. Mater.* **2013**, *25*, 6829.

[49] Y. S. Lee, J. H. Park, J. S. Choi, *Opt. Mater.* **2002**, *21*, 433.

[50] J. G. Simmons, R. R. Verderber, *Proc. R. Soc. Lond. A. Math. Phys. Sci.* **1967**, *301*, 77.

[51] L. D. Bozano, B. W. Kean, V. R. Deline, J. R. Salem, J. C. Scott, *Appl. Phys. Lett.* **2004**, *84*, 607.

[52] L. D. Bozano, B. W. Kean, M. Beinhoff, K. R. Carter, P. M. Rice, J. C. Scott, *Adv. Funct. Mater.* **2005**, *15*, 1933.

[53] C. Wu, F. Li, T. Guo, T. W. Kim, *Org. Electron.* **2012**, *13*, 178.

[54] D. I. Son, T. W. Kim, J. H. Shim, J. H. Jung, D. U. Lee, J. M. Lee, W. Il Park, W. K. Choi, *Nano Lett.* **2010**, *10*, 2441.

[55] Y. Ji, M. Choe, B. Cho, S. Song, J. Yoon, H. C. Ko, T. Lee, *Nanotechnology* **2012**, *23*, 105202.

[56] B. Hu, R. Quhe, C. Chen, F. Zhuge, X. Zhu, S. Peng, X. Chen, L. Pan, Y. Wu, W. Zheng, Q. Yan, J. Lu, R. Li, *J. Mater. Chem.* **2012**, *22*, 16422.

[57] A. Sleiman, M. F. Mabrook, R. R. Nejm, A. Ayesh, A. Al Ghaferi, M. C. Petty, D. A. Zeze, *J. Appl. Phys.* **2012**, *112*, 024509.

[58] T. Kondo, S. M. Lee, M. Malicki, B. Domercq, S. R. Marder, B. Kippelen, *Adv. Funct. Mater.* **2008**, *18*, 1112.

[59] B. Jiao, Z. Wu, H. Dong, S. Ning, X. Hou, *J. Phys. D. Appl. Phys.* **2013**, *46*, 445107.

[60] C. W. Lin, T. S. Pan, M. C. Chen, Y. J. Yang, Y. Tai, Y. F. Chen, *Appl. Phys. Lett.* **2011**, *99*, 023303.

[61] K. Onlaor, B. Tunhoo, T. Thiwawong, J. Nukeaw, *Curr. Appl. Phys.* **2012**, *12*, 331.

[62] X. Xia, X. Liu, M. Yi, Q. Fan, L. Wang, Q. Tai, W. Shi, L. Xie, W. Huang, *J. Phys. D. Appl. Phys.* **2012**, *45*, 215101.

[63] B. Cho, S. Song, Y. Ji, T. Lee, *Appl. Phys. Lett.* **2010**, *97*, 063305.

[64] Y. Ji, B. Cho, S. Song, T.-W. Kim, M. Choe, Y. H. Kahng, T. Lee, *Adv. Mater.* **2010**, *22*, 3071.

[65] S. Song, B. Cho, T.-W. Kim, Y. Ji, M. Jo, G. Wang, M. Choe, Y. H. Kahng, H. Hwang, T. Lee, *Adv. Mater.* **2010**, *22*, 5048.

[66] W. Tang, H. Z. Shi, G. Xu, B. S. Ong, Z. D. Popovic, J. C. Deng, J. Zhao, G. H. Rao, *Adv. Mater.* **2005**, *17*, 2307.

[67] H. Lin, Z. Pei, Y. Chan, *IEEE Electron Device Lett.* **2007**, *28*, 569.

[68] J. Ouyang, C.-W. Chu, C. R. Szmanda, L. Ma, Y. Yang, *Nat. Mater.* **2004**, *3*, 918.

[69] R. J. Tseng, J. Huang, J. Ouyang, R. B. Kaner, Y. Yang, *Nano Lett.* **2005**, *5*, 1077.

[70] T. Oyamada, H. Tanaka, K. Matsushige, H. Sasabe, C. Adachi, *Appl. Phys. Lett.* **2003**, *83*, 1252.

[71] C. W. Chu, J. Ouyang, J.-H. Tseng, Y. Yang, *Adv. Mater.* **2005**, *17*, 1440.

[72] Y. Yang, J. Ouyang, L. Ma, R. J.-H. Tseng, C.-W. Chu, *Adv. Funct. Mater.* **2006**, *16*, 1001.

[73] S. Song, J. Jang, Y. Ji, S. Park, T.-W. Kim, Y. Song, M.-H. Yoon, H. C. Ko, G.-Y. Jung, T. Lee, *Org. Electron.* **2013**, *14*, 2087.

[74] M. Xie, K. C. Aw, M. Langlois, W. Gao, *Solid State Commun.* **2012**, *152*, 835.

[75] B. Cho, K. H. Nam, S. Song, Y. Ji, G.-Y. Jung, T. Lee, *Curr. Appl. Phys.* **2012**, *12*, 940.

[76] J.-D. Lee, H.-M. Seung, K.-C. Kwon, J. Park, *Curr. Appl. Phys.* **2011**, *11*, e25.

[77] H. Houili, E. Tutiš, R. Izquierdo, *Org. Electron.* **2010**, *11*, 514.

[78] P. Y. Lai, J. S. Chen, *Appl. Phys. Lett.* **2008**, *93*, 153305.

[79] V. Reddy, S. Karak, S. Ray, A. Dhar, *Org. Electron.* **2009**, *10*, 138.

[80] L. D. Bozano, B. W. Kean, V. R. Deline, J. R. Salem, J. C. Scott, *Appl. Phys. Lett.* **2004**, *84*, 607.

[81] P. Sebastian, F. Lindner, K. Walzer, B. Lüssem, K. Leo, *J. Appl. Phys.* **2011**, *110*, 084508.

[82] H. Pagnia, N. Sotnik, *Phys. Status Solidi* **1988**, *108*, 11.

[83] M. Cölle, M. Büchel, D. M. de Leeuw, *Org. Electron.* **2006**, *7*, 305.

[84] B. Cho, J.-M. Yun, S. Song, Y. Ji, D.-Y. Kim, T. Lee, *Adv. Funct. Mater.* **2011**, *21*, 3976.

[85] C. Pearson, L. Bowen, M.-W. Lee, A. L. Fisher, K. E. Linton, M. R. Bryce, M. C. Petty, *Appl. Phys. Lett.* **2013**, *102*, 213301.

[86] W. L. Kwan, B. Lei, Y. Shao, S. V. Prikhodko, N. Bodzin, Y. Yang, *J. Appl. Phys.* **2009**, *105*, 124516.

[87] T.-W. Kim, H. Choi, S.-H. Oh, M. Jo, G. Wang, B. Cho, D.-Y. Kim, H. Hwang, T. Lee, *Nanotechnology* **2009**, *20*, 025201.

[88] M. L. Wang, J. Zhou, X. D. Gao, B. F. Ding, Z. Shi, X. Y. Sun, X. M. Ding, X. Y. Hou, *Appl. Phys. Lett.* **2007**, *91*, 143511.

[89] S. Gao, F. Zeng, C. Chen, G. Tang, Y. Lin, Z. Zheng, C. Song, F. Pan, *Nanotechnology* **2013**, *24*, 335201.

[90] S. Gao, C. Song, C. Chen, F. Zeng, F. Pan, *J. Phys. Chem. C* **2012**, *116*, 17955.

[91] Y. Chang, Y. Wang, *ACS Appl. Mater. Interfaces* **2014**, *6*, 5413.

[92] Y. T. You, Q. Zeng, Y. Yao, M. L. Wang, B. Wu, Y. He, Y. M. Hu, C. Q. Wu, X. Y. Hou, *Appl. Phys. Lett.* **2012**, *100*, 123304.

[93] A. Laiho, H. S. Majumdar, J. K. Baral, F. Jansson, R. Österbacka, O. Ikkala, *Appl. Phys. Lett.* **2008**, *93*, 203309.

[94] Y. T. You, M. L. Wang, H. N. Xuxie, B. Wu, Z. Y. Sun, X. Y. Hou, *Appl. Phys. Lett.* **2010**, *97*, 233301.

[95] B. Lei, W. L. Kwan, Y. Shao, Y. Yang, *Org. Electron.* **2009**, *10*, 1048.

[96] A. Bandyopadhyay, A. J. Pal, *Appl. Phys. Lett.* **2004**, *84*, 999.

[97] S. Karthaü er, B. Lüssem, M. Weides, M. Alba, A. Besmehn, R. Oligschlaeger, R. Waser, *J. Appl. Phys.* **2006**, *100*, 094504.

[98] S. L. Lim, Q. Ling, E. Yeow, H. Teo, C. X. Zhu, D. Siu, H. Chan, E. Kang, K. G. Neoh, N. Uni, K. Ridge, *Chem. Mater.* **2007**, 5148.

[99] E. Y. H. Teo, Q. D. Ling, Y. Song, Y. P. Tan, W. Wang, E. T. Kang, D. S. H. Chan, C. Zhu, *Org. Electron.* **2006**, *7*, 173.

[100] J. Ouyang, C.-W. Chu, C. R. Szmanda, L. Ma, Y. Yang, *Nat. Mater.* **2004**, *3*, 918.

[101] V. Reddy, S. Karak, S. Ray, A. Dhar, *Org. Electron.* **2009**, *10*, 138.

[102] S. Gao, C. Song, C. Chen, F. Zeng, F. Pan, *Appl. Phys. Lett.* **2013**, *102*, 141606.

[103] B. Ghosh, A. J. Pal, *J. Phys. Chem. C* **2009**, *113*, 18391.

[104] G. G. Malliaras, J. R. Salem, P. J. Brock, J. C. Scott, *J. Appl. Phys.* **1998**, *84*, 1583.

[105] S. Dongaonkar, J. D. Servaites, G. M. Ford, S. Loser, J. Moore, R. M. Gelfand, H. Mohseni, H. W. Hillhouse, R. Agrawal, M. A. Ratner, T. J. Marks, M. S. Lundstrom, M. a. Alam, *J. Appl. Phys.* **2010**, *108*, 124509.

[106] O. Breitenstein, *Proc. 17th NREL Work. Cryst. Silicon Sol. Cells Modul. Mater. Process.* **2007**, *Vail, USA*, 61.

[107] B. Qi, J. Wang, *Phys. Chem. Chem. Phys.* **2013**, *15*, 8972.

[108] R. Steim, S. A. Choulis, P. Schilinsky, U. Lemmer, C. J. Brabec, *Appl. Phys. Lett.* **2009**, *94*, 043304.

[109] H. Hoppe, J. Bachmann, B. Muhsin, K.-H. Drüe, I. Riedel, G. Gobsch, C. Buerhop-Lutz, C. J. Brabec, V. Dyakonov, *J. Appl. Phys.* **2010**, *107*, 014505.

[110] S. van Reenen, P. Matyba, A. Dzwilewski, R. A. J. Janssen, L. Edman, M. Kemerink, *J. Am. Chem. Soc.* **2010**, *132*, 13776.

[111] H. Sirringhaus, *Science* **2000**, *290*, 2123.

[112] H. Yan, Z. Chen, Y. Zheng, C. Newman, J. R. Quinn, F. Dötz, M. Kastler, A. Facchetti, *Nature* **2009**, *457*, 679.

[113] M. Böberl, M. V. Kovalenko, S. Gamerith, E. J. W. List, W. Heiss, *Adv. Mater.* **2007**, *19*, 3574.

[114] G. Mauthner, K. Landfester, A. Köck, H. Brückl, M. Kast, C. Stepper, E. J. W. List, *Org. Electron.* **2008**, *9*, 164.

[115] H. Gorter, M. J. J. Coenen, M. W. L. Slaats, M. Ren, W. Lu, C. J. Kuijpers, W. a. Groen, *Thin Solid Films* **2013**, *532*, 11.

[116] C. N. Hoth, P. Schilinsky, S. A. Choulis, C. J. Brabec, *Nano Lett.* **2008**, *8*, 2806.

[117] T. N. Ng, B. Russo, B. Krusor, R. Kist, A. C. Arias, *Org. Electron.* **2011**, *12*, 2012.

[118] A. C. Dürr, F. Schreiber, M. Kelsch, H. D. Carstanjen, H. Dosch, O. H. Seeck, *J. Appl. Phys.* **2003**, *93*, 5201.

[119] M. Punke, S. Valouch, S. Member, S. W. Kettlitz, M. Gerken, U. Lemmer, *J. Light. Technol.* **2008**, *26*, 816.

[120] J. W. Kingsley, A. J. Pearson, L. Harris, S. J. Weston, D. G. Lidzey, *Org. Electron.* **2009**, *10*, 1170.

[121] G. H. Gelinck, A. Kumar, D. Moet, J.-L. van der Steen, U. Shafique, P. E. Malinowski, K. Myny, B. P. Rand, M. Simon, W. Rütten, A. Douglas, J. Jorritsma, P. Heremans, R. Andriessen, *Org. Electron.* **2013**, *14*, 2602.

[122] T. N. Ng, W. S. Wong, M. L. Chabinyc, S. Sambandan, R. A. Street, *Appl. Phys. Lett.* **2008**, *92*, 213303.

[123] S. Aihara, H. Seo, M. Namba, T. Watabe, H. Ohtake, M. Kubota, N. Egami, T. Hiramatsu, T. Matsuda, M. Furuta, H. Nitta, T. Hirao, *IEEE Trans. Electron Devices* **2009**, *56*, 2570.

[124] T. Rauch, S. F. Tedde, J. Fürst, M. V Kovalenko, M. Bo, U. Lemmer, W. Heiss, O. Hayden, *Nat. Photonics* **2009**, *3*, 332.

[125] B. Lamprecht, E. Kraker, M. Sagmeister, S. Köstler, N. Galler, H. Ditlbacher, B. Ungerböck, T. Abel, T. Mayr, *Phys. status solidi - Rapid Res. Lett.* **2011**, *5*, 344.

[126] D. Ghezzi, M. R. Antognazza, M. Dal Maschio, E. Lanzarini, F. Benfenati, G. Lanzani, *Nat. Commun.* **2011**, *2*, 166.

[127] N. Martino, D. Ghezzi, F. Benfenati, G. Lanzani, M. R. Antognazza, *J. Mater. Chem. B* **2013**, *1*, 3768.

[128] X. Xu, M. Davanco, X. Qi, S. R. Forrest, *Org. Electron.* **2008**, *9*, 1122.

[129] X. Tong, S. R. Forrest, *Org. Electron.* **2011**, *12*, 1822.

[130] S. Tedde, E. S. Zaus, J. Fürst, D. Henseler, P. Lugli, *IEEE Electron Device Lett.* **2007**, *28*, 893.

[131] M. T. Dang, L. Hirsch, G. Wantz, *Adv. Mater.* **2011**, *23*, 3597.

[132] S. Nau, S. Sax, E. J. W. List-Kratochvil, *Adv. Mater.* **2014**, *26*, 2508.

[133] M. Eritt, C. May, K. Leo, M. Toerker, C. Radehaus, *Thin Solid Films* **2010**, *518*, 3042.

[134] A. R. Duggal, C. M. Heller, J. J. Shiang, J. Liu, L. N. Lewis, *J. Disp. Technol.* **2007**, *3*, 184.

[135] R. Trattnig, T. M. Figueira-Duarte, D. Lorbach, W. Wiedemair, S. Sax, S. Winkler, A. Vollmer, N. Koch, M. Manca, M. A. Loi, M. Baumgarten, E. J. W. List, K. Müllen, *Opt. Express* **2011**, *19*, A1281.

[136] M. Jansen, H. P. Baldus, U. S. Patent, R. Jaschek, C. Russel, J. N. Solids, B. J. Grimme, M. Kreyenschmidt, F. Uckert, K. Miillen, U. Scherf, *Adv. Mater.* **1995**, *292*, 292.

[137] D. Neher, *Macromol. Rapid Commun.* **2001**, *22*, 1365.

[138] B. U. Scherf, E. J. W. List, *Adv. Mater.* **2002**, *14*, 477.

[139] S. Setayesh, D. Marsitzky, K. Mu, *Macromolecules* **2000**, *33*, 2016.

[140] B. A. C. Grimsdale, P. Lecl, R. Lazzaroni, J. D. Mackenzie, C. Murphy, S. Setayesh, C. Silva, R. H. Friend, K. Müllen, *Adv. Funct. Mater.* **2002**, *12*, 729.

[141] J. Jacob, J. Zhang, A. C. Grimsdale, K. Müllen, M. Gaal, E. J. W. List, *Macromolecules* **2003**, *36*, 8240.

[142] J. Jacob, S. Sax, T. Piok, E. J. W. List, A. C. Grimsdale, K. Müllen, *J. Am. Chem. Soc.* **2004**, *126*, 6987.

[143] J. Morgado, R. H. Friend, F. Cacialli, *Appl. Phys. Lett.* **2002**, *80*, 2436.

[144] X. H. Yang, F. Jaiser, B. Stiller, D. Neher, F. Galbrecht, U. Scherf, *Adv. Funct. Mater.* **2006**, *16*, 2156.

[145] C. Gu, H. Liu, D. Hu, W. Zhang, Y. Lv, P. Lu, D. Lu, Y. Ma, *Macromol. Rapid Commun.* **2011**, *32*, 1014.

[146] B. Zhang, W. Li, J. Yang, Y. Fu, Z. Xie, S. Zhang, L. Wang, *J. Phys. Chem. C* **2009**, *113*, 7898.

[147] M. Gross, D. Muller, H. Nothofer, U. Scherf, D. Neher, C. Brauchle, K. Meerholz, *Nature* **2000**, *405*, 661.

[148] T.-W. Lee, T. Noh, B.-K. Choi, M.-S. Kim, D. W. Shin, J. Kido, *Appl. Phys. Lett.* **2008**, *92*, 043301.

[149] S.-R. Tseng, H.-F. Meng, K.-C. Lee, S.-F. Horng, *Appl. Phys. Lett.* **2008**, *93*, 153308.

[150] N. C. Greenham, S. C. Moratti, D. D. C. Bradley, R. H. Friend, A. B. Holmes, *Nature* **1993**, *365*, 628.

[151] D. C. Müller, A. Falcou, N. Reckefuss, M. Rojahn, V. Wiederhirn, P. Rudati, H. Frohne, O. Nuyken, H. Becker, K. Meerholz, *Nature* **2003**, *421*, 829.

[152] X. Jiang, S. Liu, M. S. Liu, H. Ma, A. K.-Y. Jen, *Appl. Phys. Lett.* **2000**, *76*, 2985.

[153] X. Gong, D. Moses, A. J. Heeger, S. Liu, A. K.-Y. Jen, *Appl. Phys. Lett.* **2003**, *83*, 183.

[154] S. Sax, N. Rugen-Penkalla, A. Neuhold, S. Schuh, E. Zojer, E. J. W. List, K. Müllen, *Adv. Mater.* **2010**, *22*, 2087.

[155] W. Ma, P. K. Iyer, X. Gong, B. Liu, D. Moses, G. C. Bazan, A. J. Heeger, *Adv. Mater.* **2005**, *17*, 274.

[156] A. Köhnen, M. Irion, M. C. Gather, N. Rehmann, P. Zacharias, K. Meerholz, *J. Mater. Chem.* **2010**, *20*, 3301.

[157] Y.-H. Niu, M. S. Liu, J.-W. Ka, J. Bardeker, M. T. Zin, R. Schofield, Y. Chi, a. K.-Y. Jen, *Adv. Mater.* **2007**, *19*, 300.

[158] Y.-H. Niu, M. S. Liu, J.-W. Ka, A. K.-Y. Jen, *Appl. Phys. Lett.* **2006**, *88*, 093505.

[159] N. Koch, *Chemphyschem* **2007**, *8*, 1438.

[160] B. L. Groenendaal, F. Jonas, D. Freitag, H. Pielartzik, J. R. Reynolds, *Adv. Mater.* **2000**, *12*, 481.

[161] B. G. Heywang, F. Jonas, *Adv. Mater.* **1992**, *4*, 116.

[162] P. Ho, J. Kim, J. Burroughes, H. Becker, S. Li, T. Brown, F. Cacialli, R. Friend, *Nature* **2000**, *404*, 481.

[163] Q. Xu, J. Ouyang, Y. Yang, T. Ito, J. Kido, *Appl. Phys. Lett.* **2003**, *83*, 4695.

[164] N. Koch, A. Elschner, J. P. Rabe, R. L. Johnson, *Adv. Mater.* **2005**, *17*, 330.

[165] A. J. A. B. Seeley, R. H. Friend, J.-S. Kim, J. H. Burroughes, *J. Appl. Phys.* **2004**, *96*, 7643.

[166] D. Poplavskyy, J. Nelson, D. D. C. Bradley, *Appl. Phys. Lett.* **2003**, *83*, 707.

[167] P. Brewer, J. Huang, P. Lane, A. deMello, D. Bradley, J. deMello, *Phys. Rev. B* **2006**, *74*, 115202.

[168] P. Tehrani, A. Kanciurzewska, X. Crispin, N. Robinson, M. Fahlman, M. Berggren, *Solid State Ionics* **2007**, *177*, 3521.

[169] S. Wu, S. Han, Y. Zheng, H. Zheng, N. Liu, L. Wang, Y. Cao, J. Wang, *Org. Electron.* **2011**, *12*, 504.

[170] J.-S. Kim, R. H. Friend, I. Grizzi, J. H. Burroughes, *Appl. Phys. Lett.* **2005**, *87*, 023506.

[171] R.-Q. Png, P.-J. Chia, S. Sivaramakrishnan, L.-Y. Wong, M. Zhou, L.-L. Chua, P. K.-H. Ho, *Appl. Phys. Lett.* **2007**, *91*, 013511.

[172] A. van Dijken, A. Perro, E. A. Meulenkamp, K. Brunner, *Org. Electron.* **2003**, *4*, 131.

[173] L. C. Palilis, D. G. Lidzey, M. Redecker, D. D. C. Bradley, M. Inbasekaran, **2000**, 159.

[174] S. Kappaun, S. Horner, A.-M. Kelterer, K. Waich, F. Grasse, M. Graf, L. Romaner, F. Niedermair, K. Müllen, A. C. Grimsdale, R. Saf, E. J. W. List, E. Zojer, C. Slugovc, *Macromol. Chem. Phys.* **2008**, *209*, 2122.

[175] C.-Y. Chang, F.-Y. Tsai, S.-J. Jhuo, M.-J. Chen, *Org. Electron.* **2008**, *9*, 667.

[176] S. Kappaun, H. Scheiber, R. Trattnig, E. Zojer, E. J. W. List, C. Slugovc, *Chem. Commun.* **2008**, 5170.

[177] W. C. H. Choy, J. H. Niu, X.-W. Chen, W. L. Li, P. C. Chui, *Appl. Phys. A* **2007**, *89*, 667.

[178] S. Gamerith, H.-G. Nothofer, U. Scherf, E. J. W. List, *Jpn. J. Appl. Phys.* **2004**, *43*, L891.

[179] S. Lee, D. Ko, C. Chung, S. M. Cho, **2002**, *128*, 51.

[180] J. Huang, Z. Xu, Y. Yang, *Adv. Funct. Mater.* **2007**, *17*, 1966.

[181] K. Asadi, P. W. M. Blom, D. M. de Leeuw, *Adv. Mater.* **2011**, *23*, 865.

[182] L. Ma, J. Liu, S. Pyo, Y. Yang, *Appl. Phys. Lett.* **2002**, *80*, 362.

[183] K. S. Yook, S. O. Jeon, C. W. Joo, J. Y. Lee, *J. Ind. Eng. Chem.* **2009**, *15*, 328.

[184] S. H. Kim, K. S. Yook, J. Y. Lee, J. Jang, *Appl. Phys. Lett.* **2008**, *93*, 053306.

[185] S. H. Kim, K. S. Yook, J. Jang, J. Y. Lee, *Synth. Met.* **2008**, *158*, 861.

[186] K. S. Yook, S. O. Jeon, O. Y. Kim, J. Y. Lee, *Electrochem. Solid-State Lett.* **2011**, *14*, J31.

[187] C.-W. Chang, W.-C. Tan, M.-L. Lu, T.-C. Pan, Y.-J. Yang, Y.-F. Chen, *Sci. Rep.* **2014**, *4*, 5121.

[188] J. Huang, G. Li, E. Wu, Q. Xu, Y. Yang, *Adv. Mater.* **2006**, *18*, 114.

[189] B. Hu, F. E. Karasz, *J. Appl. Phys.* **2003**, *93*, 1995.

[190] H. T. Nicolai, A. Hof, P. W. M. Blom, *Adv. Funct. Mater.* **2012**, *22*, 2040.

[191] S. Sax, E. Fisslthaler, S. Kappaun, C. Konrad, K. Waich, T. Mayr, C. Slugovc, I. Klimant, E. J. W. List, *Adv. Mater.* **2009**, *21*, 3483.

Appendix

Two published papers (incl. Supporting information) which are included in this work can be found in this Appendix:

- **S. Nau**, N. Schulte, S. Winkler, J. Frisch, A. Vollmer, N. Koch, S. Sax, E. J. W. List, ‘Highly Efficient Color-Stable Deep-Blue Multilayer PLEDs: Preventing PEDOT:PSS-Induced Interface Degradation.’ *Advanced Materials* 2013, *25*, 4420.

- **S. Nau**, S. Sax, E. J. W. List-Kratochvil, ‘Unravelling the Nature of Unipolar Resistive Switching in Organic Devices by utilizing the Photovoltaic Effect‘ *Advanced Materials* 2014, *26*, 2508.

ADVANCED MATERIALS
www.advmat.de

Materials Views
www.MaterialsViews.com

Highly Efficient Color-Stable Deep-Blue Multilayer PLEDs: Preventing PEDOT:PSS-Induced Interface Degradation

Sebastian Nau, Niels Schulte, Stefanie Winkler, Johannes Frisch, Antje Vollmer, Norbert Koch, Stefan Sax, and Emil J. W. List**

Since the report of the first small-molecule-based thin-film organic light-emitting diode (OLED)[1] and the first polymer light-emitting diode (PLED),[2] remarkable efforts of the research community and a resilient industrial contribution have led to a number of commercial OLED-based products; they have attracted attention beyond niche markets and have large-area applications in the field of flat-panel displays and lighting devices.[3] While fast improvements in the chemical stability of the active materials and the reliability of the devices have led to well-established red and green[4] fluorescent and phosphorescent emitters (based on both small molecules and conjugated polymers), there remains a quest for improved stability in materials emitting in the blue spectral range.

Among others, poly(para-phenylene) (PPP)- and poly(pyrene)-type[5] polymers are rather promising as blue-emitting conjugated polymers for stable PLED applications and therefore of particular interest. In addition to a well-defined chemistry, PPP-type polymers allow for effective emission-color tuning from UV-blue to blue emission by increasing the number of aryl–aryl bridges – stretching from PPP[6] with a dominating UV emission, over poly(fluorene)[7] (emitting in the UV-blue) and poly(indenofluorene)[8] (PIF) (emitting further in the visible) to poly(pentaphenylene),[9] yielding a deep blue emission perfectly matching the sensitivity of the human eye for blue.

Aside from the chemical stability of the particular emitter material and a high radiative quantum yield of the emissive unit, efficient and bright PLED devices with long lifetimes require a balanced charge carrier injection and an effective and balanced transport of electrons and holes towards the electro-optical active layer. Moreover a pinning of the emission zone to the center of the device, using heterojunctions with an appropriate type-II band level offset to avoid quenching at either of the electrode interfaces, has also been found to be rather favorable.[10] Modifications of the poly(3,4-ethylenedioxythiophene):poly(styrenesulphonic acid) (PEDOT:PSS) surface, auxiliary injection layers,[11] doped interface regions,[12] and multiple tandem structures including interconnecting layers[13] have been used to enhance and balance charge injection/transport as well as exciton formation in the devices.

Irrespective of the individual preparation techniques, the crucial challenge of solution-processed multilayer PLEDs is how to not redissolve a preceding polymer layer by the solvent used to deposit a subsequent polymer layer. Different approaches have been suggested, ranging from liquid buffer layers between the individual polymer layers[14] to in situ converted or crosslinked polymer layers[15] to the application of orthogonal solvent systems.[16] Alternatively, the stability against the resolubilization of a polymer film can be significantly increased by a thermal bake-out process.[17]

Independent of the specific device structure, the majority of today's polymer-based light-emitting diodes comprise a PEDOT:PSS layer on top of the transparent bottom electrode due to its reasonable workfunction (4.8 to 5.6 eV), high conductivity range ($\approx 10^{-5}$–10^{2} S/cm), and good hole injection ability.[18] Since the surface moiety of a PEDOT:PSS layer is sensitive to the preparation/storage conditions, for example, vacuum-annealed samples tend to form PSS-rich surfaces while water vapor supports the decrease of the PSS concentration on top of the layer,[19] the overall performance of a PLED can be considerably altered. In particular, enhanced concentrations of the insulating PSS moieties are considered to be responsible for electron blocking at the interface.[20] In the case of using desired low-workfunction cathode materials, electrons – representing the charge carrier majority – tend to accumulate at the PSS-rich phase increasing hole injection because of strong electric fields in the anode region, leading to an improved charge carrier balance and higher device efficiencies.[21]

Even though PEDOT:PSS is widely used for PLEDs due to its beneficial properties, it suffers from many drawbacks such as its acidic character,[22] exciton quenching,[23] field-induced migration of PEDOT-cations,[24] and the possible chemical degradation of the light-emitting polymer.[25] These problems can be avoided or at least minimized by integrating an appropriate acid-stable interlayer between the organic–PEDOT:PSS interface.

S. Nau, Dr. S. Sax, Prof. E. J. W. List
NanoTecCenter Weiz Forschungsgesellschaft mbH
Franz-Pichler Str. 32, A-8160 Weiz, Austria
E-mail: Stefan.Sax@ntc-weiz.at; E.List@tugraz.at
Dr. N. Schulte
Merck KGaA
Frankfurter Str. 250, D-64293 Darmstadt, Germany
S. Winkler, Dr. A. Vollmer
Helmholtz Zentrum Berlin für Materialien und Energie GmbH
Elektronenspeicherring BESSY II, Albert-Einstein-Str. 15
D-12489 Berlin, Germany
J. Frisch, Prof. N. Koch
Institut für Physik
Humboldt-Universität zu Berlin
Brook-Taylor-Str. 6, D-12489 Berlin, Germany
Prof. E. J. W. List
Institute of Solid State Physics
Graz University of Technology
Petersgasse 16, A-8010 Graz, Austria

DOI: 10.1002/adma.201300832

Figure 1. Chemical structures of the individual copolymer building blocks: A) 9,9,12,12-tetraorganyl-6,12-dihydroindeno[1,2-*b*]fluorene; B) (*E*)-4-organyl-*N*-phenyl-*N*-(4-styrylphenyl)aniline; C) 9,10-diorganyl-phenanthrene; D) N^1,N^4-bis(4-organylphenyl)-N^1,N^4-diphenylbenzene-1,4-diamine; and E) 4-organyl-*N*,*N*-diphenylaniline; R_n where *n* is 1–10 represents organyl groups. **CP-AE** consists of component **A** and **E** at a ratio of 50:50; **CP-ABCD** consists of component **A**, **B**, **C**, and **D** at an A:B:C:D ratio of 46:2:50:2; and **CP-ACD** consists of component **A**, **C**, and **D** at an A:C:D ratio of 48:50:2.

We report here on the electro-optical properties of novel light-emitting copolymers (CPs, designated as **CP-AE**, **CP-ABCD**, **CP-ACD**) comprising different light-emitting and transport-supporting building blocks (**Figure 1**). The chemical degradation of the emissive units assigned to the acidity of PEDOT:PSS will be addressed, and a route to fabricate highly efficient and color-stable multilayer PLEDs will be presented.

The molecular design of the copolymers was optimized with particular emphasis on: a) efficient exciton formation, b) light emission in an energy region with reasonable human-eye sensitivity for the blue color, c) enhanced charge carrier transport properties for electrons and holes, d) appropriate energy level positions facilitating both charge injection and blocking in a polymer heterostructure, and e) suppression of the PEDOT:PSS-induced spectral degradation of the emissive units. The alternating copolymer **CP-AE** is used as the hole-transport and injection layer; it contains component **A** (indenofluorene) and **E** (triphenylamine) at an A:E ratio of 50:50. Copolymer **CP-ABCD**, comprising an indenofluorene unit (**A**), an (*E*)-4-organyl-*N*-phenyl-*N*-(4-styrylphenyl)aniline emissive unit (**B**), electron-transport-supporting phenanthrene (**C**), and hole-transport-supporting amine (**D**) units at an A:B:C:D ratio of 46:2:50:2, is used as the emissive layer. Additionally the copolymer **CP-ACD** (A:C:D = 48:2:50) was investigated in place of **CP-ABCD** for comparison, as the two differ only by the additional emissive unit **B**.

Figure 2a–c show the thin-film absorbance and photoluminescence (PL) spectra of the three utilized CPs as well as the PL film spectra of the CP layers deposited on PEDOT:PSS and the CP films mixed with trifluoroacetic acid (TFA) in order to demonstrate the possibility of chemical degradation of the emissive units of the copolymers.

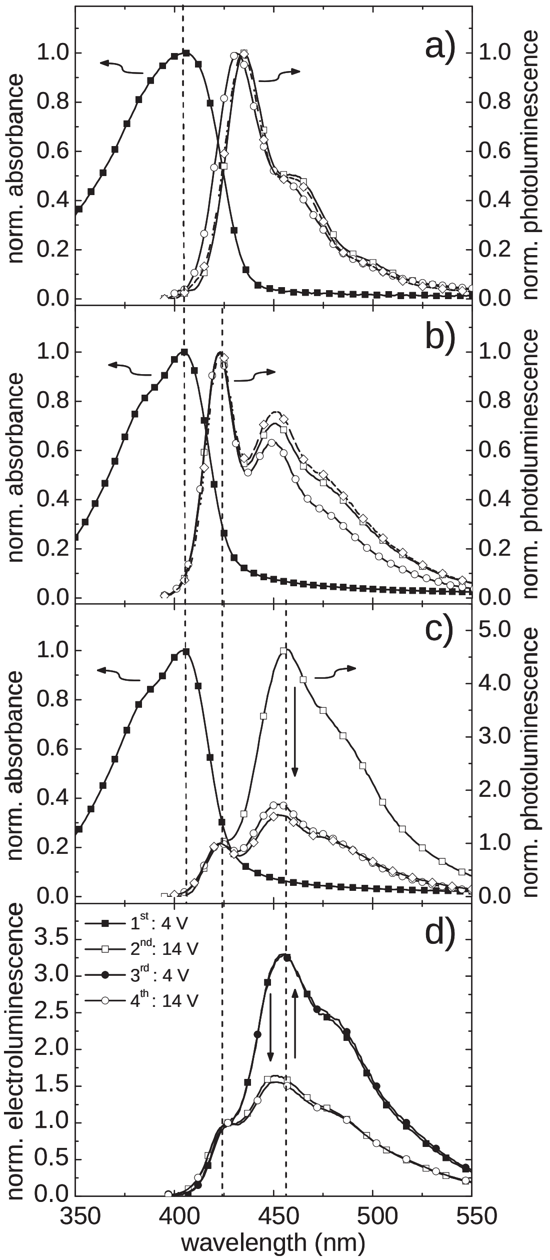

Figure 2. Absorbance and photoluminescence spectra of a) **CP-AE**, b) **CP-ACD**, and c) **CP-ABCD**: thin-film absorbance spectra (filled squares); thin-film PL spectra (open squares); thin-film PL spectra of a PEDOT:PSS/CP double layer (open circles); thin-film PL spectra of a CP–(trifluoroacetic acid) blend (open diamonds). d) Normalized electroluminescence emission spectra of an ITO/PEDOT:PSS/**CP-ABCD** (60 nm)/Ca (10 nm)/Al (100 nm) device biased at 4 V (first, full squares; third, full circles) or at 14 V (second, open squares; fourth, open circles).

As depicted in Figure 2a, **CP-AE** shows an unstructured absorption spectrum with its maximum at 406 nm. The emission maximum of the **CP-AE** thin-film PL spectrum was found at 435 nm with the first vibronic peak at 461 nm. Except for a bathochromic shift of ca. 10 meV, which is attributed to the high concentration of copolymerized-amine-based hole transport units,[26] both the emission and absorption spectra are prototypical for PIF.[8]

Figure 2b shows the absorption spectrum of **CP-ACD** with its maximum located at 404 nm and a slight shoulder at 385 nm. The thin-film emission maxima, found at around 423 and 451 nm, are assigned to the π–π^* transition and the first vibronic progression, respectively, of the copolymer. As it becomes evident in Figure 2c, the absorption spectrum of **CP-ABCD** does not show any significant modifications compared to **CP-ACD** because the additional emissive component **B** is only present at a low concentration. Nevertheless, the PL emission spectrum is seriously influenced by the introduced co-emitter **B**; the maximum of the spectrum is shifted towards longer wavelengths by ca. 20 meV to 457 nm with a shoulder at 480 nm. This significant shift of the PL emission spectrum as well as the strong reduction of the **CP-ACD** emission peak at 423 nm clearly demonstrates the distinct impact of component **B**, resulting in a perfect overlay with the sensitivity of the human eye.

It is known from literature that polymers containing pyridine units,[27] vinylene units[28] or distinct end-chain groups[29] may be prone to degrade in an acidic environment. Therefore all copolymers have been tested for the possible influence of PEDOT:PSS to the emissive spectrum, and in particular that of the PSS-rich phase at the interface. As depicted in Figure 2c, the thin-film emission spectrum of **CP-ABCD** on a glass substrate is considerably different from the emission of the copolymer on PEDOT:PSS, where a reduction of the emission peak at 457 nm by more than 60% was found. To clarify the acidic influence on the emission, **CP-ABCD** was also blended with TFA; when the PL of the thin films was measured, exactly the same reduction in the PL emission at 457 nm was observed. Consistently with the spectra obtained from PEDOT:PSS/copolymer double-layer systems, where essentially no alteration for **CP-ACD** and **CP-AE** on PEDOT:PSS was found, the blends of TFA:**CP-ACD** (Figure 2b and Supporting Information, Figure S1) and TFA:**CP-AE** (Figure 2a; Figure S1, Supporting Information) did not exhibit any significant changes in the PL spectrum. Comparing the chemical structures of **CP-ACD** and **CP-ABCD**, the observed spectral change can be attributed to an electrophilic addition of the acid with the nucleophilic carbon double bond of the vinylene units[28] (component **B**), leading to a strong quenching of the PL at this copolymer site.

In addition to PL measurements, the influence of PEDOT:PSS on **CP-ABCD** was investigated in a PLED device structure (indium tin oxide (ITO)/PEDOT:PSS/**CP-ABCD**/Ca/Al PLED). As depicted in Figure 2d the electroluminescence (EL) spectrum can be reversibly changed as a function of the bias voltage with respect to the emission peak at 457 nm. At 4 V, the EL spectrum mostly equals the corresponding **CP-ABCD** single-layer PL spectrum (Figure 2c, open squares) with a maximum at 455 nm and two additional features at 426 and 482 nm. Increasing the bias voltage to 14 V leads to a reduction of the maximum emission peak at 457 nm by more than 50%, comparable to the change found in the PL spectrum from the PEDOT:PSS/**CP-ABCD** double layer or the TFA:**CP-ABCD** films (Figure 2c, open circles; open diamonds). Since this behavior is shown to be fully reversible, general device degradation can be excluded, and the change in the EL spectrum can be assigned to a voltage-dependent movement of the recombination zone[30] forwards and backwards with respect to the PSS/**CP-ABCD** interface with degraded vinylene units due to the interaction with PSS.

While tentatively discussed in literature,[23,25] these results clearly demonstrates that the acidity of the PEDOT:PSS layer can distinctively alter the device performance/stability due to exciton quenching at the emissive units at the interface, accompanied by changes in the overall spectral emission characteristics and a reduction of the device stability. Particularly when using low-workfunction cathode materials, where the charge carrier recombination zone tends to shift towards the anode, the chemical stability of the emissive units close to the interface with PEDOT:PSS is of crucial importance.

In order to impede interactions at the PEDOT:PSS/**CP-ABCD** interface in PLEDs and to improve hole transport towards the **CP-ABCD** layer, an additional hole transport layer using **CP-AE** was integrated. To avoid resolubilization during device preparation, the **CP-AE** layer was stabilized by thermal curing at 200 °C for 1 h in argon. This bake-out did not result in any significant change of the absorbance or of the PL spectrum (Figure S2, Supporting Information). Atomic force microscopy investigations reveal that **CP-AE** films cured at 200 °C did not show any noteworthy decrease in film thickness after being washed with pure solvent, whereas films baked at 70 °C can still be completely removed.

Compared to devices without **CP-AE**, ITO/PEDOT:PSS/**CP-AE**/**CP-ABCD**/Ca/Al devices did not show any distinct bias-voltage-dependent change in the EL emission spectrum (Figure S3, Supporting Information), but a significant device efficiency enhancement from 1 to 1.9 cd A^{-1} at 1000 cd m^{-2} (**Table 1**).

Aside from the enhanced hole transport properties of **CP-AE**, this significant performance enhancement is a result of an optimal type-II band alignment at the **CP-AE**/**CP-ABCD** interface as determined by ultraviolet photoelectron spectroscopy (UPS) (**Figure 3**a; Figure S4, Supporting Information). Therefore valence-band-region spectra and the secondary electron cut-off was measured after each layer-deposition step. **CP-AE**'s and **CP-ABCD**'s low-binding-energy onsets are 0.6 and 0.9 eV below the Fermi level (E_F), respectively; this energy offset corresponds to the hole-injection barrier from PEDOT:PSS. Together with the workfunction determined from the secondary

Table 1. Electro-optical properties of single- and multilayer devices with different electrode configurations.

PLED configuration	Maximum efficiency [cd A^{-1}]	Efficiency @1000 cd m^{-2} [cd A^{-1}]	CIE1931 color space coordinates
ITO/PEDOT:PSS/**CP-AE**/**CP-ACD**/Cs_2CO_3/Al	7.3	2.8	$x = 0.148$; $y = 0.149$
ITO/PEDOT:PSS/**CP-ABCD**/Ca/Al	1.0	1.0	$x = 0.144$; $y = 0.125$
ITO/PEDOT:PSS/**CP-AE**/**CP-ABCD**/Ca/Al	2.1	1.9	$x = 0.144$; $y = 0.125$
ITO/PEDOT:PSS/**CP-AE**/**CP-ABCD**/Cs_2CO_3/Al	9.7	3.7	$x = 0.144$; $y = 0.129$

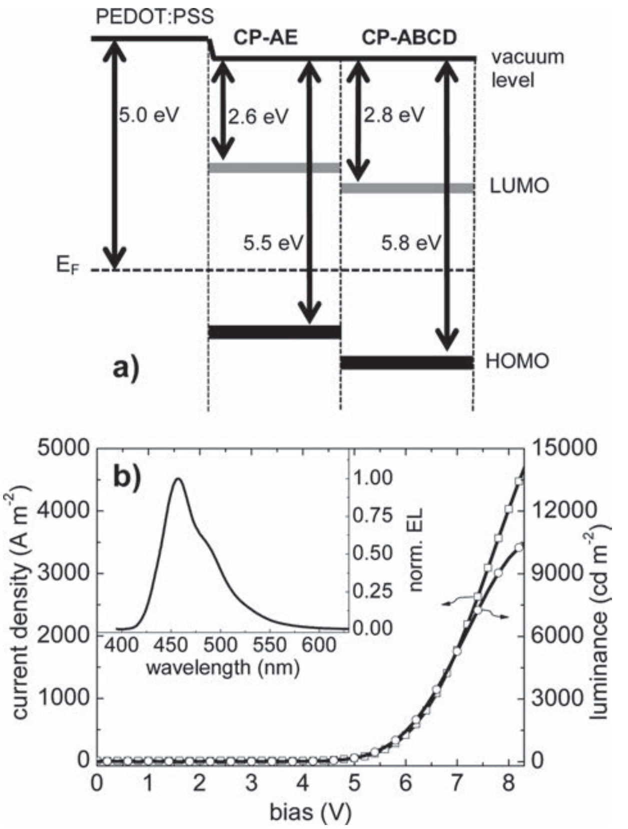

Figure 3. a) Schematic energy level diagram of the PEDOT:PSS/**CP-AE/CP-ABCD** multilayer structure obtained from layer-by-layer UPS investigation. b) Current density (open squares) and luminance (open circles) as a function of the bias voltage in an ITO/PEDOT:PSS (60 nm)/**CP-AE** (20 nm)/**CP-ABCD** (60 nm)/Cs_2CO_3 (0.15 nm)/Al (100 nm) device. The inset shows the normalized EL spectrum of the device with CIE color space coordinates of x = 0.144 and y = 0.129. (HOMO indicates the highest occupied molecular orbital.)

electron cut-off, the corresponding ionization energy can be found at 5.5 and 5.8 eV for **CP-AE** and **CP-ABCD**, respectively. Based on the optical bandgaps, the onset of the lowest unoccupied molecular orbital (LUMO) can be assumed to be at 2.6 and 2.8 eV below the vacuum level for **CP-AE** and **CP-ABCD**, respectively. Consequently, **CP-AE** is operative at an additional energy level in this staggered heterojunction, enabling stepwise hole injection from PEDOT:PSS into **CP-ABCD**. In contrast, electrons are blocked at the **CP-AE**/**CP-ABCD** interface, being favorable for device performance.

In a final step, further considerable device efficiency enhancement was achieved using a cesium carbonate cathode (Cs_2CO_3, workfunction of approximately 2.1 eV[31]) instead of a calcium cathode with its significantly higher workfunction of approximately 2.9 eV.[32] Figure 3b shows the current–voltage and luminescence–voltage characteristics as well as the corresponding electroluminescence spectrum of the optimized ITO/PEDOT:PSS/**CP-AE**/**CP-ABCD**/Cs_2CO_3/Al structure. The inset shows the electroluminescence spectrum of the **CP-AE**/**CP-ABCD** double-layer device with its maximum at 459 nm and a weak shoulder at around 480 nm. Changing the cathode material from calcium to cesium carbonate nearly doubles the efficiency from 1.9 to 3.7 cd A^{-1} at 1000 cd m^{-2}. The maximum device efficiency was measured at low current densities to be at 9.7 cd A^{-1} (Figure S5, Supporting Information). The observed efficiency roll-off in this device structure can be explained by the strongly enhanced electron injection at high bias voltages resulting in a progressive unbalance of electrons and holes. In addition to the high current efficiencies, a high brightness with luminance values of up to 10 600 cd m^{-2} was found for this multilayer approach.

In order to demonstrate the distinct contribution of component **B** to the device efficiency, the reference copolymer **CP-ACD**, was examined in an ITO/PEDOT:PSS/**CP-AE**/**CP-ACD**/Cs_2CO_3/Al configuration, leading to a lower overall efficiency of 2.8 cd A^{-1} at 1000 cd m^{-2}.

In conclusion, the fabrication of highly efficient blue-light-emitting multilayer PLEDs was demonstrated to be possible without the need for orthogonally soluble polymers by employing the novel combination of the copolymers **CP-AE/CP-ABCD** comprising optimized building blocks. We demonstrate that the hole-transporting polymer **CP-AE** leads to a more balanced charge-carrier injection as well as charge blocking at the polymer interface due to optimal band level alignment. Therefore the recombination zone is shifted away from the PEDOT:PSS interface, which was shown to cause defect-induced exciton quenching and spectral changes, and shifted into the **CP-ABCD** layer. The introduction of the **CP-AE** layer not only led to an enhanced spectral stability but also to a clearly increased device efficiency (Table 1). A further efficiency increase was obtained by changing the cathode material from calcium to cesium carbonate. The final ITO/PEDOT:PSS/**CP-AE**/**CP-ABCD**/Cs_2CO_3/Al PLED showed pure blue emission (CIE (Commission Internationale de l'Eclairage) color space coordinates: x = 0.144, y = 0.129), a high luminescence intensity, and notably one of the highest ever reported current efficiencies for blue multilayer PLEDs, 9.7 cd A^{-1}.

Experimental Section

Polymer Synthesis: All of the copolymers were synthesized using a Suzuki-coupling method as described previously.[33] Structures were confirmed by ^1H NMR spectroscopy. Purity was confirmed by trace analysis via inductively coupled plasma mass spectrometry (ICP-MS) checking for traces of monomers (Br, B) and catalyst (Pd, P). The following trace contents were found: Br ≤50 ppm, B ≤20 ppm, P ≤200 ppm, and Pd ≤15 ppm. Molecular weights and polydispersities were determined by gel-permeation chromatography calibrated against polystyrene standards. The molecular weights were in the range of 200 000–600 000 g mol^{-1}, with most polymers between 400 000 and 500 000 g mol^{-1}. The polydispersities were in the range of 2.8–4.0.

UV-Photon Spectroscopy: Ultraviolet photoemission spectra were recorded using a hemispherical electron spectrometer (Scienta SES 100, resolution 120 meV) at the end station SurICat (beamline PM4) of the synchrotron light source BESSY II, consisting of an interconnected sample preparation and analysis chamber in ultrahigh vacuum (UHV), with a base pressure of 10^{-8} and 10^{-10} mbar, respectively. The excitation energy was 35 eV, and for the measurement of the secondary electron cut-off, the sample was biased at –10 V to clear the analyzer workfunction.

Optical Spectroscopy: For the basic characterization of the absorption and the PL behavior, a two-beam Perkin–Elmer Lambda 900 spectrometer and a Shimadzu RF-5301 PL spectro-fluorophotometer were used. All the PL spectra were corrected with the detector-specific sensitivity curve.

Device Fabrication/Characterization: ITO-covered glass substrates were cleaned in acetone, toluene, and isopropanol and subsequently exposed to oxygen plasma. PEDOT:PSS (H.C. Stark Al 4083) layers were spin-coated under ambient conditions and dried at 120 °C under an inert atmosphere. Each copolymer was dissolved in toluene at a concentration of 3 g L^{-1} (**CP-AE**) and 4 g L^{-1} (**CP-ABCD**, **CP-ACD**) and spin-coated on top of the PEDOT:PSS layer, resulting in film thicknesses of about 20 and 60 nm, respectively. The **CP-AE** interlayer was thermally stabilized at 200 °C for 60 min under argon atmosphere whereas the subsequently coated **CP-ABCD** was dried at 70 °C for 60 min under high vacuum. All layer thicknesses were measured by atomic force microscopy (Veeco Dimension V and a Nanoscope V Controller). The multilayer cathode was thermally deposited in a vacuum coating unit at base pressures less than 10^{-6} mbar.

The luminescence–voltage measurements were performed using a silicon photodiode and a computer-controlled Keithley 2612 source measurement unit. Spectral characterization was done with a LOT-ORIEL Multispec equipped with a DB 401-UV charge-coupled device (CCD) camera from Andor.

Supporting Information

Supporting Information is available from the Wiley Online Library or from the author.

Acknowledgements

The authors would like to thank Anna Hayer and Roman Trattnig for fruitful discussions and support. For financial support, the Styrian government (Project POLYLED, GZ:A3-22.B-9/2009-9) is acknowledged.

Received: February 21, 2013
Revised: May 8, 2013
Published online: June 17, 2013

---

[1] C. W. Tang, S. Van Slyke, *Appl. Phys. Lett.* **1987**, *51*, 913.
[2] J. H. Burroughes, D. D. C. Bradley, A. R. Brown, R. N. Marks, K. Mackay, R. H. Friend, P. L. Burn, A. B. Holmes, *Nature* **1990**, *347*, 539.
[3] M. Eritt, C. May, K. Leo, M. Toerker, C. Radehaus, *Thin Solid Films* **2010**, *518*, 3042.
[4] A. R. Duggal, C. M. Heller, J. J. Shiang, J. Liu, L. N. Lewis, *J. Display Technol.* **2007**, *3*, 184.
[5] R. Trattnig, T. M. Figueira-Duarte, D. Lorbach, W. Wiedemair, S. Sax, S. Winkler, A. Vollmer, N. Koch, M. Manca, M. A. Loi, M. Baumgarten, E. J. W. List, K. Müllen, *Opt. Express* **2011**, *19*, A1281.
[6] J. Grimme, M. Kreyenschmidt, F. Uckert, K. Müllen, U. Scherf, *Adv. Mater.* **1995**, *7*, 292.
[7] a) D. Neher, *Macromol. Rapid Commun.* **2001**, *22*, 1365; b) U. Scherf, E. J. W. List, *Adv. Mater.* **2002**, *14*, 477.
[8] a) S. Setayesh, D. Marsitzky, K. Müllen, *Macromolecules* **2000**, *33*, 2016; b) A. C. Grimsdale, P. Leclère, R. Lazzaroni, J. D. MacKenzie, C. Murphy, S. Setayesh, C. Silva, R. H. Friend, K. Müllen, *Adv. Funct. Mater.* **2002**, *12*, 729; c) J. Jacob, J. Zhang, A. C. Grimsdale, K. Müllen, M. Gaal, E. J. W. List, *Macromolecules* **2003**, *36*, 8240.
[9] J. Jacob, S. Sax, T. Piok, E. J. W. List, A. C. Grimsdale, K. Müllen, *J. Am. Chem. Soc.* **2004**, *126*, 6987.
[10] J. Morgado, R. H. Friend, F. Cacialli, *Appl. Phys. Lett.* **2002**, *80*, 2436.
[11] a) H. Riel, H. Vestweber, W. Riess, *Proc. SPIE* **1998**, *3281*, 240; b) X. H. Yang, F. Jaiser, B. Stiller, D. Neher, F. Galbrecht, U. Scherf, *Adv. Funct. Mater.* **2006**, *16*, 2156; c) C. Gu, H. Liu, D. Hu, W. Zhang, Y. Lv, P. Lu, D. Lu, Y. Ma, *Macromol. Rapid Commun.* **2011**, *32*, 1014; d) B. Zhang, W. Li, J. Yang, Y. Fu, Z. Xie, S. Zhang, L. Wang, *J. Phys. Chem. C* **2009**, *113*, 7898.
[12] M. Gross, D. C. Müller, H. G. Nothofer, U. Scherf, D. Neher, C. Bräuchle, K. Meerholz, *Nature* **2000**, *405*, 661.
[13] T. W. Lee, T. Noh, B. K. Choi, M. S. Kim, D. W. Shin, J. Kido, *Appl. Phys. Lett.* **2008**, *92*, 043301.
[14] S. R. Tseng, H. F. Meng, C. H. Yeh, H. C. Lai, S. F. Horng, H. H. Liao, C. S. Hsu, L. C. Lin, *Synth. Met.* **2008**, *158*, 130.
[15] a) N. C. Greenham, S. C. Moratti, D. D. C. Bradley, R. H. Friend, A. B. Holmes, *Nature* **1993**, *365*, 628; b) C. D. Müller, A. Falcou, N. Reckefuss, M. Rojahn, V. Wiederhirn, P. Rudati, H. Frohne, O. Nuyken, H. Becker, K. Meerholz, *Nature* **2003**, *421*, 829; c) X. Jiang, S. Liu, M. S. Liu, H. Ma, A. K.-Y. Jen, *Appl. Phys. Lett.* **2000**, *76*, 2985; d) X. Gong, D. Moses, A. J. Heeger, S. Liu, A. K.-Y. Jen, *Appl. Phys. Lett.* **2003**, *83*, 183.
[16] a) W. Ma, P. K. Iyer, X. Gong, B. Lin, D. Moses, G. C. Bazan, A. J. Heeger, *Adv. Mater.* **2005**, *17*, 274; b) S. Sax, N. Rugen-Penkalla, A. Neuhold, S. Schuh, E. Zojer, E. J. W. List, K. Müllen, *Adv. Mater.* **2010**, *22*, 2087.
[17] a) A. Köhnen, M. Irion, M. C. Gather, N. Rehmann, P. Zacharias, K. Meerholz, *J. Mater. Chem.* **2010**, *20*, 3301; b) Y.-H. Niu, M. S. Liu, J. W. Ka, J. Bardeker, M. T. Zin, R. Schofield, Y. Chi, A. K.-Y. Jen, *Adv. Mater.* **2007**, *19*, 300; c) Y. H. Niu, M. S. Liu, J. W. Ka, A. K.-Y. Jen, *Appl. Phys. Lett.* **2006**, *88*, 093505.
[18] a) N. Koch, *ChemPhysChem* **2007**, *8*, 1438; b) G. Heywang, F. Jonas, *Adv. Mater.* **1992**, *4*, 116; c) B. L. Groenendaal, F. Jonas, D. Freitag, H. Pielartzik, J. R. Reynolds, *Adv. Mater.* **2000**, *12*, 481; d) M. Granstrom, M. Berggren, O. Inganas, *Science* **1995**, *267*, 1479; e) P. K. H. Ho, J.-S. Kim, J. H. Burroughes, H. Becker, S. F. Y. Li, T. M. Brown, F. Cacialli, R. H. Friend, *Nature* **2000**, *404*, 481; f) Q. Xu, J. Ouyang, Y. Yang, T. Ito, J. Kido, *Appl. Phys. Lett.* **2003**, *83*, 4695.
[19] N. Koch, A. Elschner, J. P. Rabe, R. L. Johnson, *Adv. Mater.* **2005**, *17*, 330.
[20] a) D. Poplavskyy, J. Nelson, D. D. C. Bradley, *Appl. Phys. Lett.* **2003**, *83*, 707; b) A. J. A. B. Seeley, R. H. Friend, J. S. Kim, J. H. Burroughes, *J. Appl. Phys.* **2004**, *96*, 7643.
[21] P. J. Brewer, J. Huang, P. A. Lane, A. J. deMello, D. D. C. Bradley, J. C. deMello, *Phys. Rev. B* **2006**, *74*, 115202.
[22] a) S. Wu, S. Han, Y. Zheng, H. Zheng, N. Liu, L. Wang, Y. Cao, J. Wang, *Org. Electron.* **2011**, *12*, 504; b) P. Tehrani, A. Kanciurzewska, X. Crispin, N. D. Robinson, M. Fahlman, M. Berggren, *Solid State Ionics* **2007**, *177*, 3521.
[23] J. S. Kim, R. H. Friend, I. Grizzi, J. H. Burroughes, *Appl. Phys. Lett.* **2005**, *87*, 023506.
[24] R. Q. Png, P. J. Chia, S. Sivaramakrishnan, L. Y. Wong, M. Zhou, L. L. Chua, P. K. H. Ho, *Appl. Phys. Lett.* **2007**, *91*, 013511.
[25] A. van Dijken, A. Perro, E. A. Meulenkamp, K. Brunner, *Org. Electron.* **2003**, *4*, 131.
[26] L. C. Palilis, D. G. Lidzey, M. Redecker, D. D. C. Bradley, M. Inbasekaran, E. P. Woo, W. W. Wu, *Synth. Met.* **2000**, *111*, 159.
[27] S. Kappaun, S. Horner, A.-M. Kelterer, K. Waich, F. Grasse, M. Graf, L. Romaner, F. Niedermair, K. Müllen, A. C. Grimsdale, R. Saf, E. J. W. List, E. Zojer, C. Slugovc, *Macromol. Chem. Phys.* **2008**, *209*, 2122.
[28] C. Y. Chang, F. Y. Tsai, S. J. Jhuo, M.-J. Chen, *Org. Electron.* **2008**, *9*, 667.
[29] S. Kappaun, H. Scheiber, R. Trattnig, E. Zojer, E. J. W. List, C. Slugovc, *Chem. Commun.* **2008**, 5170.
[30] a) W. C. H. Choy, J. H. Niu, X. W. Chen, W. L. Li, P. C. Chui, *Appl. Phys. A* **2007**, *89*, 667; b) S. S. Lee, D. Ko, C. H. Chung, S. M. Cho, *Synth. Met.* **2002**, *128*, 51; c) S. Gamerith, H.-G. Nothofer, U. Scherf, E. J. W. List, *Jpn. J. Appl. Phys.* **2004**, *43*, L891.
[31] J. Huang, Z. Xu, Y. Yang, *Adv. Funct. Mater.* **2007**, *17*, 1966–1973.
[32] N. C. Greenham, A. R. Brown, D. D. C. Bradley, R. H. Friend, *Synth. Met.* **1993**, *57*, 4134.
[33] K. Treacher, P. Stössel, H. Spreitzer, H. Becker, A. Falcou, U.S. Patent Application WO03/048225 A2, **2003**.

ADVANCED
MATERIALS

Supporting Information

for *Adv. Mater.*, DOI: 10.1002/adma.201300832

Highly Efficient Color-Stable Deep-Blue Multilayer PLEDs: Preventing PEDOT:PSS-Induced Interface Degradation

Sebastian Nau, Niels Schulte, Stefanie Winkler, Johannes Frisch, Antje Vollmer, Norbert Koch, Stefan Sax, and Emil J. W. List**

DOI: 10.1002/adma.201300832

Supporting Information

Highly Efficient Color-Stable Deep Blue Multilayer PLEDs: Preventing the PEDOT:PSS Induced Interface Degradation

By *Sebastian Nau*, *Niels Schulte*, *Stefanie Winkler*, *Johannes Frisch*, *Antje Vollmer*, *Norbert Koch*, *Stefan Sax** and *Emil J. W. List**

[*] Prof. E. J. W. List, Dr. S. Sax, S. Nau
NanoTecCenter Weiz Forschungsgesellschaft mbH
Franz-Pichler Straße 32, A-8160 Weiz (Austria)
E-mail: E.List@tugraz.at, Stefan.Sax@ntc-weiz.at
Dr. N. Schulte
Merck KGaA
Frankfurter Str. 250, D-64293 Darmstadt (Germany)
Prof. N. Koch, J. Frisch
Institut für Physik,
Humboldt-Universität zu Berlin
Brook-Taylor-Strasse 6, D-12489 Berlin (Germany)
Dr. A. Vollmer, S. Winkler
Helmholtz Zentrum Berlin für Materialien und Energie GmbH,
Elektronenspeicherring BESSY II
Albert-Einstein-Straße 15, D-12489 Berlin (Germany)
Prof. E. J. W. List
Institute of Solid State Physics,
Graz University of Technology
Petersgasse 32, A-8010 Graz (Austria)

The influence of acidic environments on the thin film emission properties of the three copolymers **CP-AE**, **CP-ACD** and **CP-ABCD** was investigated by blending trifluoroacetic (TFA) in different concentrations to the polymer solutions followed by spin coating on quartz glass. From **figure S1** it's obvious that the normalized PL emission of **CP-AE** and **CP-ACD** is largely unaffected by the acid. In contrast, for **CP-ABCD**, an additional emission peak at 424 nm is evolving with increasing TFA concentration.

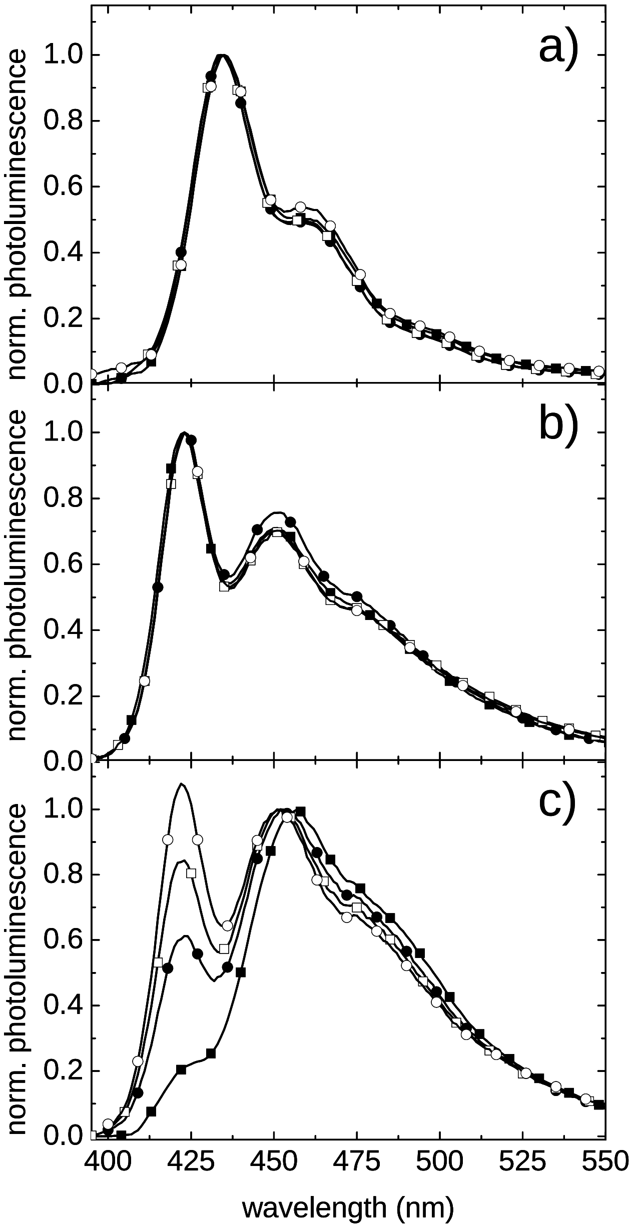

Figure S1. Normalized PL thin film emission spectra of a) **CP-AE** b) **CP-ACD** and c) **CP-ABCD** on glass substrates in dependence of TFA concentration; PL spectra without acid (full squares); PL spectra with 0.5 % TFA blended to the solution (full circles); PL spectra with 1% TFA blended to the solution (open squares); PL spectra with 2% TFA blended to the solution (open circles). For **CP-AE** and **CP-ACD** no influence of the acid was found. For **CP-ABCD**, the emission feature at 424 nm develops to a distinct peak with increasing acidic content.

With respect to the multilayer approach, the polymer interlayer **CP-AE** was stabilized against redissolving by a thermal bake-out process at 200°C in argon atmosphere for 1 hour. **Figure S2** depicts absorbance and PL spectra of the polymer layer before and after the bake out. No changes of the spectral features were found, being a pre-requisite for the applicability of the described stabilization procedure.

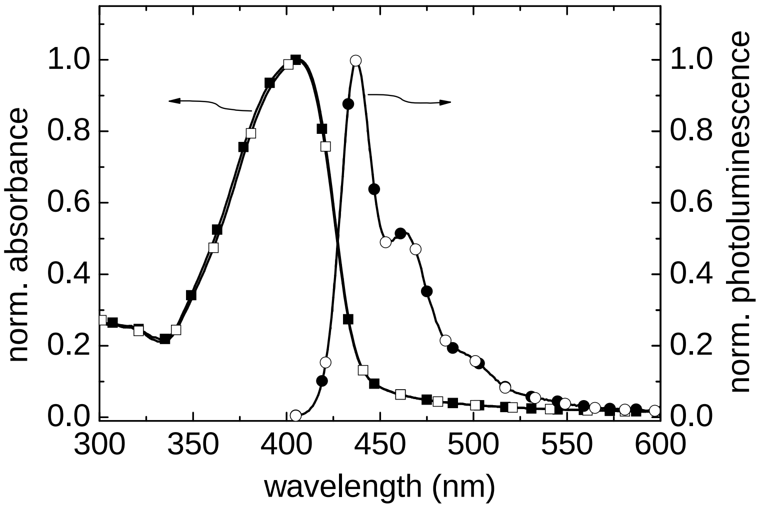

Figure S2. Influence of a thermal bake out to the photophysical thin film properties of **CP-AE**. Spectra were recorded before (absorbance: full squares; PL: full circles) and after (absorbance: open squares; PL: open circles) a 200°C curing process for 1 hour in argon. No distinct changes can be found for the normalized spectra.

Figure S3 shows EL spectra of an ITO/PEDOT:PSS/**CP-ABCD**/Ca/Al single layer reference device (left) and an ITO/PEDOT:PSS/**CP-AE**/**CP-ABCD**/Cs_2CO_3/Al multilayer device (right) in dependence of the applied bias voltage. The distinct features evolving in the spectrum of the **CP-ABCD** single layer device had been shown to be fully reversible and are ascribed to a shift of the recombination zone forwards and backwards with respect to the PSS/**CP-ABCD** interface with degraded vinylene units due to the interaction with PSS. This behaviour was not found for devices using the acid-stable **CP-AE** interlayer. Here, only a slight broadening of the spectrum was obtained for higher bias levels which can be ascribed to a broadening of the recombination zone, leading to an overlap of the spectral contribution of **CP-AE** with the major spectral contribution from **CP-ABCD**. Since higher bias values led to a permanent device breakdown, only spectra up to 10 V are shown for the **CP-AE**/**CP-ABCD** multilayer device.

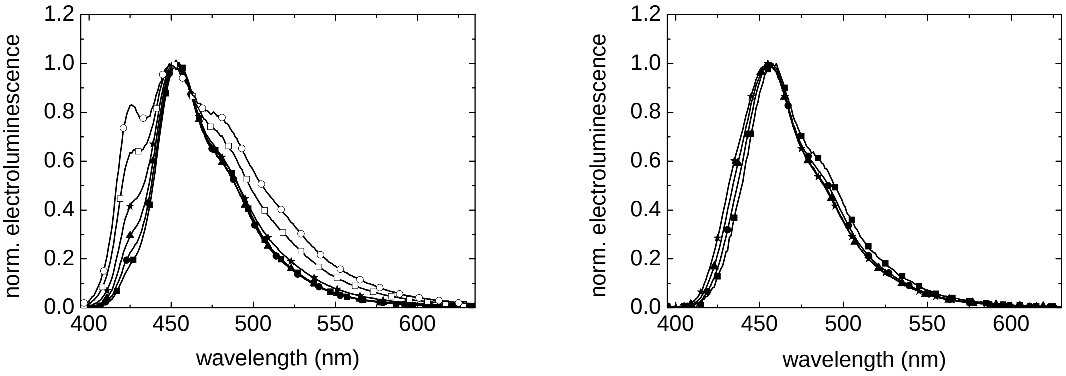

Figure S3. Electroluminescence spectra obtained from an ITO/PEDOT:PSS/**CP-ABCD**/Ca/Al device (left) and an ITO/PEDOT:PSS/**CP-AE**/**CP-ABCD**/Cs_2CO_3/Al device (right) in dependence of the applied bias voltage: full squares: 4 V; full circles: 6 V; full triangles: 8 V; full stars: 10 V; open squares: 12 V; open circles: 14 V.

Figure S4 shows the ultraviolet photon spectroscopy (UPS) spectra of each layer from the PEDOT:PSS/**CP-AE**/**CP-ABCD** device stack. The corresponding workfunctions were determined from the secondary electron cutoff to be at 5.0 eV for PEDOT:PSS and at 4.9 eV for **CP-AE** and **CP-ABCD**. The binding energy onset was found to be at 0.6 eV for **CP-AE** and 0.9 eV for **CP-ABCD** below the fermi level.

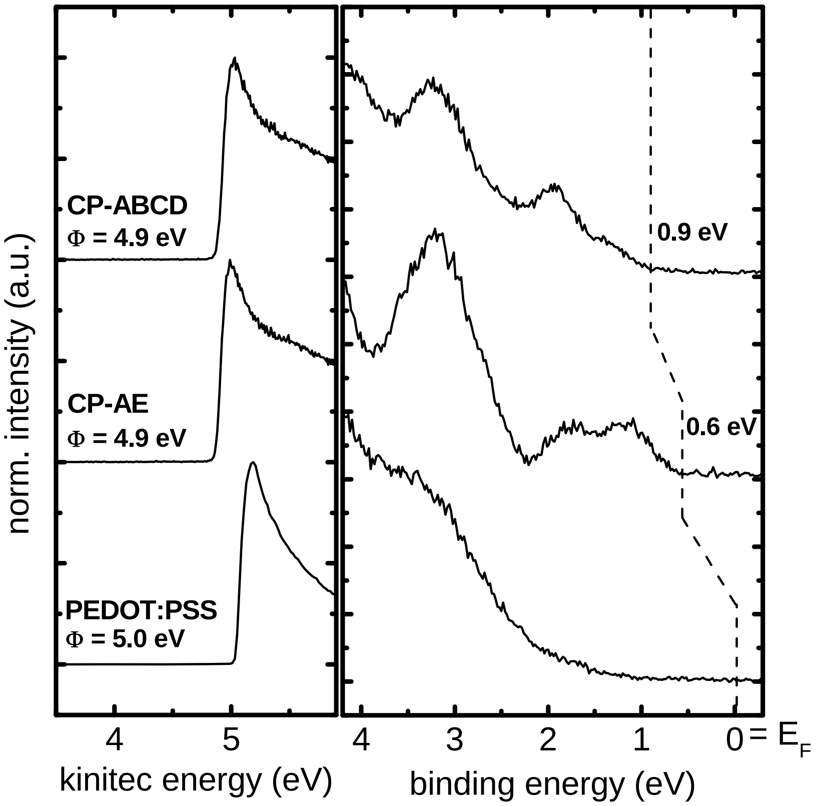

Figure S4. Secondary electron cutoff (left) and valence region UPS (right spectra) of the multilayer structure PEDOT:PSS (bottom) / **CP-AE** (middle) / **CP - ABCD** (top).

Figure S5 shows the device efficiency in dependence of the current density for the three **CP-ABCD** based devices. At low current densities, a high efficiency with an initial value of 9.7 cd A^{-1} was found for the optimized structure, but a high roll-off is observed as well. Since no roll-off is present for the two other **CP-ABCD** based devices, we ascribe this to the strongly enhanced electron injection at high bias levels and a progressive unbalance of electrons and holes. Nevertheless, independent of the applied current density the obtained device efficiencies are at least three to four times higher than for the device without the **CP-AE** interlayer.

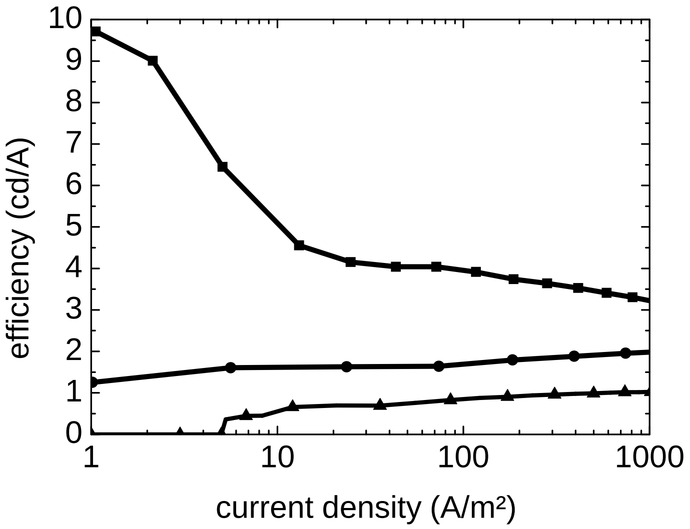

Figure S5. Device efficiency in dependence of the current density for an ITO/PEDOT:PSS/**CP-ABCD**/Ca/Al device (triangles), an ITO/PEDOT:PSS/**CP-AE**/**CP-ABCD**/Ca/Al device (circles) and an ITO/PEDOT:PSS/**CP-AE**/**CP-ABCD**/Cs_2CO_3/Al device (squares).

Unravelling the Nature of Unipolar Resistance Switching in Organic Devices by Utilizing the Photovoltaic Effect

Sebastian Nau, Stefan Sax, and Emil J. W. List-Kratochvil**

Over the past decade, resistive memory[1] has appeared as one of the pace setters in the field of emerging non-volatile random access memory technologies and serious commercialization can be expected soon. Impressive performance values with respect to retention, endurance, and switching speed are reported for memory cells based on metal oxides.[2,3] Owing to the very basic 2-terminal architecture, the integration into 4F^2-footprint passive crossbar arrays promises a great deal in terms of integration density. Alternative applications such as the combination of logic circuitry and memory using one and the same building block,[4] the implementation in neuromorphic systems[5] or its robustness with respect to ionizing radiation[6] additionally offer a large, versatile potential of this technology.

Aside from inorganic memory devices, resistive switching was also observed for a wide variety of devices employing organic materials, paving the way for large area and cost efficient manufacturing using different printing and coating technologies. However, despite considerable research efforts in the field of organic non-volatile memories (ONVM),[7–9] the nature of the switching mechanism is still a subject of debate. A general and consistent explanation about all observations is still missing, making the reliable fabrication and engineering of the devices and their properties challenging and clearly limits widespread applications.

For ONVM, typically bipolar[10] (writing and erasing with opposite polarization of the electric field) and unipolar (writing and erasing with identical polarization of the electric field) switching cells are reported, whereas for the latter typical current-voltage- (*IV*) characteristics (**Figure 1**) can be described as follows: The low bias region is dominated by two clearly distinguishable resistance states, which may be utilized to store logical information. The sharp current threshold at a typical voltage V_T represents the switching of the device from its high resistance state (HRS) to its low resistance state (LRS). The *IV*-curve of both states merges for $V > V_T$ and shows a pronounced region of negative differential resistance (NDR), i.e., decreasing current with increasing voltage, followed by a region of increasing current. Applying a bias above the NDR region sets the device back to its high resistance state. Typically it is also possible to address intermediate resistance states (IMRS) in-between HRS and LRS by applying a voltage in the NDR region.[11,12]

This specific behaviour has been observed for a vast manifold of devices distinguished by nearly every structural parameter; exchanging the electrode materials, the organic semiconductor/insulator or modifying the organics by additional inorganic nanoparticles turned out to not influence the switching mechanism.[13]

Since its discovery, fundamentally two hypotheses, namely charging related phenomena and filament formation related phenomena[14,15] have been applied to explain the observed *IV*-characteristics in ONVM. The former hypotheses are either related to charge-transfer processes in donor-acceptor systems (hybrid or organic)[16–19] or to charging/discharging effects by charge carriers trapped on metallic particles, forming a space-charged field capable to significantly modify the conductivity of the device ('nanotrap'-memory).[13,20–22] These models are dating back on the investigations of Simmons and Verderber (SV)[23] in the 1960s who observed similar *IV*-curves from inorganic Al/SiO$_x$/Au devices (therefore hereafter denoted as SV-model). The SV-model and derived theories are still extensively used to describe resistance switching in ONVM,[24–29] even though, there is significant disagreement between the predictions of the model and experimental observations; e.g., pristine ('as prepared') devices are expected to be in their LRS (particles uncharged) during the first measurement, which is typically not the case.[20] Also, it was reported that the device capacity is constant, regardless of the resistance state.[13]

On the other hand, switching of the device resistance was explained by the formation of highly conductive channels (filaments), shortening the organic layer between the two electrodes. Redox driven formation processes of metallic bridges[10,30] is held to be responsible for bipolar resistive switching devices. For devices with unipolar characteristics, the migration of polarized metal atoms from the electrodes was suggested to play an important role.[31] For both cases, the unintended incorporation of metal during the deposition of the top electrode through film non-uniformities is thought to be significant to induce/promote the growth of a filament.[32]

This work presents a novel approach for the investigation of ONVM based on the circuit model for photovoltaic devices. The obtained parameters, namely the open circuit voltage (V_{oc}) and the short circuit current (I_{sc}), are used to interpret the memory functionality, and lead to solid evidence that the actual cause of unipolar resistive switching is based on the formation of conductive pathways between the electrodes (e.g., filaments), rather than on charging effects. Impedance spectroscopy is performed in order to distinguish between the capacitive and ohmic influence. Furthermore, the model is extended to

S. Nau, Dr. S. Sax, Prof. Dr. E. J. W. List-Kratochvil
NanoTecCenter Weiz Forschungsgesellschaft mbH
Franz-Pichler Straße 32, A-8160, Weiz, Austria
E-mail: stefan.sax@ntc-weiz.at
emil.list-kratochvil@ntc-weiz.at
Prof. Dr. E. J. W. List-Kratochvil
Institute of Solid State Physics
Graz University of Technology
Petersgasse 32, A-8010, Graz, Austria

DOI: 10.1002/adma.201305369

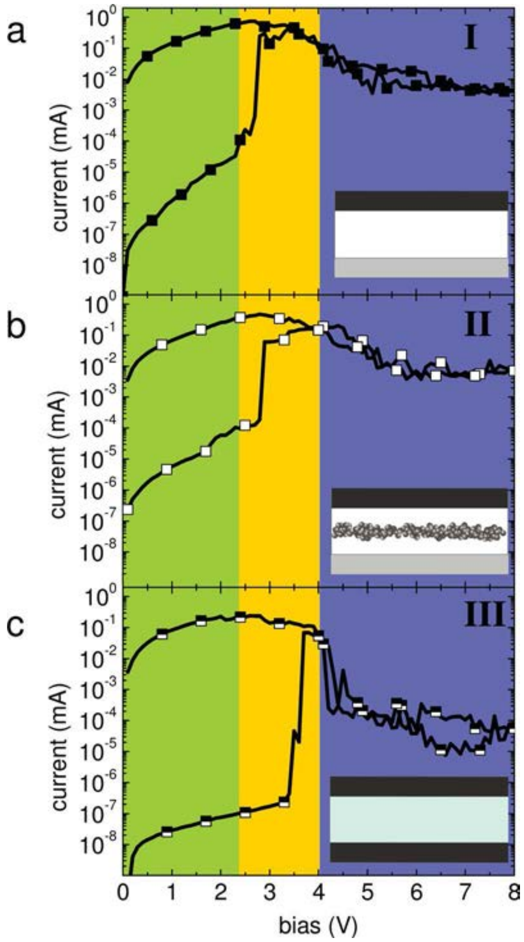

Figure 1. Current-Voltage characteristics of device **I**: ITO/Alq3/Ag (**a**, upper figure); device **II**: ITO/Alq3/Al/Alq3/Ag (**b**, middle) and device **III**: Ag/PMMA/Ag (**c**, lower). The colored areas indicate the three specific regions: For each device two distinctive resistance states are present at low voltages (green), representing the read-out margin. A current threshold can be found between 2.4 V and 4 V, representing the switching from the devices from their HRS to its LRS (yellow). For higher bias levels, a pronounced region of NDR is observed. Applying a bias at the end of this NDR region sets the device back to its initial HRS (blue). All devices were initially in their HRS. The curves were recorded as a double-sweep starting from 0 V to 8 V and again back to 0 V. Sketches of the general setup are shown in the insets.

devices which cannot be investigated by photovoltaic means, i.e., devices employing insulating materials. From the manifold of the fabricated devices (distinguished by the electrodes, the organics or the general setup; Supporting Information,Table S1 and Figure S1–S15), a series of model devices were selected to demonstrate the origin of resistive switching step by step.

Three prototypical resistive switching devices were chosen for these investigations: **I**: an ITO/Aluminium-tris(8-hydroxychinolin) (Alq3)/Ag single layer system, **II**: a tri-layer approach ITO/Alq3/Al/Alq3/Ag, and **III**: an Ag/Poly(methyl methacrylate) (PMMA)/Ag configuration. The basic *IV*–characterization from these assemblies are depicted in Figure 1.

Device **I** can be considered as the reference device to the tri-layer device **II**, one of the most commonly presented device types which is also regarded as a prototypical nanotrap memory:[20,22] the thin intermediate layer (~10 nm) of aluminium is slowly thermally evaporated onto the first organic layer, forming Al-oxide covered particles, which are meant to act as charge traps. Obviously both device structures expose a similarly shaped *IV*-curve. For device **III** a spin coated layer of PMMA was chosen, being a model assembly for devices with insulating organic materials. Also here, qualitatively the same *IV*-characteristics was found during these experiments, making the claimed role of π-conjugation and metallic nanotraps questionable already at this point.

As depicted in Figure 1, all devices have two clearly distinguishable and non-volatile resistance states for bias values <2.7 V, a distinct HRS to LRS threshold voltage at 2.7 V – 3.8 V and a region of NDR between 4 V and 8 V. The shape of the *IV*-curve as well as the location of the threshold can be considered as prototypical for most reported unipolar ONVM systems (Figure S1 – S15). Nevertheless, a major difference of the characteristics is defined by the absolute current through the device, either of the LRS or the HRS state. For device **III** with the insulating PMMA as active material, the HRS current is in the order of 10 pA at 1 V. For device **I** and **II**, using the semiconducting Alq3 as the organic material, the HRS current is increased by two orders of magnitude when compared to device **III**. On the other hand, the variations between the LRS currents from devices **I-III** are significantly smaller and in the range of 70 µA to 150 µA (at 1 V). Consequently, the ratio between the individual resistance values of the HRS and LRS at 1 V (ON/OFF – ratio) was found to be $1.2{*}10^5$ for **I**, $1.1{*}10^4$ for **II** and $2.9{*}10^6$ for **III**, respectively. In addition to these variations of the current levels, the pre-conditioning or forming procedure needed to establish the resistance switching is determined by the actual device setup. While for device **II** bi-stability was immediately present within the first sweep, the other configurations typically developed bi-stability after a forming procedure of about 10 (device **I**) and about 50 (device **III**) *IV*-sweeps.

Device **I** and **II** can in principle be also considered as organic photovoltaic devices. Irrespective of the cause of their electrical bistability, the measurement of photovoltaic parameters from these devices may deliver insight to the underlying working mechanisms.[30,33] When the organic semiconductor of the memory device gets illuminated with a wavelength matching with its optical bandgap, photovoltaic parameters such as the short circuit current I_{sc} (current at zero bias) and the open circuit voltage V_{oc} (voltage at zero current) can be determined. The presented devices are not designed as organic (bulk) heterojunction cells and extractable charge carriers and the resulting photocurrent is therefore mainly generated at the specific organic semiconductor/electrode interfaces.[34] The built-in potential is then largely determined by the work function difference of the two electrode materials determining the obtained open circuit voltage. Although this setup is a rather inefficient solar cell, one can gain insight into the working mechanism of the memory device.

It is well known that the described ONVM devices can take stable intermediate resistance states in-between the two extremes by applying a bias in the NDR region.[11,12] As indicated in **Figure 2**a (inset) seven different resistance states were established in this way for device **I** and for each state the *IV*-curve between –0.1 V and 0.6 V was recorded under constant

Adv. Mater. 2014,
DOI: 10.1002/adma.201305369

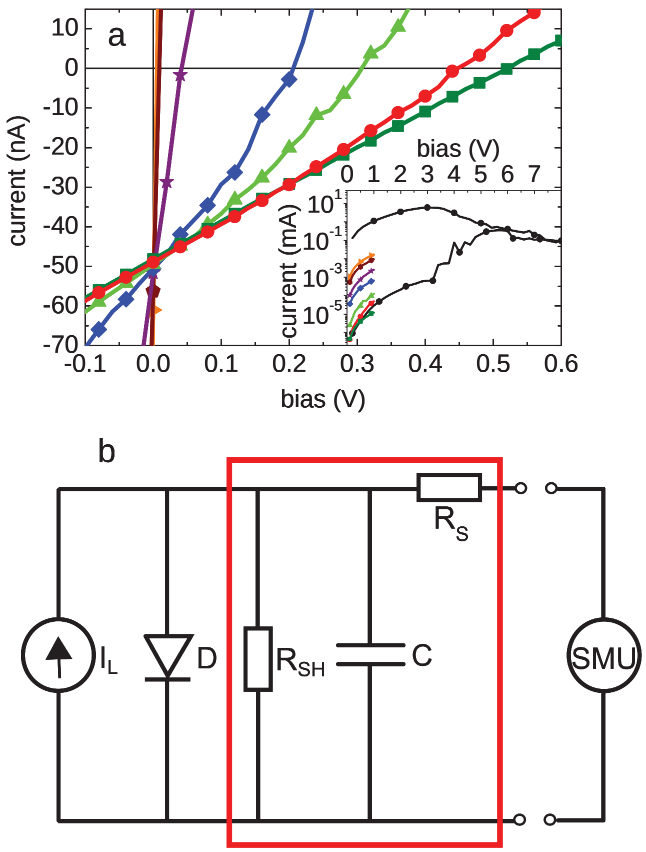

Figure 2. Photovoltaic investigation of a organic memory device: a) *IV* characteristics of different intermediate resistance states from a device of type **I** under illumination. The inset shows a typical *IV* characteristics in a half-logarithmic scale with indicated intermediate state b) Equivalent circuit diagram of an organic photovoltaic device, consisting of a current generating element (i.e., free charge carriers generated by light), a diode (D, accounting for the rectifying ability), a series resistor (R_S, the bulk and contact resistance) and a shunt resistors (R_{SH}, accounting for power dissipation pathways e.g., by material defects or pinholes). The capacitive contribution to the model is considered by C. The red square highlight the relevant building blocks for the switching mechanism.

illumination from a light source with high spectral overlap with the absorption of Alq3 (Figure S17). For the highest resistance, an open circuit voltage of V_{oc} ~ 524 mV was found. Changing the resistance state from the HRS to the LRS via IMRS, the open circuit voltage decreases as well (V_{oc} ~ 524 mV → 450 mV → 307 mV → 207 mV → 42 mV → 10 mV), and finally ends up at 4 mV (Figure 2a). On the other hand, I_{sc} (current at V = 0 under illumination) remains remarkably constant at 50 nA – independent of the device resistance state and of the decrease of V_{oc}. Also for type **II** devices, photovoltaic measurements reveal the same tendency with respect to V_{oc} and I_{sc} (Figure S18).

Variations in the *IV*-curve of a photovoltaic cell are explained by leakage currents resulting from a variable shunt resistance.[35] Such shunting pathways typically result in a reduction of V_{oc} while I_{sc} remains constant,[36,37] which fits exactly with the observations made for the presented ONVM. The studies on shunt pathways in the field of solar cells suggest that these defects are mostly due to the incursion of the electrode material at film non-uniformities and are thus highly localized,[38,39] which is very similar to the model of filamentary conduction in organic resistive switching devices.

On the other hand, in the SV-model the variation of V_{oc} can in principle be attributed to modification of the built-in potential due to charge accumulation; still, the constant short circuit current is in strong contradiction to his model: Since any variation of the space-charge density/distribution capable to change the overall device resistance by several orders of magnitude within the device or at the interfaces, would necessarily lead to a variation of the extracted short circuit current due to the modification of the charge transport properties and the injection/extraction barriers.[40]

To test for the validity of the introduced photovoltaic viewpoint, the devices were modelled with the basic equivalent circuit diagram (ECD) of solar cells (Figure 2b). By changing from the DC to the AC regime, also possible capacitive contributions (considered by C in the ECD) to the resistance switching effect can be revealed. Starting again from the two suggested hypothesis, the expected impact on the building blocks of the ECD was analyzed. In the charging based model, significant changes of the capacitance C are inevitable to explain the switching, whereas C should be largely unaffected in the case of filamentary conduction.

A method to determine whether the device functionality is dominated by capacitive or ohmic changes is given by impedance spectroscopy, where the overall impedance Z and the phase ϕ are measured as a function of the applied frequency f. The obtained impedance and phase spectra are largely unaffected by illumination of the device, leading to equal Z-f and ϕ-f spectra with respect to the individual resistance state (see Supporting Figure S18 and S19). This validates the ECD for devices of type **III**, where the previously introduced photovoltaic method is not feasible due to the lack of optical absorbance of the insulating organic layer.

Figure 3a – f depict the impedance- (Z-f) and the phase-spectra (ϕ-f) of the LRS, HRS and one selected IMRS of **I**, **II** and **III** devices, respectively. In order to avoid a change of the device resistance state during the measurement, the semi-amplitude (0.5 V) of the applied signal was kept well below V_T of the devices.

Apart from quantitative variations in the individual impedance- and phase-spectra of the three different device configurations, qualitatively the same trend was found: Independent on the device geometry and the organic material a strictly linear dependence of the impedance (Figure 3d,e,f) as a function of the frequency was found for all devices in the HRS. Furthermore, the measured phase angle (Figure 3a,b,c) for the HRS of all three devices remains largely constant at −90°, representing a system mainly dominated by a constant capacitance.

By switching the device from the HRS to an IMRS, the phase angle is shifted close to 0° at low frequencies. Along with this shift, each impedance spectrum shows a nearly frequency independent part which bends downwards at a certain cut off frequency. A further modification of the device state to the LRS extends the frequency independent impedance region as well as the frequency range where the phase angle is close to 0°.

Obviously the impedance characteristic of the HRS represents the limiting curve for all other devices states. Above the

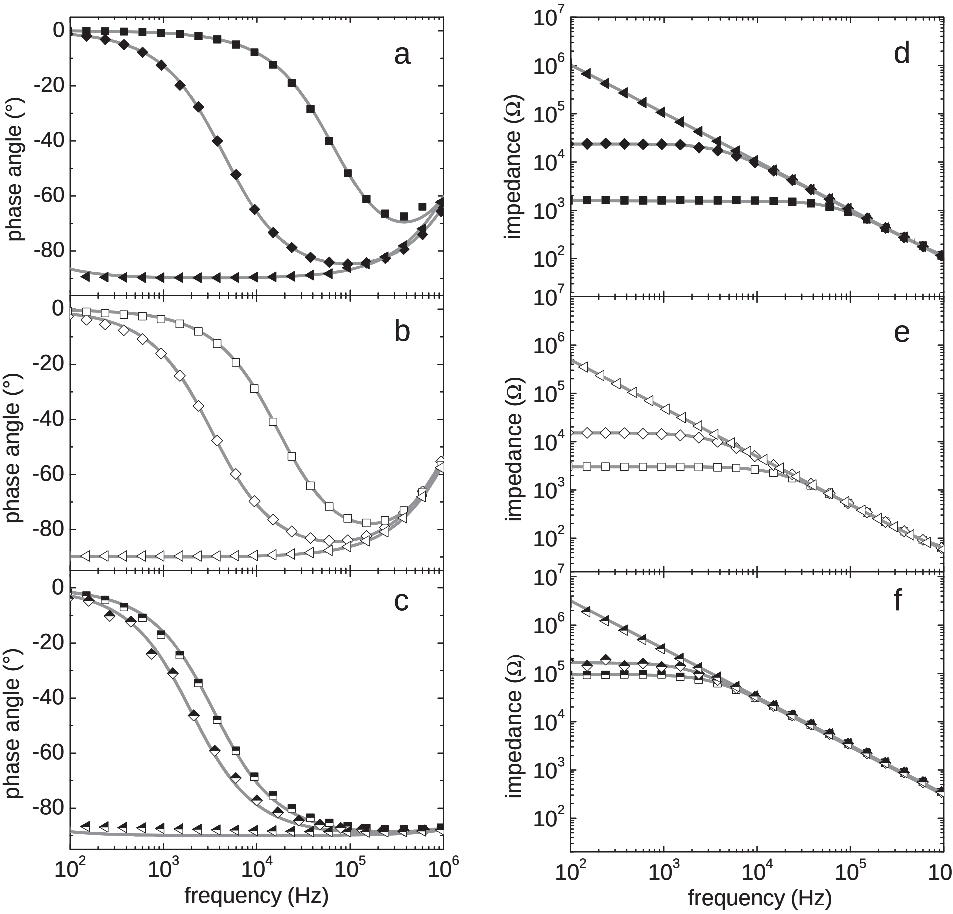

Figure 3. Impedance and phase angle spectra from device types **I-III** for different resistance states: a-c) phase angle d-f) impedance in dependence of the applied frequency from device **I** (a & d), device **II** (b & e) and device **III** (c & f) in different resistance states. Triangles: HRS; Diamonds: IMRS; Squares: LRS. The grey lines represent the fits of the data points according to the equivalent circuit diagram.

cut off frequency of the specific device states, the impedance spectra match with the shape of HRS curve. This overlap shows that the capacitive contribution is constant and can therefore not be responsible for the conductivity of the individual device states. Below the cut off frequency, the phase and the impedance spectra clearly show that the device behaviour is dominated by ohmic conduction.

In contrast to device **I** and **II**, the ϕ-f curve for device **III** does not show this distinctive phase shift to lower angles at high frequencies (f > 10^5 Hz), which is attributed to the reduced contribution of R_s due to the Ag bottom electrode instead of ITO.

Based on the ECD of a solar cell, analytical expressions for the impedance- and the phase response as a function of the frequency, the series resistance R_s, the shunt resistance R_{sh} and the capacity C were derived (see Equation S1 and Equation S2). **Table 1** shows the fitting parameters obtained from the ϕ-f spectra for each device configuration and state. Additionally, fit results from the Z-f spectra qualitatively and quantitatively confirm these values with high accuracy (Table S2): In contrast to the capacitance and the series resistance, which shows no significant dependency on the device state, the corresponding shunt resistance changes by several orders of magnitude.

Table 1. Capacitive and resistive parameters from the three different ONVM in dependence of different resistance states obtained from fits of the ϕ-f spectra (Figure 3a-c).

	ITO/Alq3/Ag			ITO/Alq3/Al/Alq3/Ag			Ag/PMMA/Ag		
	C [nF]	R_S [Ω]	R_{SH} [Ω]	C [nF]	R_S [Ω]	R_{SH} [Ω]	C [nF]	R_S [Ω]	R_{SH} [Ω]
HRS	1.56	58.2	$1.70 * 10^7$	3.16	33.8	$1.43 * 10^8$	0.45	13.6	$1.44 * 10^8$
IMRS	1.56	49.8	$2.30 * 10^4$	3.13	36.9	$1.51 * 10^4$	0.41	15.7	$1.96 * 10^5$
LRS	1.55	50.5	$1.49 * 10^3$	3.32	31.8	$2.79 * 10^3$	0.48	15.0	$9.53 * 10^4$

DOI: 10.1002/adma.201305369

Photovoltaic measurement based analysis of ONVM combined with impedance spectroscopy provide a solid proof that the picture of the equivalent circuit of a solar cell is valid and memory functionality can be assigned to a variable shunt resistance (e.g., due to the growth and rupture of a conductive filament). The charging based model can be clearly ruled out to play a major role due to the constant short circuit current of devices under illumination as well as due to the constant capacitive contribution in the AC-spectra, independent of the individual resistance state. Moreover, all presented devices show qualitatively similar *IV*-characteristics independent of their specific architecture and the used organic- and electrode materials, except from the absolute device currents. The strong variation in the HRS currents can be explained by the different bulk conductivity of the organic materials as well as by the different architectures. As expected, PMMA based devices have the lowest HRS-current. Even though smaller, a variation can also be observed for the LRS current attributed to the stochastic nature of the filament formation process.[41] A strong difference was found during the forming of bi-stability. While single layered device need an extended conditioning procedure, devices with additional metal particles incorporated in the organic matrix quickly show bi-stability, indicating that the metallic particles promote the growth of a filament.

In conclusion, we clearly demonstrated that unipolar resistive switching can be assigned to the same working principle for the prototypical device architectures: A single layered memory device with a semiconducting material (device **I**); A device, considered to be a prototypical nanotrap memory (device **II**), and a single layered device employing the insulating PMMA as active material (device **III**). For all three devices the obtained results point towards filamentary mechanisms as the dominant conductance switching process. In strong contrast to many previous works, we were able to exclude contributions of π-conjugation and charge trapping. We suggest that unipolar resistance switching is a fundamental property of electrode/organic/electrode systems, making this finding significant for researchers working on other typical organic thin film 'sandwich' devices like organic photovoltaic devices or organic light emitting diodes, where the formation of parasitic pathways through the device doubtless is an undesired side-effect.

Experimental Section

Device Fabrication: Each device was fabricated on ITO covered quartz or quartz glass solely. The substrates were cleaned with acetone, 2-propanol and toluene in an ultrasonic bath and subsequently dried. Alq3 was purchased from Sigma-Aldrich and used without further purification. The material was thermally evaporated in a vacuum coating unit at a base pressure lower than $1{*}10^{-6}$ mbar. The silver electrodes were deposited immediately afterwards without breaking the vacuum.

For PMMA based devices, silver electrodes were thermally evaporated onto quartz glass. Afterwards, solutions of PMMA were applied by spin-coating and subsequently dried on a hotplate for 10 minutes at 130 °C. In a final step, Ag top electrodes were again thermally evaporated. The size of all devices was 10 mm^2.

Characterization: The basic *IV*-characterization was performed after contacting the device with tungsten tips using an Agilent B1500A Parameter Analyzer. Impedance and phase spectra were recorded with an Agilent E4980A LCR-Meter. For the *IV*-measurements on devices under constant illumination, a conventional inorganic LED with a high spectral overlap with the absorbance of Alq3 was used as light source (λ_{max} = 402 nm; FWHM = 17 nm, Figure S17). The LED was placed in close proximity to the device under test and was then driven with a constant bias leading to a nominal radiant flux of 12 mW.

All fabrication and characterization steps were performed in an argon filled glovebox (residual gas: <1 ppm O_2 and <1 ppm H_2O).

Supporting Information

Supporting Information is available from the Wiley Online Library or from the author.

Acknowledgements

This work was supported by FP7-NMP-2010-SMALL-4 program, project number 263073 (HYMEC).

Received: October 29, 2013
Revised: November 21, 2013

---

[1] D. B. Strukov, G. S. Snider, D. R. Stewart, R. S. Williams, *Nature* **2008**, *453*, 80.
[2] K. Szot, M. Rogala, W. Speier, Z. Klusek, A. Besmehn, R. Waser, *Nanotechnology* **2011**, *22*, 254001.
[3] M.-J. Lee, C. B. Lee, D. Lee, S. R. Lee, M. Chang, J. H. Hur, Y.-B. Kim, C.-J. Kim, D. H. Seo, S. Seo, U.-I. Chung, I.-K. Yoo, K. Kim, *Nat. Mater.* **2011**, *10*, 625.
[4] J. Borghetti, G. S. Snider, P. J. Kuekes, J. J. Yang, D. R. Stewart, R. S. Williams, *Nature* **2010**, *464*, 873.
[5] S. H. Jo, T. Chang, I. Ebong, B. B. Bhadviya, P. Mazumder, W. Lu, *Nano Lett.* **2010**, *10*, 1297.
[6] W. M. Tong, J. J. Yang, P. J. Kuekes, D. R. Stewart, R. S. Williams, E. Deionno, E. E. King, S. C. Witczak, M. D. Looper, J. V. Osborn, *IEEE Trans. Nucl. Sci.* **2010**, *57*, 1640.
[7] J. C. Scott, L. D. Bozano, *Adv. Mater.* **2007**, *19*, 1452.
[8] Q.-D. Ling, D.-J. Liaw, C. Zhu, D. S.-H. Chan, E.-T. Kang, K.-G. Neoh, *Prog. Polym. Sci.* **2008**, *33*, 917.
[9] B. Cho, S. Song, Y. Ji, T.-W. Kim, T. Lee, *Adv. Funct. Mater.* **2011**, *21*, 2806.
[10] B. Cho, J.-M. Yun, S. Song, Y. Ji, D.-Y. Kim, T. Lee, *Adv. Funct. Mater.* **2011**, *21*, 3976.
[11] V. S. Reddy, S. Karak, A. Dhar, *Appl. Phys. Lett.* **2009**, *94*, 173304.
[12] J. Park, W. Nam, S. Seo, Y. Kim, Y. Oh, G. Lee, U. Paik, *Nano Lett.* **2009**, *9*, 1713.
[13] L. D. Bozano, B. W. Kean, M. Beinhoff, K. R. Carter, P. M. Rice, J. C. Scott, *Adv. Funct. Mater.* **2005**, *15*, 1933.
[14] P. Sebastian, F. Lindner, K. Walzer, B. Lüssem, K. Leo, *J. Appl. Phys.* **2011**, *110*, 084508.
[15] W. L. Kwan, B. Lei, Y. Shao, Y. Yang, *Curr. Appl. Phys.* **2010**, *10*, e50.
[16] J. Ouyang, C.-W. Chu, C. R. Szmanda, L. Ma, Y. Yang, *Nat. Mater.* **2004**, *3*, 918.
[17] C. W. Chu, J. Ouyang, J.-H. Tseng, Y. Yang, *Adv. Mater.* **2005**, *17*, 1440.
[18] R. J. Tseng, J. Huang, J. Ouyang, R. B. Kaner, Y. Yang, *Nano Lett.* **2005**, *5*, 1077.
[19] B. Cho, T. Kim, S. Song, Y. Ji, M. Jo, H. Hwang, G.-Y. Jung, T. Lee, *Adv. Mater.* **2010**, *22*, 1228.
[20] L. D. Bozano, B. W. Kean, V. R. Deline, J. R. Salem, J. C. Scott, *Appl. Phys. Lett.* **2004**, *84*, 607.

[21] L. Ma, S. Pyo, J. Ouyang, Q. Xu, Y. Yang, *Appl. Phys. Lett.* **2003**, *82*, 1419.
[22] V. Reddy, S. Karak, S. Ray, A. Dhar, *Org. Electron.* **2009**, *10*, 138.
[23] J. G. Simmons, R. R. Verderber, *Proc. R. Soc. Lond. A. Math. Phys. Sci.* **1967**, *301*, 77.
[24] S. Song, J. Jang, Y. Ji, S. Park, T.-W. Kim, Y. Song, M.-H. Yoon, H. C. Ko, G.-Y. Jung, T. Lee, *Org. Electron.* **2013**, *14*, 2087.
[25] M. Xie, K. C. Aw, M. Langlois, W. Gao, *Solid State Commun.* **2012**, *152*, 835.
[26] B. Cho, K. H. Nam, S. Song, Y. Ji, G.-Y. Jung, T. Lee, *Curr. Appl. Phys.* **2012**, *12*, 940.
[27] J.-D. Lee, H.-M. Seung, K.-C. Kwon, J. Park, *Curr. Appl. Phys.* **2011**, *11*, e25.
[28] T. Kondo, S. M. Lee, M. Malicki, B. Domercq, S. R. Marder, B. Kippelen, *Adv. Funct. Mater.* **2008**, *18*, 1112.
[29] H. Houili, E. Tutiš, R. Izquierdo, *Org. Electron.* **2010**, *11*, 514.
[30] S. Gao, C. Song, C. Chen, F. Zeng, F. Pan, *J. Phys. Chem. C* **2012**, *116*, 17955.
[31] Y. T. You, Q. Zeng, Y. Yao, M. L. Wang, B. Wu, Y. He, Y. M. Hu, C. Q. Wu, X. Y. Hou, *Appl. Phys. Lett.* **2012**, *100*, 123304.
[32] W. L. Kwan, B. Lei, Y. Shao, S. V. Prikhodko, N. Bodzin, Y. Yang, *J. Appl. Phys.* **2009**, *105*, 124516.
[33] B. Ghosh, A. J. Pal, *J. Phys. Chem. C* **2009**, *113*, 18391.
[34] G. G. Malliaras, J. R. Salem, P. J. Brock, J. C. Scott, *J. Appl. Phys.* **1998**, *84*, 1583.
[35] S. Dongaonkar, J. D. Servaites, G. M. Ford, S. Loser, J. Moore, R. M. Gelfand, H. Mohseni, H. W. Hillhouse, R. Agrawal, M. A. Ratner, T. J. Marks, M. S. Lundstrom, M. A. Alam, *J. Appl. Phys.* **2010**, *108*, 124509.
[36] O. Breitenstein, Proc. 17th NREL Work. Cryst. Silicon Sol. Cells Modul. Mater. Process. **2007**, Vail, USA, 61.
[37] B. Qi, J. Wang, *Phys. Chem. Chem. Phys.* **2013**, *15*, 8972.
[38] R. Steim, S. A. Choulis, P. Schilinsky, U. Lemmer, C. J. Brabec, *Appl. Phys. Lett.* **2009**, *94*, 043304.
[39] H. Hoppe, J. Bachmann, B. Muhsin, K.-H. Drüe, I. Riedel, G. Gobsch, C. Buerhop-Lutz, C. J. Brabec, V. Dyakonov, *J. Appl. Phys.* **2010**, *107*, 014505.
[40] S. van Reenen, P. Matyba, A. Dzwilewski, R. A. J. Janssen, L. Edman, M. Kemerink, *J. Am. Chem. Soc.* **2010**, *132*, 13776.
[41] B. Lei, W. L. Kwan, Y. Shao, Y. Yang, *Org. Electron.* **2009**, *10*, 1048.

ADVANCED
MATERIALS

Supporting Information

for *Adv. Mater.*, DOI: 10.1002/adma.201305369

Unravelling the Nature of Unipolar Resistance Switching in Organic Devices by Utilizing the Photovoltaic Effect

Sebastian Nau, Stefan Sax, and Emil J. W. List-Kratochvil**

Supporting Information

Unravelling the nature of unipolar resistance switching in organic devices by utilizing the photovoltaic effect

Sebastian Nau, Stefan Sax and Emil J. W. List-Kratochvil**

S. Nau, Dr. S. Sax, Prof. Dr. E. J. W. List-Kratochvil,
NanoTecCenter Weiz Forschungsgesellschaft mbH
Franz-Pichler Straße 32, A-8160 Weiz (Austria)
E-mail: e.list-kratochvil@ntc-weiz.at.at, stefan.sax@ntc-weiz.at
Prof. Dr. E. J. W. List-Kratochvil
Institute of Solid State Physics,
Graz University of Technology
Petersgasse 32, A-8010 Graz (Austria)

Figure S1-S15 show the IV characteristics of different device structures (as summarized in **Table S1**). Independent of the actual device setup, the used electrode materials and the organic semiconductor/dielectric, qualitatively equal IV-curves were found.

Table S1. List of the additionally fabricated device structures.

Figure #	Device structure
Figure S1	ITO/40-XT Photoresist/Ag
Figure S2	Ag/Alq3/Ag
Figure S3	ITO/Alq3/Ca/Ag
Figure S4	ITO/Ca/Alq3/Ca/Ag
Figure S5	ITO/Alq3/Au/Alq3/Ag
Figure S6	ITO/PEDOT:PSS/Alq3/Ag
Figure S7	ITO/PEDOT:PSS/Alq3/Al/Alq3/Ag
Figure S8	ITO/Alq3/Al/Alq3/Al/Alq3/Al/Alq3/Ag
Figure S9	ITO/NPB/Ag
Figure S10	ITO/NPB/Au/Alq3/Ag
Figure S11	ITO/PVK/Au/PVK/Ag
Figure S12	ITO/PVK/Al/PVK/Ag
Figure S13	ITO/PEDOT:PSS/PS/Ag
Figure S14	ITO/PVK/Au/PS/Ag
Figure S15	Al/PS/Al Al/PS:8HQ/Al Al/PS:8HQ:gold nanoparticles /Al

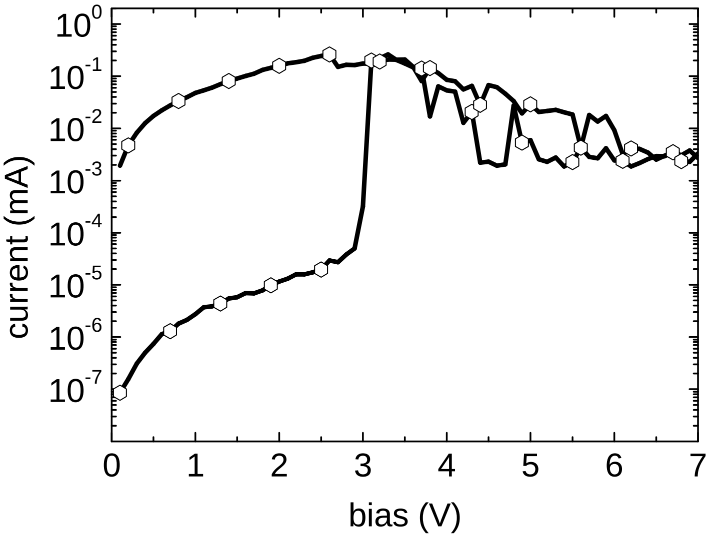

Figure S1. IV-characteristics of an ITO/40-XT Photoresist/Ag device. The device was initially in its high resistive state; Sweeping from 0 V to 7 V leads to a current threshold at ~3.1 V and a region of negative differential resistance from 3.5 V to 7 V; the device remains in a low resistive state when sweeping from 7 V back to 0 V. The ON/OFF-ratio at 1 V is $1.7*10^{4}$. The ITO electrode acts as positive contact.

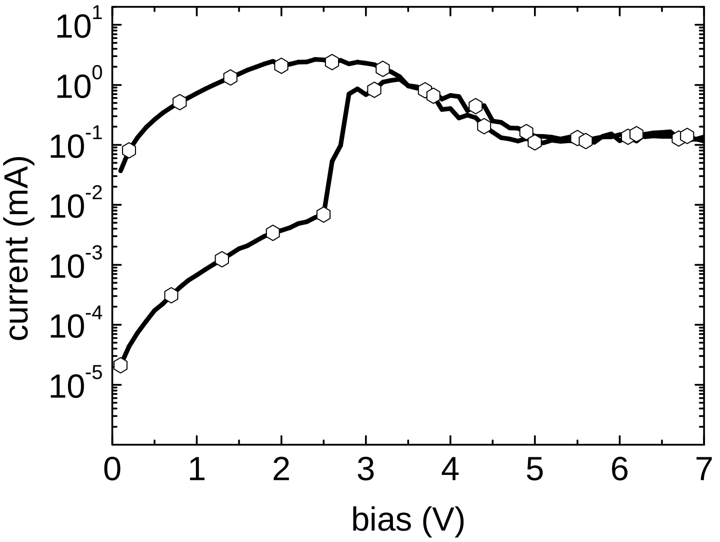

Figure S2. IV-characteristics of an Ag/Alq3/Ag device. The ON/OFF-ratio at 1 V is ~1*10^3.

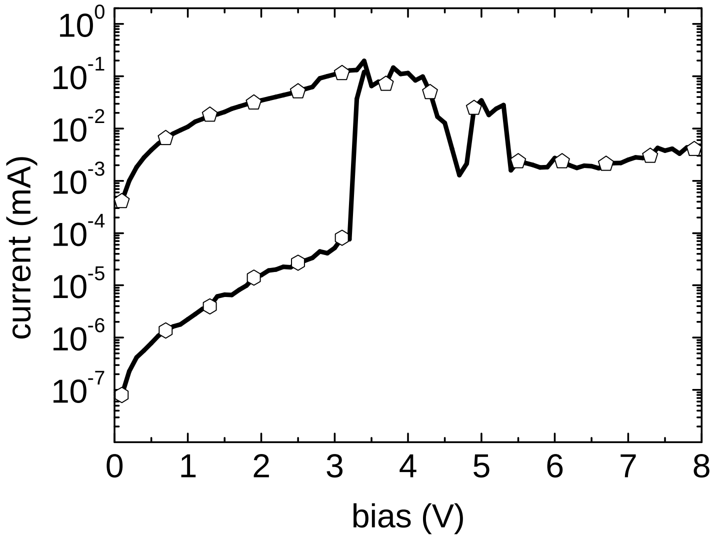

Figure S3. IV-characteristics of an ITO/Alq3/Ca/Ag device. The ON/OFF-ratio at 1 V is ~2*10^4. The ITO electrode acts as positive contact.

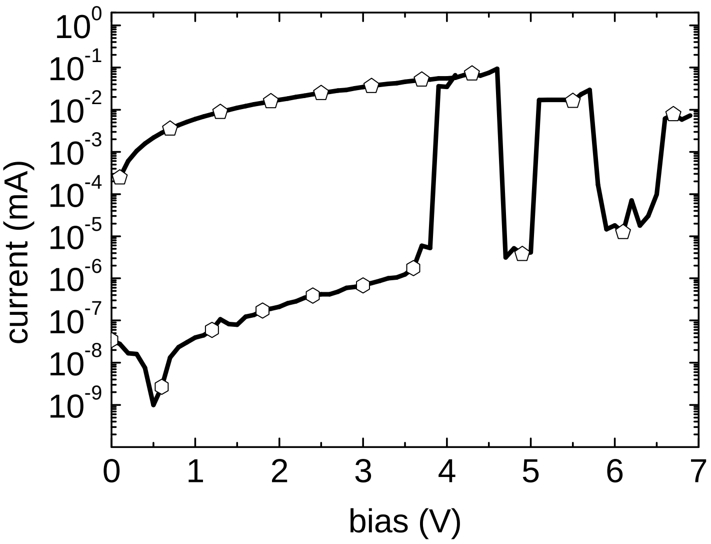

Figure S4. IV-characteristics of an ITO/Ca/Alq3/Ca/Ag device. The ON/OFF-ratio at 1 V is ~1.5*10^5. The ITO electrode acts as positive contact.

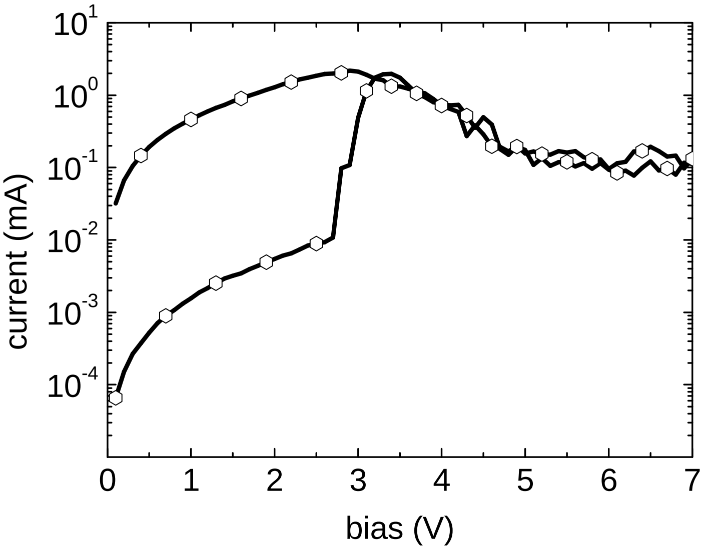

Figure S5. IV-characteristics of an ITO/Alq3/Au/Alq3/Ag device. The Au - intermediate metal was nominally 2 nm thick. The ON/OFF-ratio at 1 V is ~3*10^2. The ITO electrode acts as positive contact.

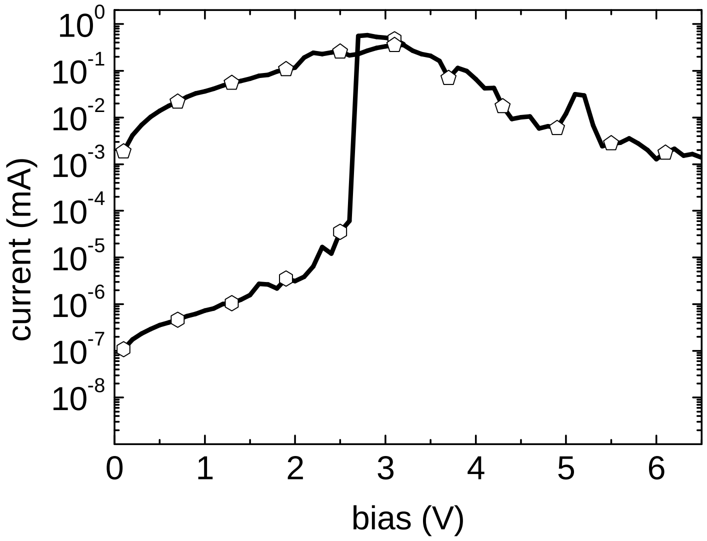

Figure S6. IV-characteristics of an ITO/PEDOT:PSS/Alq3/Ag device. The ON/OFF-ratio at 1 V is ~5*10^4. The ITO electrode acts as positive contact. Green electroluminescence was observed starting from ~8V.

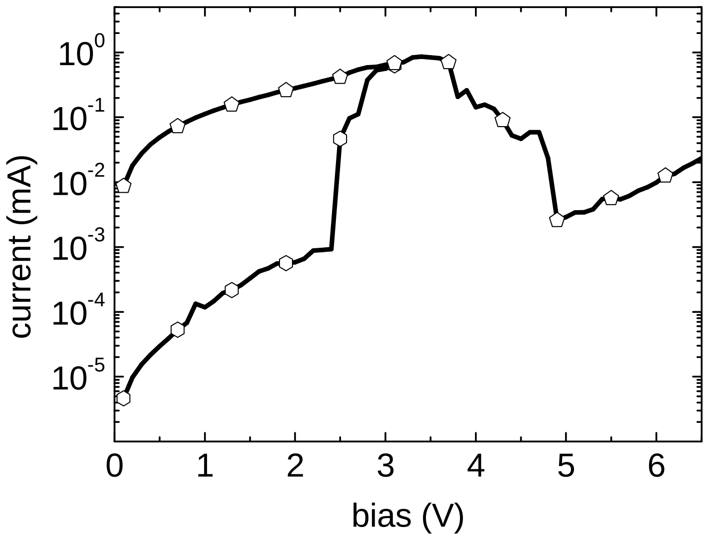

Figure S7. IV-characteristics of an ITO/PEDOT:PSS/Alq3/Al/Alq3/Ag device. The ON/OFF-ratio at 1 V is ~1*10^3. The ITO electrode acts as positive contact.

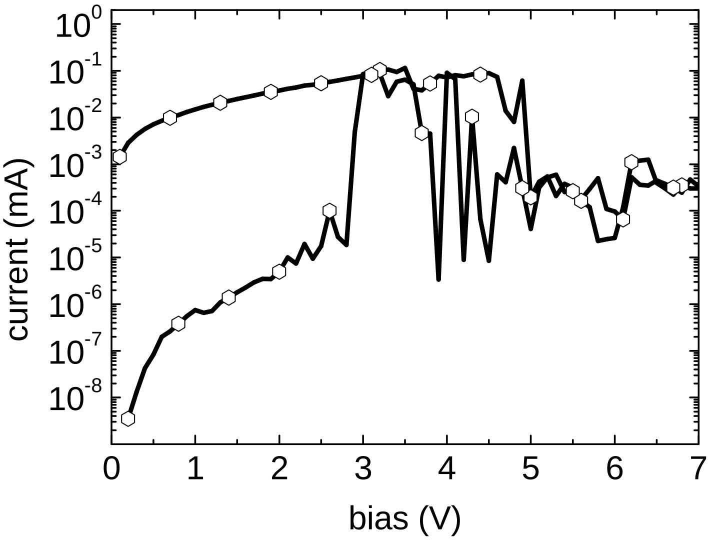

Figure S8. IV-characteristics of an ITO/Alq3/Al/Alq3/Al/Alq3/Al/Alq3/Ag device. Each Al-intermediate layer has a thickness of ~10 nm. The ON/OFF-ratio at 1 V is ~ $2*10^4$. The ITO electrode acts as positive contact.

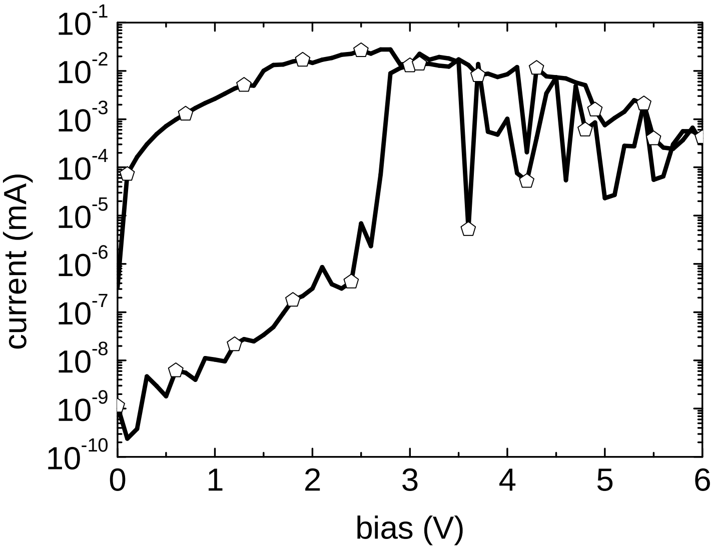

Figure S9. IV-characteristics of an ITO/N,N′-Di-[(1-naphthyl)-N,N′-diphenyl]-1,1′-biphenyl)-4,4′-diamine (NPB)/Ag device. The ON/OFF-ratio at 1 V is ~$2.6*10^5$. The ITO electrode acts as positive contact.

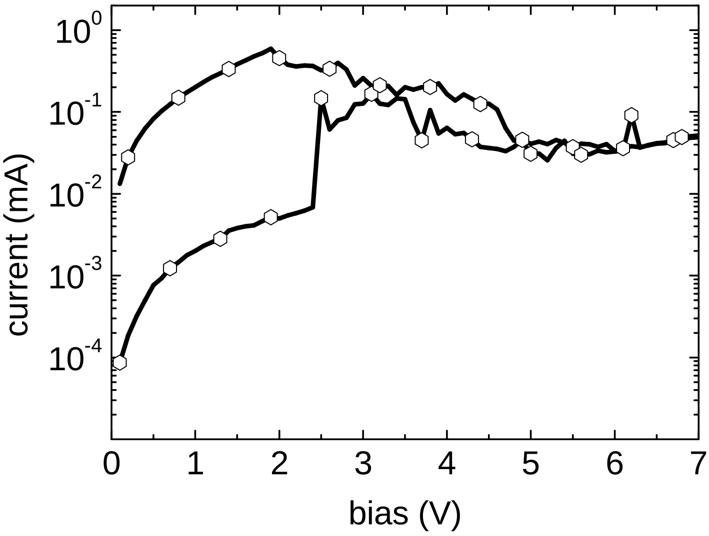

Figure S10. IV-characteristics of an ITO/NPB/Au/Alq3/Ag device. The Au - intermediate metal was nominally 2 nm thick. The ON/OFF-ratio at 1 V is ~1*10^2. The ITO electrode acts as positive contact.

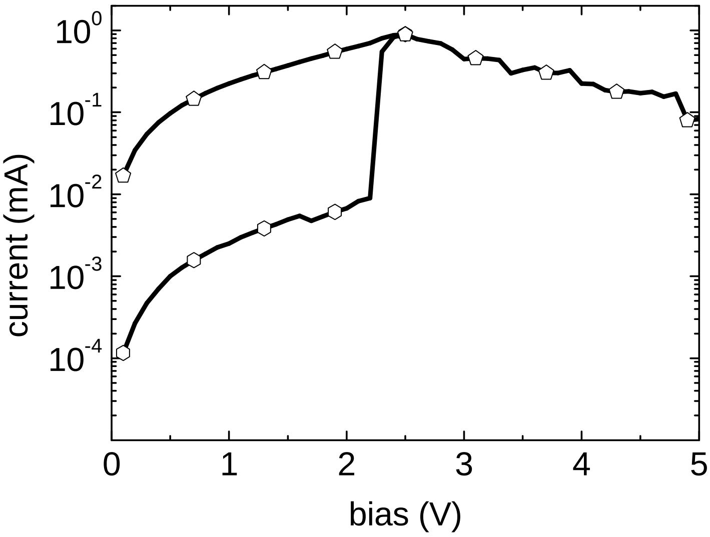

Figure S11. IV-characteristics of an ITO/Poly(9-vinylcarbazole) (PVK)/Au/PVK/Ag device. The Au - intermediate metal was nominally 2 nm thick. The ON/OFF-ratio at 1 V is ~9*10^1. The ITO electrode acts as positive contact.

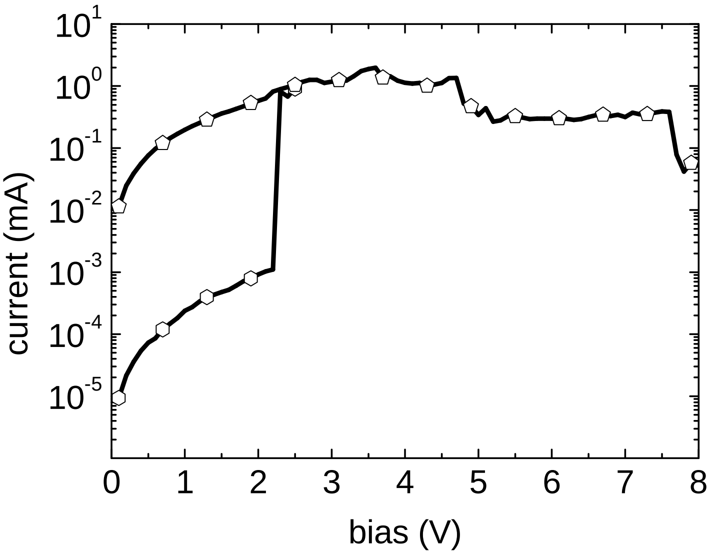

Figure S12. IV-characteristics of an ITO/PVK/Al/PVK/Ag device. The Al - intermediate metal was nominally 10 nm thick. The ON/OFF-ratio at 1 V is ~8.4*10^2. The ITO electrode acts as positive contact.

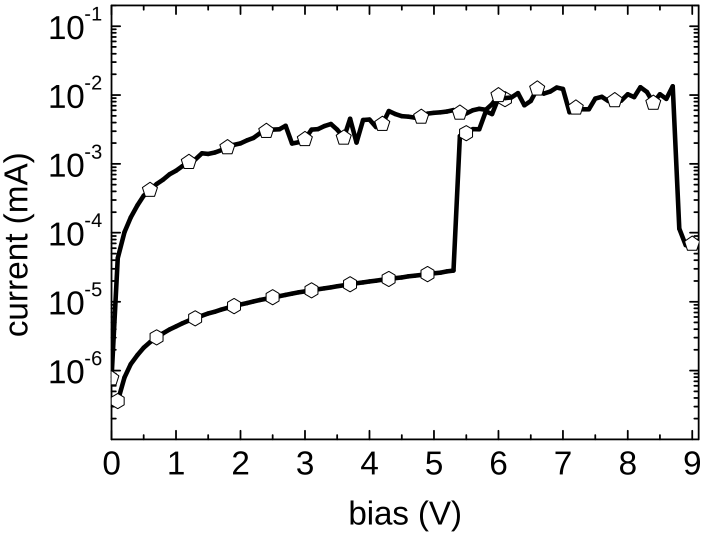

Figure S13. IV-characteristics of an ITO/PEDOT:PSS/PS/Ag device. The ON/OFF-ratio at 1 V is ~1.8*10^2. The ITO electrode acts as positive contact.

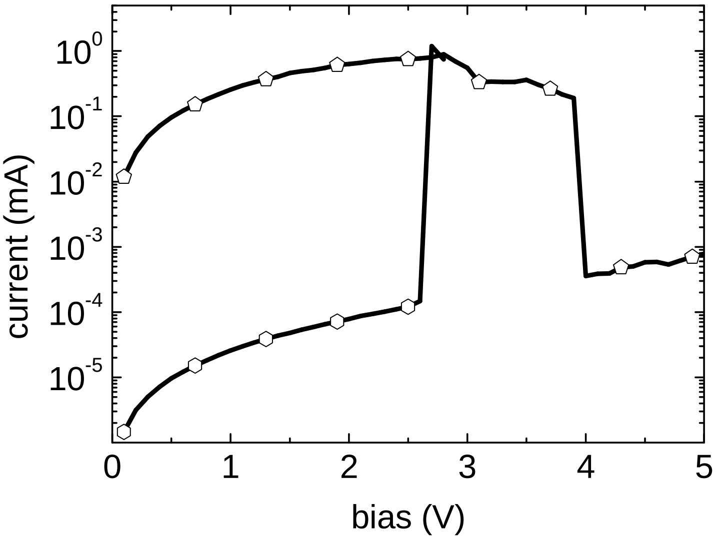

Figure S14. IV-characteristics of an ITO/PVK/Au/PS/Ag device. The ON/OFF-ratio at 1 V is ~1*10^4. The ITO electrode acts as positive contact.

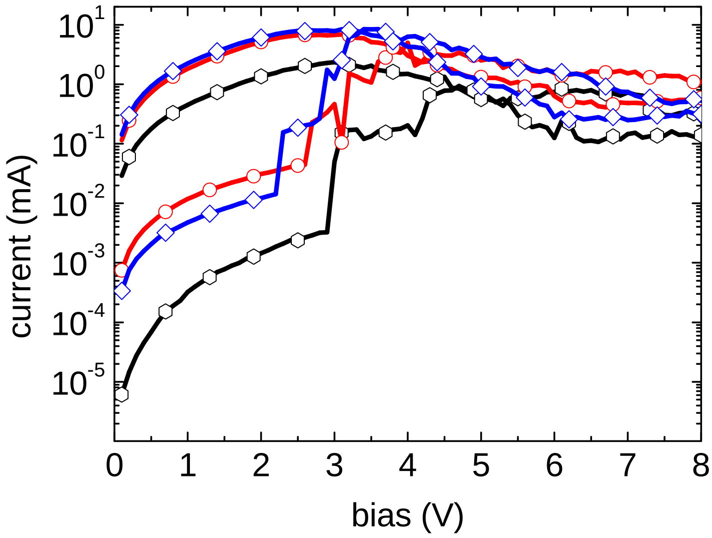

Figure S15. IV-characteristics of an Al/Poly(styrene) (PS)/Al device (black, hexagons); an Al/PS:8-hydroxychinolin (8HQ)/Al device (red, circles) and an Al/PS:8HQ:Dodecanethiol functionalized gold nanoparticles (Au-NPs)/Al (blue, diamonds). The ON/OFF-ratio at 1 V is ~ 1.4*10^3, ~ 1.5*10^2 and ~ 4.7*10^2, respectively.

This series of devices was rebuilt according to [15].

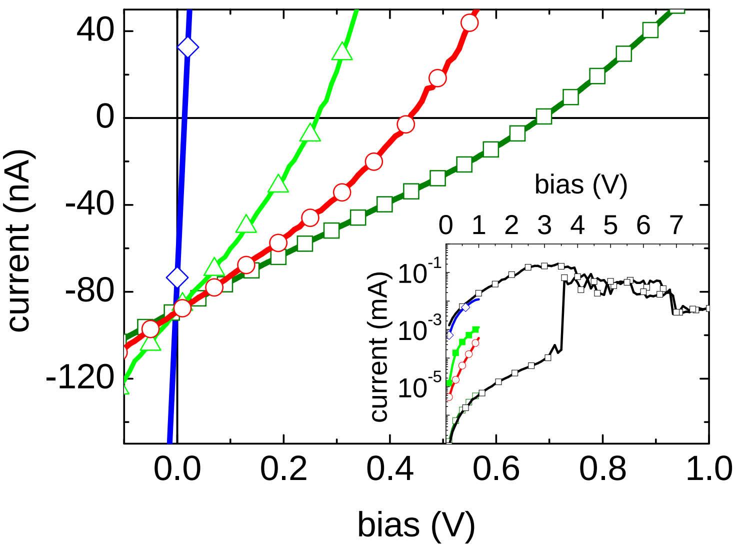

Figure S16. IV-characteristics of four different resistance states from a device of type **II** under illumination. The obtained open circuit voltage is strongly dependent on the resistance state, whereas the short circuit current is largely constant. The inset shows a typical IV-characteristics in a half-logarithmic scale with indicated intermediate states.

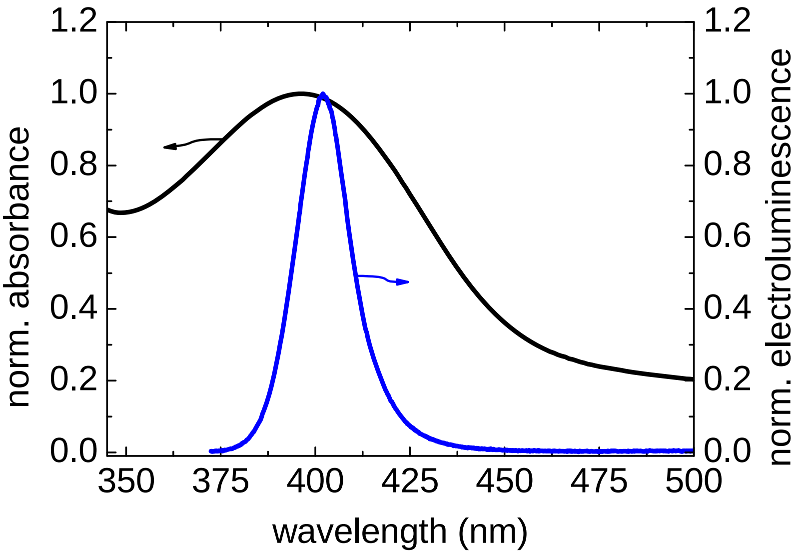

Figure S17. Spectral overlap between the normalized absorbance spectrum of Alq3 (black line) and the normalized emission spectrum of the used excitation light source (blue line). Alq3 has a broad absorption spectrum with its maximum at around 397 nm. The excitation LED shows a narrow emission with its maximum at 402 nm/FWHM = 17nm.

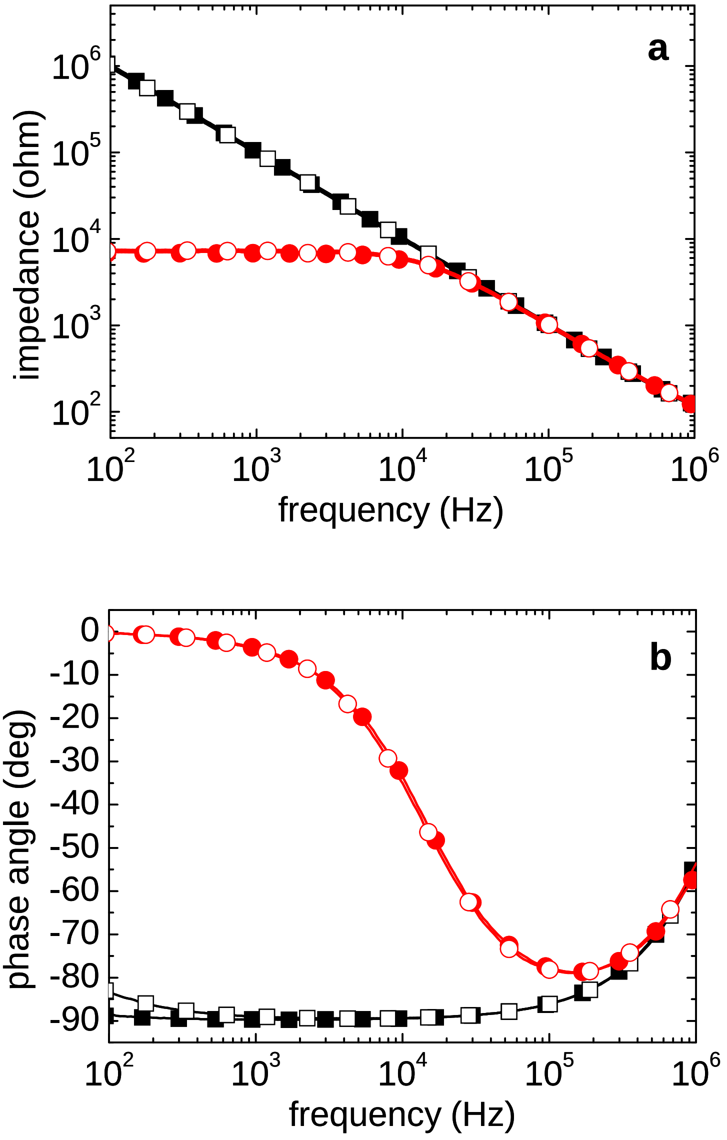

Figure S18. Impedance (**a**) and phase-angle (**b**) spectra of a type **I** device in its high resistance state (squares) and the low resistance state (circles). The spectra in dark (closed symbols) were found to be largely equal to the spectra obtained from illuminated samples (open symbols). The small variation in the φ-f spectrum of the HRS is accounted to photoconductivity. IV-characteristics of this device before and after illumination are shown in Figure S19.

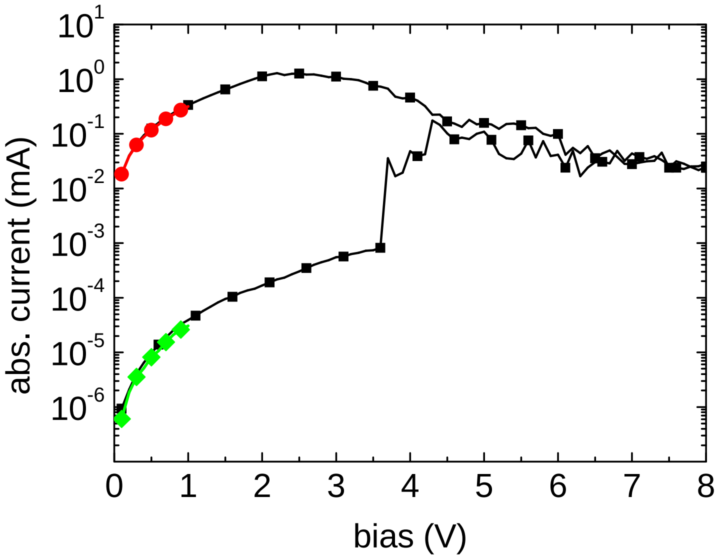

Figure S19. IV – characteristics of device **I** corresponding to the impedance and phase spectra shown in Figure S18: before illumination (black line, closed squares); HRS after 5 minutes of illumination (green line, closed diamonds); LRS after 5 minutes of illumination (red line; closed circles). No significant impact to the resistance state was found due to illumination.

$$\tan\varphi = \frac{\dfrac{2\cdot\pi\cdot f\cdot C\cdot {R_{SH}}^{2}}{1+4\cdot\pi^{2}\cdot f^{2}\cdot C^{2}\cdot {R_{SH}}^{2}}}{R_{s}+\dfrac{R_{SH}}{1+4\cdot\pi^{2}\cdot f^{2}\cdot C^{2}\cdot {R_{SH}}^{2}}}$$

Equation S1. Relation for the phase angle in dependence of capacity C, the series resistance R_S and the shunt resistance R_{SH} derived from the equivalent circuit diagram presented in the main text.

$$Z = R_S + \frac{R_{SH}}{1+4\cdot\pi^{2}\cdot f^{2}\cdot C^{2}\cdot {R_{SH}}^{2}} + j\cdot\frac{2\cdot\pi\cdot f\cdot C\cdot {R_{SH}}^{2}}{1+4\cdot\pi^{2}\cdot f^{2}\cdot C^{2}\cdot {R_{SH}}^{2}}$$

$$|Z| = \sqrt{\Re e(Z)^{2} + \Im m(Z)^{2}}$$

Equation S2. Relation for the impedance in dependence of the capacity C, the series resistance R_S and the shunt resistance R_{SH} derived from the equivalent circuit diagram presented in the main text.

Table S2. Capacitive and resistive parameters from the three different ONVM in dependence of different resistance states obtained from fits of the Z-f spectra (Figure 3d-f)

	ITO/Alq3/Ag			ITO/Alq3/Al/Alq3/Ag			Ag/PMMA/Ag		
	C [nF]	R_S [Ω]	R_{SH} [Ω]	C [nF]	R_S [Ω]	R_{SH} [Ω]	C [nF]	R_S [Ω]	R_{SH} [Ω]
HRS	1.56	45.1	$1.56*10^{7}$	3.23	38.9	$1.30*10^{8}$	0.50	12.90	$1.56*10^{8}$
IMRS	1.60	52.6	$2.36*10^{4}$	3.26	43.2	$1.51*10^{4}$	0.52	12.0	$1.66*10^{5}$
LRS	1.54	39.4	$1.57*10^{3}$	3.17	32.4	$2.98*10^{3}$	0.50	5.00	$9.41*10^{4}$